

**Low cycle lifetime assessment  
of Al2024 alloys**

**Dissertation**

**zur Erlangung des akademischen Grades  
Doktor der Ingenieurwissenschaften  
(Dr.-Ing.)**

**der Fakultät Maschinenbau  
der Technischen Universität Dortmund**

**Shehzad Saleem Khan (MSc)**

Geesthacht - Germany

2011



# Acknowledgement

This thesis is the account of three and a half years of research work, at Helmholtz Zentrum Geesthacht, Institute of Materials Research. This work would not have been possible without the help of many.

A few lines are too short to express my complete account of gratitude to my advisor, Professor Jörn Mosler. I wish to thank him for his constant support, encouragement, trust and all the fruitful discussions. I wish to thank him for his unique understanding and being such an attainable and likable teacher. I want to extend my appreciation to him for providing me the opportunity to follow and perform my ideas, and the nice working environment throughout my stay at HZG. His understanding and recognition of student's personality made my tenure as a doctoral candidate very pleasant. The team of senior colleagues that he assembled namely, Dr. Olaf Kintzel and Dr. Andriy Vishnevskyy have been my motivation and inspiration during the course of the project. It has been a distinct privilege for me to work with such brilliant minds.

I would also to express my sincere gratitude to Professor Nobert Huber for accepting me so readily as a new member at the Institute of Materials Research, supporting me constantly throughout the work and his helpful comments and discussions.

I had the opportunity to work in a very nice working environment at HZG amongst many good scientists and colleagues. I thank all of my colleagues, especially Dr. Mintesnot Nebebe, Dr. Ingo Scheider, Dr. Dirk Steglich, Dr. Alfred Cornec, Dr. Malek Homanyonifar and Baodong Shi. I am truly grateful for your support and your commitment to teamwork.

The last but not the least, I wish to thank my family for their unconditional support, love and encouragement, especially my dear friend, Friederike Buchholz, for giving me self confidence to achieve this goal.

Geesthacht, December 2011

Shehzad Saleem Khan



# Contents

<b>1</b>	<b>Motivation</b>	<b>1</b>
<b>2</b>	<b>Outline</b>	<b>3</b>
<b>3</b>	<b>Introduction to Low Cycle Fatigue</b>	<b>5</b>
3.1	Introduction to the fatigue of materials . . . . .	5
3.1.1	Brief history of fatigue: its technical and scientific im- portance . . . . .	5
3.1.2	Classification of fatigue damage . . . . .	6
3.2	Low cycle fatigue in structural analysis . . . . .	8
3.3	Empirical description of fatigue . . . . .	9
3.3.1	Approaches based on the applied stress amplitude . . .	9
3.3.2	Approaches based on the applied strain amplitude . . .	12
3.4	Multiaxial LCF in Metals . . . . .	13
<b>4</b>	<b>Experimental characterisation</b>	<b>15</b>
4.1	Aluminium alloys . . . . .	15
4.2	Production process . . . . .	16
4.3	Experimental results . . . . .	17
4.3.1	100 mm plate . . . . .	18
4.3.1.1	Tensile tests . . . . .	18
4.3.1.2	Round notched bars (RNB) . . . . .	21
4.3.1.3	Fatigue tests . . . . .	21
4.3.2	4 mm sheet . . . . .	25
4.3.2.1	Tensile tests . . . . .	26
4.3.2.2	Fatigue tests . . . . .	27
4.4	Microstructure . . . . .	32
4.4.1	Grains . . . . .	32
4.4.1.1	100 mm plate . . . . .	33
4.4.1.2	4 mm sheet . . . . .	34
4.4.2	Particles . . . . .	35
4.4.2.1	Particle level III . . . . .	36
4.4.2.2	Particle Level II . . . . .	37
4.4.2.3	Particle Level I . . . . .	37

---

4.5	Fracture mechanisms . . . . .	40
4.5.1	100 mm plate . . . . .	41
4.5.1.1	Uniaxial tension tests . . . . .	42
4.5.1.2	Cyclic tests . . . . .	42
4.5.2	4 mm sheet . . . . .	43
4.5.2.1	Uniaxial tension tests . . . . .	43
4.5.2.2	Cyclic tests . . . . .	46
4.6	Damage visualisation using synchrotron micro-tomography . .	49
4.6.1	Micro-structural characterisation using SR $\mu$ CT . . . . .	50
4.6.2	Experimental procedures . . . . .	52
4.6.3	Tomography set-up . . . . .	54
4.6.4	Results and Discussion . . . . .	55
4.6.4.1	Uniaxial tests . . . . .	56
4.6.4.2	LCF tests . . . . .	57
4.6.5	Concluding remarks - X-ray tomography . . . . .	61
<b>5</b>	<b>Modelling material damage by continuum mechanics</b>	<b>63</b>
5.1	Fundamentals . . . . .	63
5.1.1	The concept of internal damage variables . . . . .	63
5.1.1.1	Scalar damage variables . . . . .	64
5.1.1.2	Second-order damage tensors . . . . .	65
5.1.2	Principle of strain equivalence . . . . .	65
5.1.3	Modelling the evolution of damage . . . . .	66
5.2	Material law for ductile damage . . . . .	67
5.2.1	Elasto-plasticity . . . . .	67
5.2.2	Damage initiation - threshold of the stored energy . . .	68
5.2.3	Damage evolution . . . . .	69
5.2.4	Crack closure effect . . . . .	69
5.2.5	Meso-crack initiation . . . . .	70
5.3	Simulation Results . . . . .	70
5.3.1	Material parameters for plasticity model . . . . .	70
5.3.2	Material parameters for the damage model . . . . .	71
5.3.3	Simulation of fatigue life time of DLC-specimens . . . .	72
5.3.4	Lifetime prediction, RNB specimens . . . . .	73
5.4	Conclusions . . . . .	77
<b>6</b>	<b>A novel coupled damage model</b>	<b>79</b>
6.1	Fundamentals . . . . .	79
6.1.1	The ductile damage model . . . . .	80
6.1.2	The brittle damage model . . . . .	83
6.1.3	The coupled ductile-brittle damage model . . . . .	85
6.2	Parameter identification . . . . .	86
6.2.1	Calibration of the brittle damage model to Al2024 . . .	87

6.2.2	The approximation of the elasto-plastic hysteresis curve	88
6.2.3	The damage initiation phase . . . . .	90
6.2.4	The coupled ductile-brittle damage model . . . . .	91
6.3	Numerical examples . . . . .	92
6.3.1	Smooth round bar (DLC-specimen) . . . . .	92
6.3.2	Flat specimen . . . . .	96
6.4	Conclusions . . . . .	97
<b>7</b>	<b>Damage tolerance assessment of stiffened panels</b>	<b>99</b>
7.1	Adhesively bonded stiffened panels . . . . .	99
7.2	Application of the coupled ductile-brittle damage model . . . . .	101
7.3	Conclusions . . . . .	104
<b>8</b>	<b>Summary and Conclusions</b>	<b>107</b>
	<b>References</b>	<b>109</b>
	<b>List of Figures</b>	<b>115</b>
	<b>List of Tables</b>	<b>119</b>





# 1 Motivation

The Comet aircraft designed by de Havilland of England was a revolution when it first flew in July 1949 as it was the first commercial airliner ever built to use turbojet engines. The aircraft maker managed to minimise the aircraft weight and the fuel consumption to transport more passengers and freight. Unfortunately, after eighteen months of service, some of the aeroplanes went down. Intensive investigations followed to determine the origin of the crashes. A test, carried out on a full scale aircraft placed into a water tank to study the cabin pressurisation, revealed the formation of a fatigue crack from a rivet hole at a window corner that propagated to catastrophic failure.

This well known example in the history of aviation illustrates the modern philosophy of the aerospace industry: the desire to transport numerous passengers at reduced costs. One way to achieve this increase in performance is to minimise the weight of the aircraft itself and therefore reduce the fuel consumption. However, the investigations that followed the crashes pointed out first the necessity to validate both aircraft design and materials in terms of damage resistance and second, the importance of post crash investigations to clarify the origins of failure in order to prevent any fatal ruptures.

Traditionally made of aluminium alloys, the new generation of aircrafts, such as the A380, still contain 60% of aluminium, cf. Cambrésy (2006). High-performance materials like aluminium alloys are frequently employed in structural components of transportation vehicles (e.g., aeroplanes, automobiles and motorcycles). They have a high strength-to-weight-ratio and a high corrosion-resistance resulting in high efficiency. In particular, Al2024 is frequently used for components in the aerospace industry, e.g., for airframes of the fuselage of aeroplanes. This special aluminium alloy is known to be very damage tolerant and a good fatigue performer. Due to practical relevance, the material properties of aluminium alloys have been analysed extensively to assess their performance under single loading events (monotonic loading) as well as under repeated loading at low stress levels (high cycle fatigue, HCF).

Engineering structures such as aircraft fuselage panels are usually subjected to a number of loading incidents during service life which are often of cyclic nature like recurrent landing operations or alternate pressure loadings at high altitudes. In benign situations, the stress levels are comparatively low. How-

ever, during critical overloads, e.g. experienced during unpredictable mechanical events like tough landing operations, bad weather conditions, etc., the material may experience higher local stresses. Even though the bulk of the material may be below the yield limit, local flaws or inhomogeneities may increase the local stress level above the elastic regime, which may promote material degradation at higher stress levels (Low cycle fatigue, LCF). Thus, the experimental assessment of LCF behaviour of aluminium alloys is of great importance. Usually, a number of experiments have to be conducted under distinct loading conditions which is costly and time-consuming. Moreover, as empirical methodologies are inadequate for various scenarios, the demand for numerical models for the simulation of LCF is, thus, obvious. For this reason, a novel constitutive model suitable for the analysis of low cycle fatigue in high strength aluminium alloys is developed in the present thesis. It is based on a thorough material characterisation.

## 2 Outline

This thesis is structured in eight chapters.

Historically, many mechanical structures such as aircrafts and trains were readily affected by the fatigue phenomenon, therefore a brief account of these events is discussed in Chapter 3. This is followed by a general classification and fundamentals of fatigue analysis. Afterwards, the basics of experimental fatigue testing and the resulting empirical modelling are introduced.

Chapter 4 addresses the whole experimental characterisation. Thereupon, the experimental examinations are outlined. Foremost, a certain aerospace aluminium alloy is characterised w.r.t microstructure in two different material sources, i.e. plate and sheet. Furthermore, a new device to prevent buckling in the flat specimen is developed, which is compatible to the overall control setup. In the proceeding part, fracture mechanisms of Al2024 sheet and plate revealing the micromechanisms associated with damage are discussed. Non destructive testing methods for the visualisation of damage are introduced at the end of Chapter 4.

Chapter 5 is associated with the modelling of LCF. For that purpose, the fundamentals of continuum damage mechanics (CDM) are discussed first. This is followed by the material law proposed by Lemaitre & Desmorat (2005) used for the parameter identification of the ductile fatigue damage.

Since the model considered in Chapter 5 does not capture all relevant damage modes such as a quasi-brittle material degradation, a novel model is elaborated in Chapter 6. The performance of this model is demonstrated by comparing its predicted mechanical results to experiments (tensile tests, with and without notches).

Finally, the applicability of the novel model introduced in Chapter 6 is analysed for complex engineering structures. As a prototype of such a structure, a stringer-assembly is considered. Chapter 7 is completed by explaining fundamental principles of damage tolerance applied in the aircraft industry.



# 3 Introduction to Low Cycle Fatigue: Fundamentals and Methodology

## 3.1 Introduction to the fatigue of materials

As experimental evidence suggests, fracture of structures or machine components during regular operating conditions is caused mainly by fatigue, cf. Pineau (2010). The integrity of structures is and will remain one of the core issues posing an obstacle to industrial development. Its consequences could already be seen by the design of the Comet aircraft discussed in Chapter 1.

### 3.1.1 Brief history of fatigue: its technical and scientific importance

According to Schütz (2003), Braithwaite (1854) introduced the term “metal fatigue” in 1854. Despite this, Lemaitre (2001) reckons that Poncelet mentioned this term during an engineering lecture in Metz as early as 1839, and that Rankine used it in 1843. However, the knowledge of its causes was still limited at those times. Many thought that “metal fatigue” was caused by “crystallisation” of iron due to mechanical vibrations. As a consequence of its importance as an essential material phenomenon, a large amount of research was devoted to the subject of fatigue through-out the 20th century.

Clearly, with the progress in transportation, aircrafts along with other mechanical structures were a new subject of systematic studies concerning fatigue. One of the first serious accidents that occurred were those involving two Comet aircraft<sup>1</sup> in 1954. A more recent one was the crash-landing of a Boeing 737 in the famous Aloha accident in 1988, see Figure 3.1. It was assumed that the accident was caused by the formation of cracks due to fatigue in the assembly rivets area within the fuselage.

---

<sup>1</sup> Fighters aircrafts had suffered similar problems earlier but Comet was the first commercial aircraft reported with such an accident.



Figure 3.1: The severely damaged fuselage of the Aloha Airlines Boeing 737, following the accident on April 28, 1988

Table 3.1: Classification of fatigue (Dufailly & Lemaitre, 1995)

	Number of cycles to failure	Stress range $\sigma$	Strain ratio $\Delta\varepsilon^p/\Delta\varepsilon^e$	Energy ratio $\Delta W^p/\Delta W^e$
High cycle fatigue HCF	$> 10^5$	$< \sigma_y$	$\cong 0$	$\cong 0$
Low cycle fatigue LCF	$10^2$ to $10^4$	$\sigma_y$ to $\sigma_u$	1 to 10	1 to 10
Very low cycle fatigue VLCF	1 to 20	close to $\sigma_u$	10 to 100	10 to 100

### 3.1.2 Classification of fatigue damage

Fatigue damage is a kind of material damage which appears under cyclic load and can manifest itself in various ways depending upon the nature of the material, the type of loading and the temperature. A classification has been introduced by Dufailly & Lemaitre (1995) which describes a dependence upon the stress range and the number of cycles-to-failure range, as given in Table (3.1). Here, the following nomenclature is used:  $\sigma_y$  is the yield stress,  $\sigma_u$  is the ultimate stress,  $\Delta\varepsilon^e$  and  $\Delta\varepsilon^p$  are elastic and plastic strain amplitudes,  $\Delta W^e$  and  $\Delta W^p$  are the change in elastic and plastic energy due to cold work.

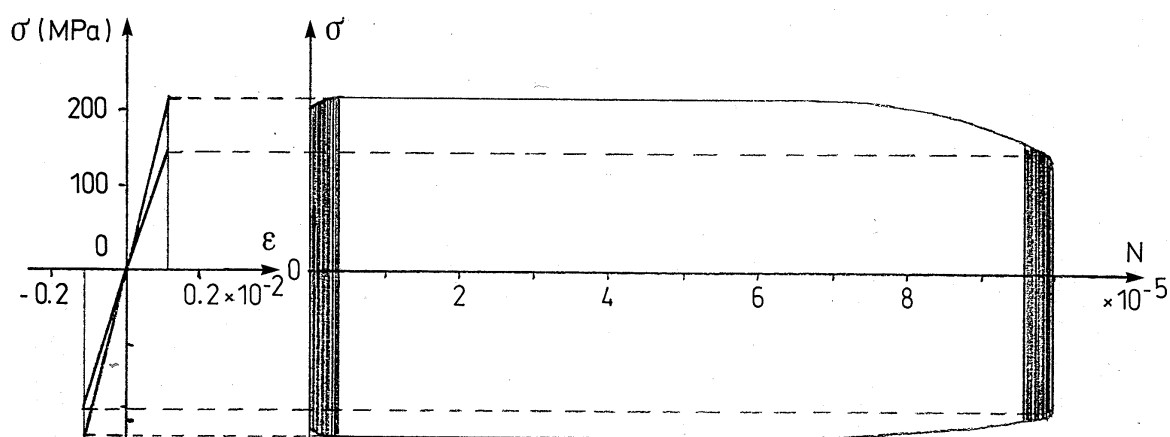


Figure 3.2: Cyclic tension-compression response for high cycle fatigue of A 316 stainless steel (Dufailly & Lemaitre, 1995)

When a material is loaded by a stress level  $\sigma$  which is significantly below the macroscopic yield stress ( $\sigma < \sigma_y$ ), the plastic strain is very small and is concentrated in the vicinity of microscopic defects. Consequently, the change in the macroscopic stored plastic energy  $W^P$  can be neglected in comparison to the reversible elastic part  $\Delta W^e$ . The number of cycles to failure is typically larger than  $10^5$ . This case of fatigue is called *high cycle fatigue* (HCF). Damage in HCF tests is a strongly localised phenomenon and it is brittle in nature. This strong localisation of damage is not always compatible with continuum mechanics for which damage is assumed to be uniformly distributed in the considered representative volume element. Even in the case of a uniform stress distribution, HCF microcracks always start from the surface boundary of the body. Later, microcracks grow within the interior and the development of a single macroscopic crack results from the coalescence of several microcracks. In Figure 3.2, a typical stress-strain response for HCF is given. It is possible to see stress-strain loops corresponding to the stabilised cycle and stress-strain loops corresponding to the cycle close to rupture. In the case of brittle damage and HCF damage, microplastically induced damage zones are considerably smaller compared to the dimensions of the specimen.

In the case when the stress level  $\sigma$  is larger than the yield stress ( $\sigma > \sigma_y$ ), damage develops together with the plastic strain after the incubation period preceding the phases of nucleation and propagation of microcracks. This mechanism of damage is manifested through the transgranular slipbands fields developed in large grains. Because of the high values of the stress, the number of cycles to failure is between  $10^1$  and  $10^4$ . This kind of fatigue is called *low cycle fatigue* (LCF). In the case of LCF, the energy change  $\Delta W^P$  is of the same order as  $\Delta W^e$ , see Table (3.1). The stress-strain response for LCF is given in Figure 3.3. It is possible to see that the drop of stress at the mesolevel

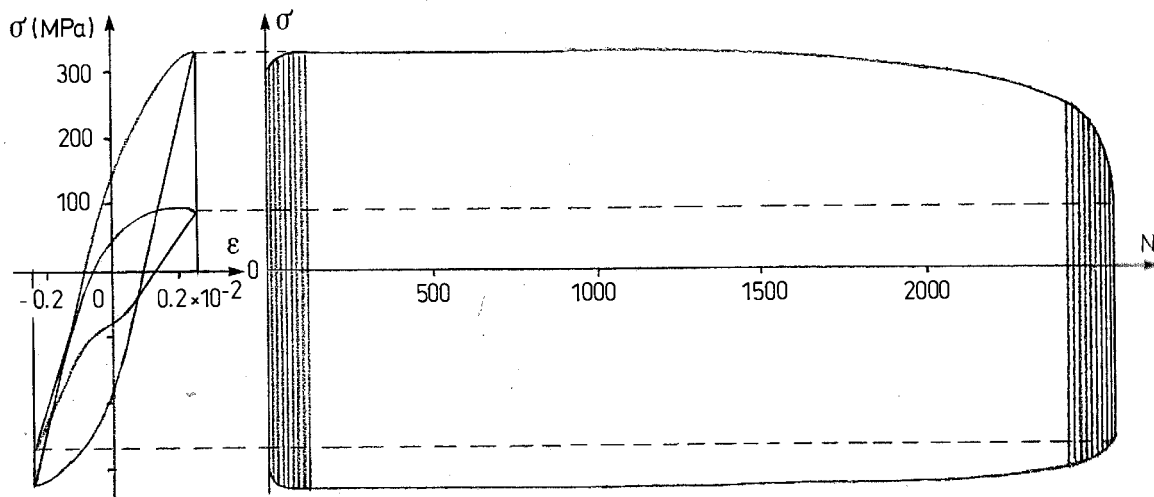


Figure 3.3: Cyclic tension-compression response for low cycle fatigue of A 316 stainless steel (Dufailly & Lemaitre, 1995)

occurs earlier compared to HCF, see Figure 3.2.

In the case when the stress level  $\sigma$  is close to the ultimate stress  $\sigma_u$ , the plastic strain is much larger than the elastic strain and the number of cycles to failure is very small (just a few cycles). This state is called *very low cycle fatigue* (VLCF).

### 3.2 Low cycle fatigue in structural analysis

While structures have been designed in the past based on ultimate load criteria or the damage tolerance under low strain amplitudes (HCF), the importance of LCF for structural members has only been noticed relatively recently. As mentioned in Section 3.1.2, LCF is always accompanied by relatively large plastic deformation. Although such deformation are certainly not desired in engineering structures, they cannot be avoided. Typical examples are given below:

- start-up and shut-down of power generator structures (thermal stresses), cf. (Polák, 1991);
- monolithic aluminium stringer assembly of an aircraft's fuselage, see Chapter 7, cf. (Meneghin, 2010);
- bad weather conditions/seismic activity (earth-quakes).

Clearly this list is not meant to be exhaustive. Accordingly, LCF is indeed of practical relevance. For this reason, it will be analysed in detail in this thesis.



### 3.3 Empirical description of fatigue

In the following, different well established modelling approaches for fatigue are briefly presented. In sharp contrast to the models presented in Chapter 5 and 6, they are purely empirical in nature. Particularly, thermomechanical considerations are not taken into account.

#### 3.3.1 Approaches based on the applied stress amplitude

First characterisation of fatigue life in terms of nominal stress amplitudes using experimental data was obtained from rotating bend experiments on smooth specimens, introduced by Wöhler (1858). He proposed a stress life approach where smooth test specimens were machined to provide a waisted cylindrical gauge length. After that, specimens were fatigue tested under plane bending, rotating bending, uniaxial tension-compression and tension-tension cyclic loading. The load was taken as a periodical function. A typical fatigue cycle of sinusoidal waveform is given in Figure 3.4. Here  $\sigma_{\max}$  and  $\sigma_{\min}$  represent the maximum and the minimum stress during one cycle,  $\sigma_m$  is the mean stress,  $\Delta\sigma$  is the stress range,  $\sigma_a$  is the stress amplitude,  $R$  is the stress ratio and  $A$  is the amplitude ratio. These parameters are related by (3.1).

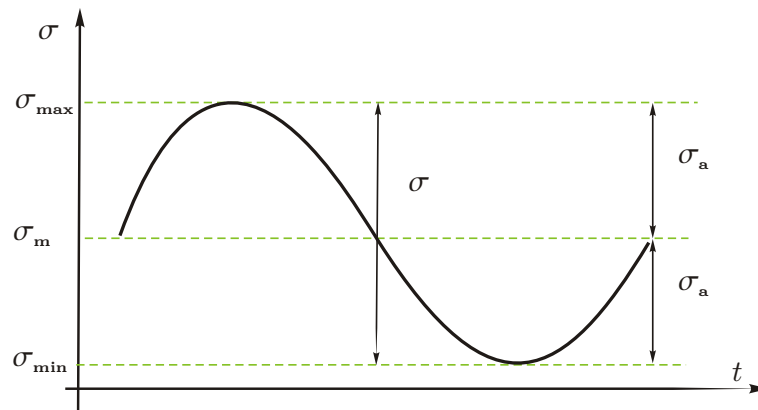


Figure 3.4: Characterisation of cyclic loads

$$\begin{aligned}
 \sigma_m &= \frac{\sigma_{\max} + \sigma_{\min}}{2}, & \Delta\sigma &= \sigma_{\max} - \sigma_{\min}, \\
 \sigma_a &= \frac{\sigma_{\max} - \sigma_{\min}}{2}, & R &= \frac{\sigma_{\min}}{\sigma_{\max}}, \\
 A &= \frac{\sigma_a}{\sigma_m} = \frac{1 - R}{1 + R}.
 \end{aligned} \tag{3.1}$$

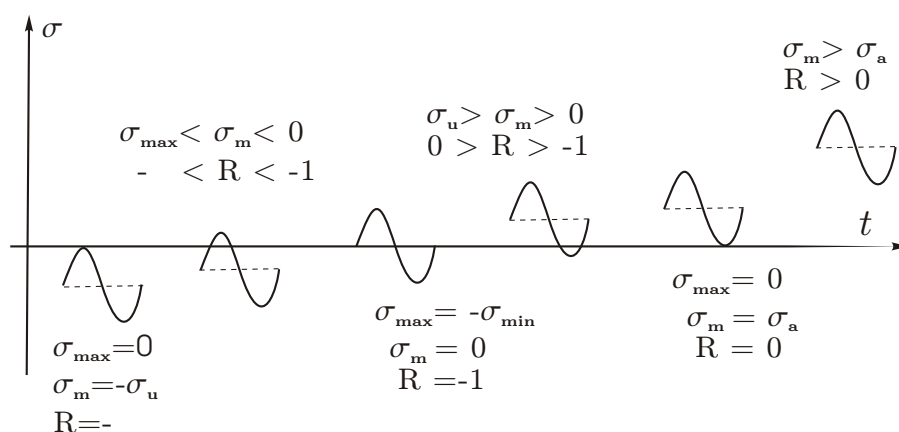


Figure 3.5: Different cyclic loading sequences, according to Haibach & Lehrke (1976)

Accordingly, it is possible to distinguish different loading forms for different values of the stress ratio and the mean stress (see Figure 3.5). Within the present thesis, only fully reversed loading ( $R = -1$ ) is considered.

To determine the shape of the so-called Wöhler curve, many different cyclic tests under constant amplitude loading conditions have to be undertaken, see Figure 3.6. A schematic representation of test results is shown in Figure 3.6 on a type of graph called *stress-life plot* (or S-N curve, or Wöhler curve), which shows the relationship between the amplitude (or maximum value, or mean value) of the applied stress and number of cycles up to fracture. Usually, the abscissa is the logarithm of the number of cycles  $N$ , while the vertical axis may be either the stress amplitude  $\sigma_a$  (or stress  $\sigma$ ) or the logarithm of  $\sigma_a$  (or logarithm of  $\sigma$ ).

Under constant amplitude loading conditions most steels and steel alloys exhibit a plateau in the stress-life plot. This plateau typically occurs beyond  $10^6$  fatigue cycles. When the load is below the plateau level, the specimen may be cycled indefinitely without causing macroscopic failure. The corresponding stress amplitude is called *endurance limit* or *fatigue limit*  $\sigma_e$ , and for most steels and copper alloys it is between 35% and 50% of the ultimate tensile strength  $\sigma_u$ . On the other hand, most aluminium alloys and some high strength steels which have been case-hardened by carburising do not generally exhibit a fatigue limit. For these materials, the stress amplitude decreases continuously with increasing number of cycles. For such cases, the stress amplitude which the specimen can support for at least  $10^7$  fatigue cycles represents a sort of an endurance limit.

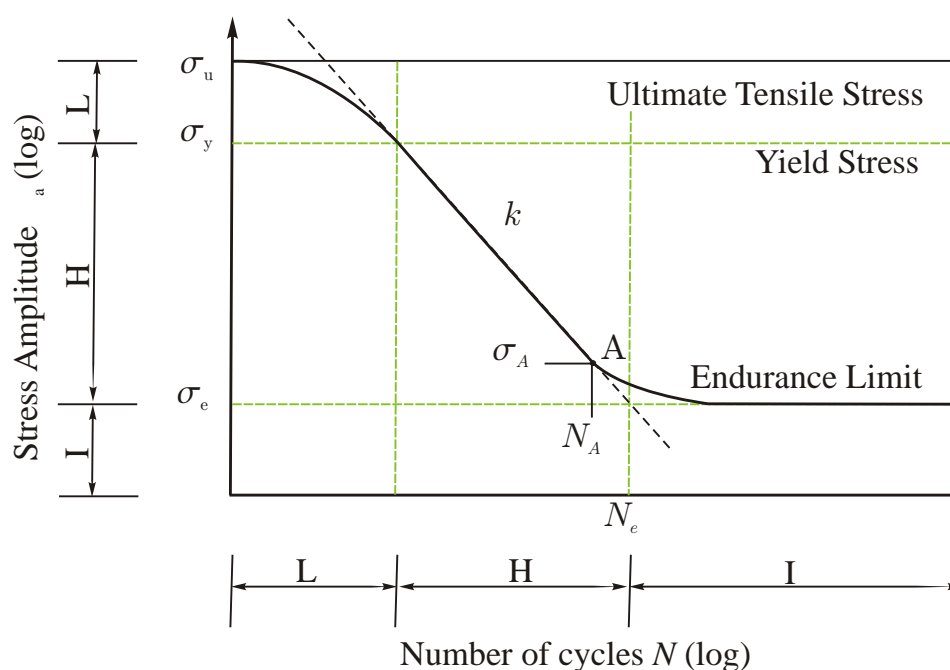


Figure 3.6: Typical Wöhler curve with stages: L - Low Cycle, H - High Cycle and I - Unlimited fatigue life, cf. Haibach & Lehrke (1976)

If the S-N curve is drawn on a log-log scale, with the stress amplitude plotted as a function of the number of load reversals, a linear relationship is commonly observed in the high cycle fatigue regime. Many authors proposed different equations for the description of the S-N curve (see Table (3.2)).  $B$ ,  $a$ ,  $b$ ,  $c$ , and  $\sigma_e$  in Table (3.2) are model parameters which can be determined from experiments. It bears emphasis that these models depend on the material, but also on the considered structure, i.e., they are not geometry invariant. Therefore, the S-N models are strictly speaking no material models.

Table 3.2: Equations for the description of S-N curve according to Haibach & Lehrke (1976)

1870	Wöhler	$\lg N$	$= a - b \cdot \sigma$
1910	Basquin	$\lg N$	$= a - b \cdot \lg \sigma$
1914	Stromeyer	$\lg N$	$= a - b \cdot \lg(\sigma - \sigma_e)$
1924	Palmgreen	$\lg(N + B)$	$= a - b \cdot \lg(\sigma - \sigma_e)$
1949	Weibull	$\lg(N + B)$	$= a - b \cdot [(\sigma - \sigma_e)/(\sigma_u - \sigma_e)]$
1955	Stüssi	$\lg(N)$	$= a - b \cdot [(\sigma - \sigma_e)/(\sigma_u - \sigma)]$
1963	Bastenaire	$\lg(N)$	$= a - \lg(\sigma - \sigma_e) - b \cdot (\sigma - \sigma_e)^c$

### 3.3.2 Approaches based on the applied strain amplitude

Alternatively to the work by Wöhler, the strain amplitude can be used as variable measuring the applied loading. Such an idea is briefly sketched in what follows.

Working independently on thermal fatigue problems, Manson (1953) and Coffin (1954) proposed a characterisation of fatigue life based on the plastic strain amplitude. They detected a linear relationship between the logarithm of the plastic strain amplitude and the logarithm of the number of load cycles to the failure of metallic materials. While in case of HCF, the resistance of a material against cyclic stress is considered of primary importance, the resistance against the cyclic plastic strain is much more important for low cycle fatigue. Thus, fatigue-life analysis in the LCF regime are conducted strain controlled and analysed using a Coffin-Manson relation (Lukas (1996)). The aforementioned approach can also be applied to the high-cycle fatigue region (Lukas & Klesnil, 1973), where plastic strain amplitudes are much lower and therefore also more difficult to measure and in particular to control.

Nowadays, the presentation of the fatigue life data in terms of strain can be considered as equally important and in some cases superior to the presentation in terms of stress. There is a variety of Coffin-Manson-type expressions modified/re-arranged by different working groups, some are given in (3.2).

$$\begin{aligned} \frac{\Delta \varepsilon^{\text{pl}}}{2} &= \varepsilon'_f \cdot (2N_R)^c && \text{(Manson, 1953)} \\ \text{where } -0.7 &\leq c \leq -0.5 \\ \varepsilon^{\text{p}} N_R^\alpha &= M && \text{(Pisarenko \& Naumenko, 1982)} \\ \varepsilon^{\text{pa}} &= \varepsilon'_f \cdot (2N_R)^c && \text{(Polák, 1991)} \\ N_R &= \left( \frac{\Delta \varepsilon^{\text{p}}}{C_1} \right)^{-\gamma_1} && \text{(Chaboche \& Lemaitre, 1994)} \\ N_R &= \left( \frac{C_{\text{MC}}}{\varepsilon^{\text{p}}} \right)^{\gamma_{\text{MC}}} && \text{(Lemaitre \& Desmorat, 2005)} \\ \text{where } C_{\text{MC}} &\approx 2\varepsilon^{\text{pR}} \quad N_R \leq 10^3 \end{aligned} \tag{3.2}$$

It bears emphasis that analogously to the approach originally advocated by Wöhler, the models summarised in (3.2) depend also on the geometry of the considered structure and consequently, they are strictly speaking no material models. Approaches not showing this disadvantage will be elaborated in Chapter 5 and 6.

### 3.4 Multiaxial LCF in Metals

Assessing mechanical components against fatigue is a complex problem that has to be properly addressed during the design process in order to avoid catastrophic failures. An understanding of multiaxial loading is clearly necessary in order to have an approach which is applicable to real industrial components, which are not loaded in the nice convenient ways that is chosen in the laboratory. In more detail, when engineering materials are subjected to time-variable loading, they can fail due to fatigue even without any evident large-scale plastic deformation altering the process zone (and this holds especially in the medium/high-cycle fatigue regime). Moreover the complex geometries of real mechanical assemblies favour the initiation of fatigue cracks due to stress concentration phenomenon arising from the geometrical features of the components themselves. Unfortunately, all such phenomena cannot be captured by the purely empirical descriptions of fatigue presented in Section 3.3.2. For this reason, a novel physically sound constitutive model is derived in Chapter 6 and implemented in a finite element program. This model is based on the thorough material characterisation elaborated in Chapter 4.



## 4 Experimental characterisation

The basic concepts needed for understanding and describing metal fatigue are discussed in this chapter. Focus is on metallurgical and mechanical aspects. *Metallurgical descriptions* are concerned with the state of the metal before, during and after the application of fatigue loads, and are concerned with the study of metal fatigue mechanisms. *Mechanical descriptions* deal rather with the kinds of mechanical responses to a given set of loading conditions like number of load cycles required to cause failure. The last part of this chapter explains the detection of damage in specimens subjected to low cycle fatigue by a distinct non-destructive inspection technique.

### 4.1 Aluminium alloys

Aluminium, the second most plentiful metallic element on earth, became an economic competitor in engineering applications as recently as the end of 19th century. The emergence of industrial developments, by demanding product characteristics consistent with the unique qualities of aluminium and its alloys, greatly benefited growth in the production and use of this metal.

Both wrought and cast aluminium alloys have found wide use in transportation industry. In automotive industry aluminium sand, die and permanent mold castings are critically important in engine construction; engine blocks, pistons, cylinder heads, intake manifolds, crankcases and carburetors etc. In trucks because of weight limitation and a desire to increase effective payloads, manufacturers have intensively employed aluminium alloys in frames, floors, roofs, cross sills, and shelving. As far as aerospace industry is concerned aluminium alloys are used virtually in all segments of the aircraft, missile, and spacecraft industry - in airframes, engines, accessories, and tankage for liquid fuel and oxidisers. Aluminium is widely used because of its high strength-to-density ratio, corrosion resistance and weight efficiency, particularly for compressive stresses (Davis, 1993). Nowadays, aluminium alloys are further developed to satisfy the demands for higher strength, improved damage resistance as well as reduction of production cost. Weldable aluminium alloys like 2xxx, 6xxx and 7xxx have been extensively tested and analysed to improve the aforementioned properties. Amongst these, Al-Cu alloys belonging to 2xxx series e.g. 2024 in

“T351” heat treatment are considered as standard, cf. Schmidt (2005). This chapter focuses on Al2024 in two different forms i.e. thick plate and thin sheet. They have copper (Cu) as major alloying element and hardening is achieved by ageing. Although damage tolerance is enhanced by copper, its high content in 2024 results in the creation of brittle intermetallics which later act as initiation sites for damage, see Section 4.5.1.2 and 4.5.2.2.

## 4.2 Production process

Al2024–T351 is an aluminium alloy renowned for its good mechanical properties, its light weight characteristics and its resistance to corrosion. To produce the considered aluminium alloy, the refined aluminium already containing, as impurities, traces of iron, silicon and chromium, is molten into furnaces and the alloying elements, copper, magnesium and manganese are added. As mentioned earlier, the main alloying element in the 2xxx series is copper, while magnesium and manganese are also introduced in order to improve the quenching properties. The material’s chemical composition (as specified by the supplier Alcoa Inc., cf. (ALCOA<sup>®</sup>, 1995)) is given in Table (4.1)<sup>1</sup>.

Table 4.1: Chemical composition limits of Al2024 alloy. Maximum value is given, if range is not shown

Element	Si	Fe	Cu	Mn	Mg	Cr	Zn	Ti	Others	Al
Wt.%	0.50	0.50	3.8-4.9	0.30-0.9	1.2-1.8	0.10	0.25	0.15	0.05	Balance

Initially, the material is cast into big ingots, usually 300 to 600 mm thick, 1 to 3 mm wide, and several meters long. Afterwards, it is heated to properly homogenise the microstructure of the material, even though, as it will be seen in (Section 4.4), it does not prevent the formation of coarse particles inside the rolled material. Considering the rolling process, the following three directions are considered, see (Figure 4.1).

- L (Longitudinal) direction: the direction of the hot-rolling process
- T (Transverse) direction: the direction normal to the rolling direction, in the rolling plane
- S (Short Transverse) direction: the direction normal (thickness) to the rolling plane

<sup>1</sup>The composition remains the same for both the sheet and the plate.



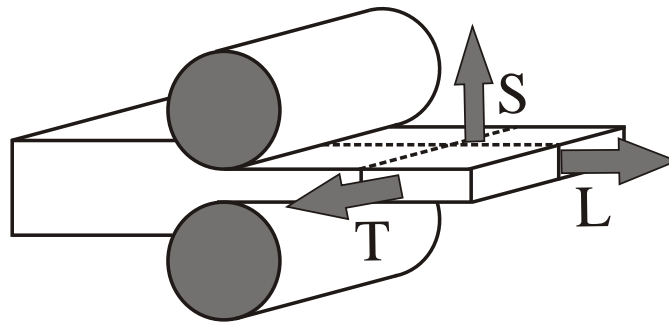


Figure 4.1: The three main directions of the material as defined with respect to the rolling process

Once the rolling process is completed, the material is heat-treated (in this case solution heat treatment). The purpose of this heat-treatment is to improve the mechanical properties. In the present case, the alloy undergoes a natural ageing, i.e. it is left at room temperature for at least 5 days. The treatments exposed above are designated by the code “T351”, where, in particular, “T3” means that the material has been solution heat-treated, air-quenched, and cold worked, while the last two digits “51” mean that it has been stress relieved by cold stretching.

### 4.3 Experimental results

The alloy under consideration was analysed in form of 100 mm (Figure 4.2(b)) thick plates and 4 mm thin (Figure 4.2(a)) sheets. To study the mechanical properties in S-direction, thick plates had to be analysed. Considering the S-orientation, specimens were taken in thickness direction around the centre position (see Figure 4.2(b)) and were equally located across the width of the sample also near the surface to be able to detect any possible differences in microstructure. Due to its importance for applications in aerospace industry, 4 mm thin sheets were also included in the analysis. As it will be evident from the later sections, these two materials have different mechanical properties, which will be described in two sub chapters. For more details about the analysis techniques used for the microstructure and the tests, see Brocks & Heerens (2002); Quan et al. (2004).

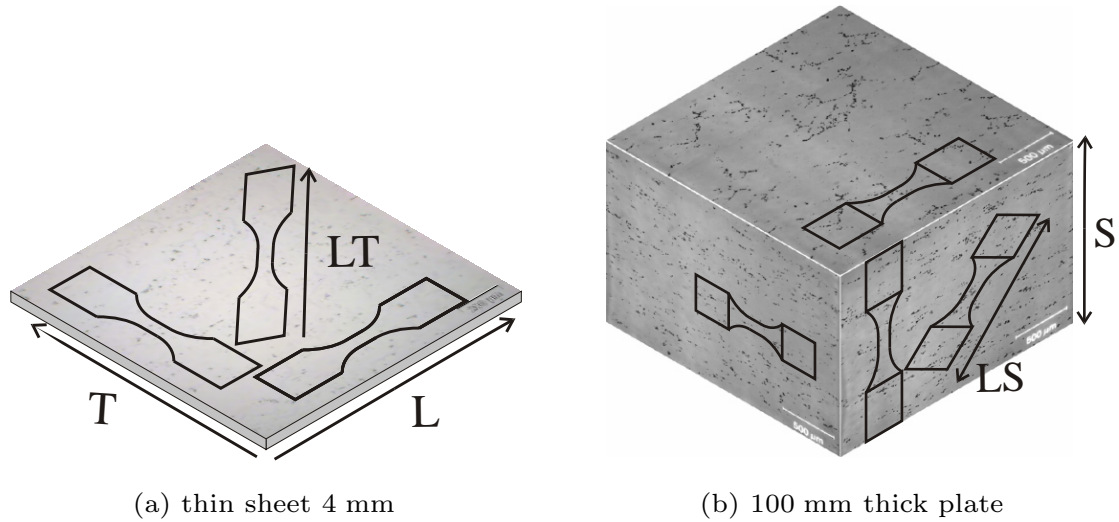


Figure 4.2: Locations of the specimens extracted from the 4 mm thin sheet and the 100 mm thick plate

### 4.3.1 100 mm plate

Problems arise, when thick plates are needed for machined components: in this case, the mechanical properties in the thickness direction become very important. Characteristic parts include deep channels, bulkheads, or other components where the part depth is oriented in the plate thickness direction.

In the past, a 100 mm plate has been extensively studied by colleagues at HZG (Steglich et al., 2008; Quan et al., 2004). These studies, however, were confined to the uniaxial tensile behaviour only.

#### 4.3.1.1 Tensile tests

At the start of the experimental characterisations, tensile tests were performed. The specimen for this test has a round cylindrical shape, with diameter  $d_0 = 10$  mm. A clip-gage has been used to measure the relative displacement  $\Delta l$  between two points on the length of the specimen. The distance between these two point is, in the undeformed state,  $l_0 = 50$  mm.

In Figure 4.3 and Table (4.2) the results of tensile tests performed for the three main directions of the material are exposed. The test performed in the LS-direction was made upon a specimen taken along an axis with inclined  $45^\circ$

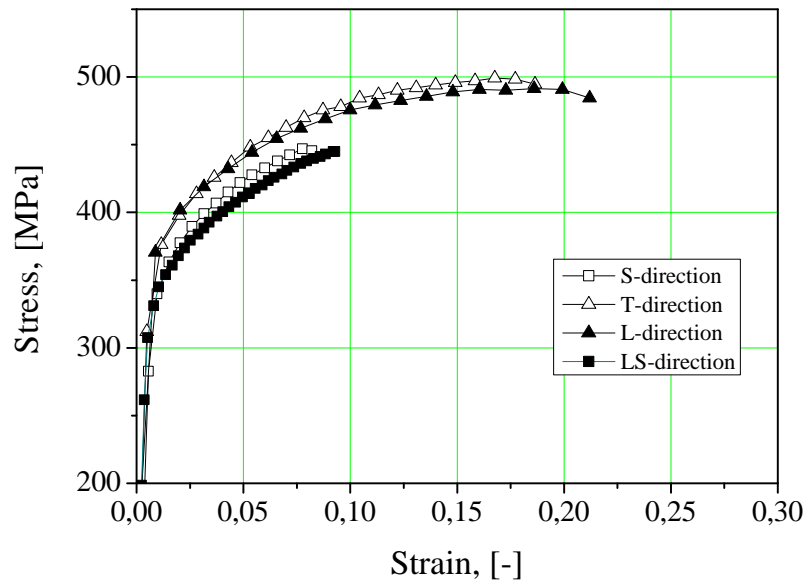


Figure 4.3: Tensile tests of the standard round bar specimen extracted from the 100 mm plate

Table 4.2: Results of the static test for the L, T and S-directions taken from 100 mm plate, with  $l_0=50$  mm

	L	T	S
Offset yield strength $R_{p\ 0,2}$ (MPa)	338	318	299
Tensile Strength $R_m$ (MPa)	485	495	446
Failure strain $\varepsilon_f$	0.212	0.186	0.086

to the L-direction (Figure 4.2(b)), in the LS-plane<sup>2</sup>. From Figure 4.3, it can be noticed that the yielding behaviour is almost the same for L and T-direction, while for S-direction the difference is more pronounced, but still small. Above all, the greatest difference is in the yielding point: S-direction yields sooner than the other two, but afterwards this difference in the yielding behaviour narrows down again (see Table (4.2)). The negligible anisotropy in the yielding behaviour is also confirmed by the small ovalisation of the specimen at the end of the test. In Table (4.3) the data about the final shape of the section of the specimens are shown: the section is always slightly elliptical and, in the case of L and T-direction, the shortest diameter  $d_{\min}$  was always found in the S-direction. It is also evident that, the ovalisation for S-direction is an order of magnitude smaller than the behaviour of L and T-directions, respectively.

Table 4.3: Out-of-roundness of the section of the specimens (100 mm plate) at the end of the test.  $d_{\max}$  is the longest diameter of the section,  $d_{\min}$  the shortest and  $d_0$  the initial diameter

Loading Direction	T	L	SL	S
$(d_{\max} - d_{\min})/d_0$	0.017	0.022	0.026	0.004

However, the main anisotropy of the material is evidently in the fracture behaviour. The S-direction appears to be much more brittle than the other two: at the fracture point there is an elongation of 21.2% and 18.6% for L and T-direction respectively, but only 8.6% for S-direction. It was observed that in every direction the material fails by unstable fracture without showing almost any local necking.

The above considerations, lead to the characterisation of an almost isotropic yielding behaviour, whereas the fracture process is rather anisotropic. To be more precise, all properties of the material are at least axisymmetric with respect to the S-direction, while the yielding characteristics are completely isotropic. This hypothesis will be also supported by the microstructure analyses Section 4.4.

<sup>2</sup>Since no considerable scatter could be detected ( $\pm 1$  kN), only mean values are plotted which are representative for each direction by averaging the data of three experimental tests. Throughout this thesis engineering stresses and strains are taken.

### 4.3.1.2 Round notched bars (RNB)

To study the fracture behaviour more closely, notched specimens are used. One of these specimens is formed like an axisymmetric bar with a circular notch at the centre. In Figure 4.4(a) the relevant dimensions of the two specimens considered are shown: they both have the same diameter at the root of the notch  $d_0=10$  mm and the same total external diameter  $D=18$  mm, while the main difference is in the radius of the notch. In one case  $r = 2$  mm and in the other  $r = 10$  mm. For these specimens, the variation of the diameter  $\Delta d$  has been measured, because the results are more significant compared to elongation in loading direction.

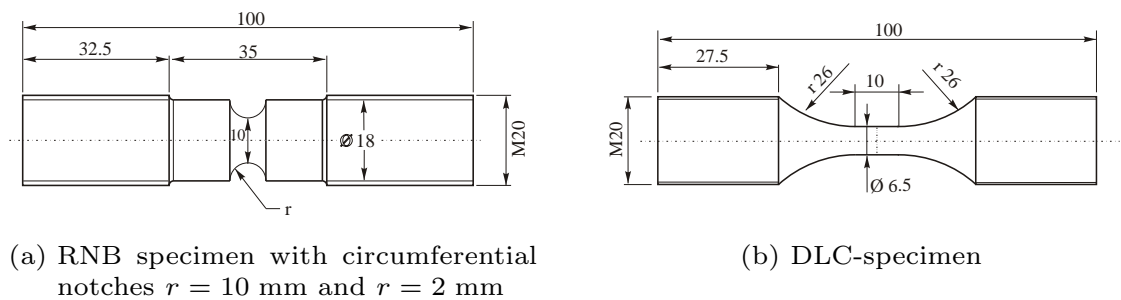


Figure 4.4: Specimen geometries for smooth and notched round specimen (100 mm plate)

In Figure 4.5 the results of the experiments are shown. Since points related to failure are subjected to large scatter, they have been marked for each test. No specimen in T-direction has been tested, because its behaviour is expected to be very similar to that of L-direction. From these data it can be seen that the radius of the notch has almost no influence on the diameter reduction of the specimen  $\Delta d_{\max}$  at fracture, but only on the maximum load. This has been qualitatively verified in many experiments: the sharper the notch, the higher the maximum load, cf. Figure 4.6. Overall, the S-direction shows a much more brittle behaviour than the L-direction<sup>3</sup>.

### 4.3.1.3 Fatigue tests

For the fatigue tests, two types of specimens (see Figure 4.4) were tested, including the so-called *Damage Low Cycle specimen* (DLC, smooth round bar) and the round notched specimen as discussed in the former section. DLC-specimens were designed for tension-compression tests showing a stress state

<sup>3</sup>Note that 4 mm notched round bars have been uni-axially tested to show the general effect of tri-axiality. However, they have not been included in the fatigue experiments.

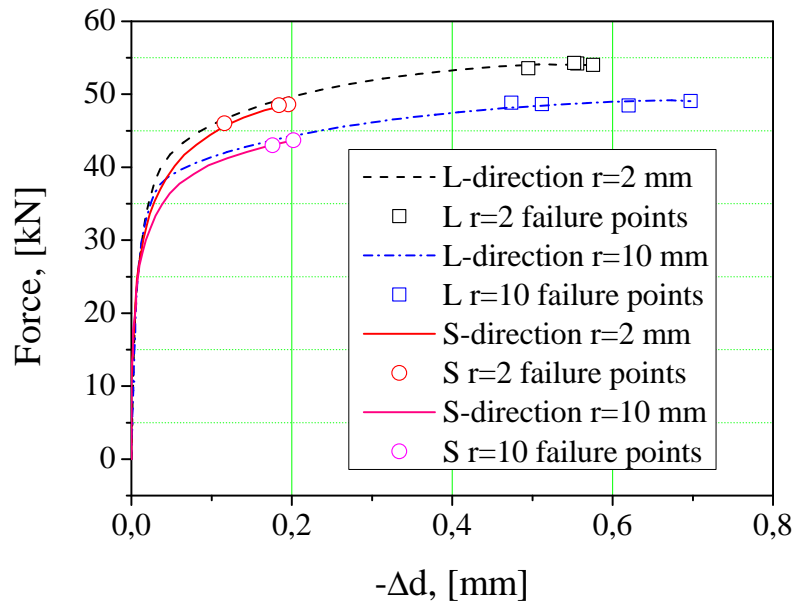


Figure 4.5: Experimental results of the round notched bars (RNB) taken from the 100 mm plate

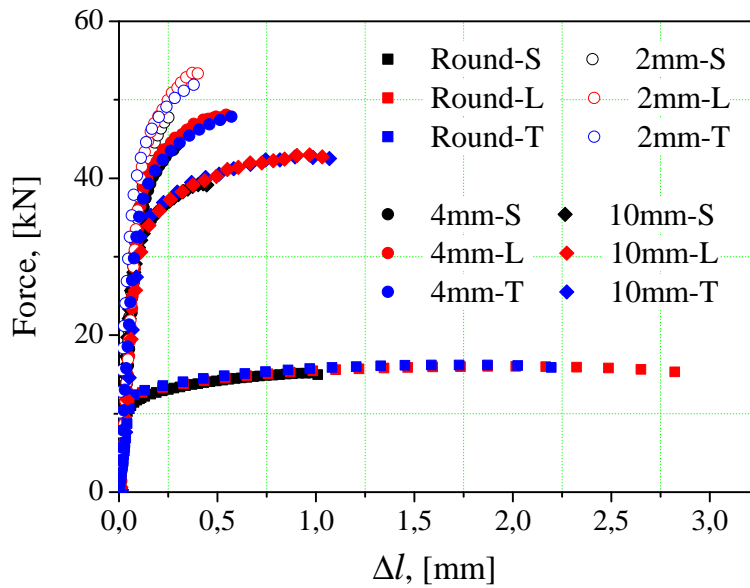


Figure 4.6: Force vs elongation experimental results of the notched round bars taken from the 100 mm plate, (S, L and T-direction) compared to that of round specimen, see Figure 4.4(a)

close to the uni-axial one (see Figure 4.4(b)). The specimens dimensions were taken from the ASTM E 606 standard test method (ASTM, 1998), with the following modifications: (i) a shorter gauge length to prevent buckling due to high compression straining; (ii) design of a new gripping for tension-compression testing.

As mentioned before, a multi-axial stress state can be achieved by various methods. The most common one is geometrical induced (see Section 3.4). To take this effect into account, circumferential Round Notch Bars (RNB) with various radii were designed to achieve a variation of the stress state in the middle cross section of the specimen (see Figure 4.4(a)) (same specimens were also used for uniaxial tensile tests). The geometry of the RNB specimens was designed similar to that in Pironi et al. (2006). All specimens were cut from the same plate of Al2024-T351 in S-direction and they were mechanically treated with a turning machine. The length of the specimens is equal to the thickness of the plate. Hence, the effective measuring length is associated with the mid-plane of the plate under investigation. The surfaces of the specimens were ground and mechanically polished in the direction of loading. The final polishing was performed with a diamond paste showing  $1\mu\text{m}$  grains.

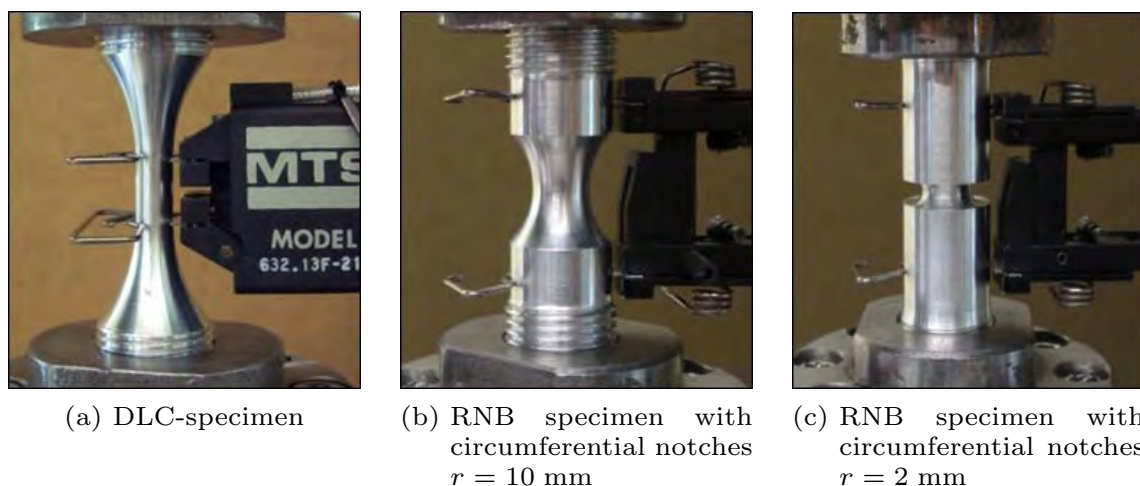


Figure 4.7: Attachment of the strain gauge to the specimen extracted from the 100 mm plate

The fatigue experiments were conducted on a 160 kN servo-hydraulic testing machine Schenck H160. Specially designed gripping of the testing setup and clamping threads of the specimens allow for reversal loading and avoid slipping during compression. The cyclic tests in all cases were performed displacement-controlled. The displacement was measured using an extensometer attached to the working distances in the case of the DLC-specimen in Figure 4.7(a). For the RNB-specimen in Figure 4.7(b) and Figure 4.7(c), the extensometer

was attached to the specially manufactured grooves.

A symmetric cycle ( $R = -1$ , see Figure 3.5) based on a triangular wave shape was imposed with various displacement amplitudes  $\Delta l$ . The time period was not varied ( $T=100$  s,  $f=0.01$  Hz). This very low frequency was chosen in order to obtain a better resolution of the load-displacement curve. In addition, a higher frequency can cause the specimen to heat up. All tests were conducted until complete failure (separation of the specimen into two parts). Time-force-displacement responses during the tests were recorded with a digital acquisition device.

Within the present thesis, focus is on the application of a certain CDM approach (Chapter 5) to the analysis of LCF in Al2024. For this reason, the experiments were reduced to such a number that the determination of a common trend was made possible. However, statistically-relevant quantitative data could not be obtained. To check for a certain reliability, some experiments were repeated under identical loading conditions. For the modelling purposes only selected experiments have been used. The results of the experiments are summarised in Table (4.4) below and the detrimental effect of triaxiality on the lifetime is shown in Figure 4.8.

Table 4.4: Matrix of LCF experiments conducted on specimens extracted from 100 mm plate

Specimen	Notch [mm]	Gauge length [mm]	Range of $\Delta l$ [mm]	Number of specimens
DLC	-	10	0.01-0.4	14
RNB	2	25	0.025-0.11	10
RNB	10	25	0.075-0.1875	10

The experimental determination of various stages of a specimen's life i.e. damage initiation and evolution etc. is aided by the analysis of the macroscopic response. Similar to many metallic materials subjected to cyclic loading, the stabilisation of the mechanical response is achieved for Al2024 after several cycles. After the stabilisation stage, mechanical degradation is observed (Figure 4.9(a), Pt.1). Following Lemaitre & Desmorat (2005), this is usually related to a critical value of the stored plastic energy (dislocation density). The subsequent degradation of mechanical properties results in a decrease of the maximum stress. Evidently, it is associated with the evolution of damage (Figure 4.9(a), from Pt.1 to Pt.2). Experimental observations show that visible macrocracks appear on the surface of the DLC-specimen after Pt.1 during a



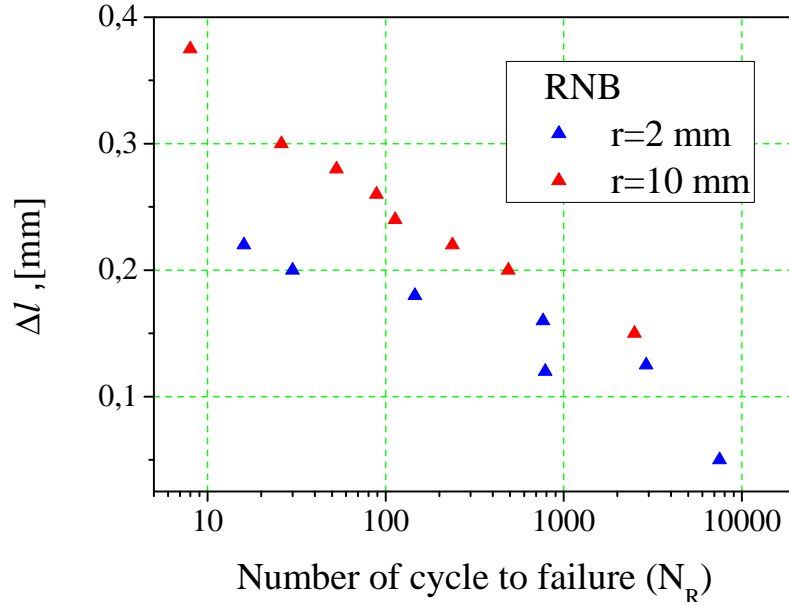


Figure 4.8: Experimental lifetime of specimens with  $r=2$  mm and  $r=10$  mm round notched bars (RNB) taken from the 100 mm plate, see Figure 4.4(a)

relatively small number of cycles. This is affiliated with the rupture of specimen (Figure 4.9(a), Pt.2). It is seen that the stage of cyclic damage (between Pt.1 and Pt.2, Figure 4.9(a)) is short compared to the plastic regime (from the beginning up to Pt.1).

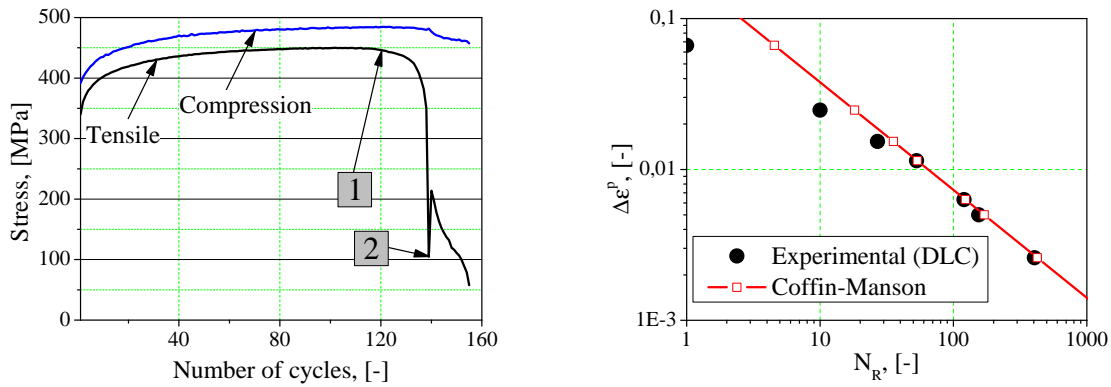
The total fatigue life  $N_R$  is the sum of the number of cycles necessary to initiate aforementioned mesocrack  $N_D$  and the number of cycles necessary to propagate the crack until final failure  $N_E$  (as in 4.1).

$$N_R = N_D + N_E . \quad (4.1)$$

Finally, the Coffin-Manson plot is given (Figure 4.9(b)), which shows a good fit. The results of these experiments w.r.t lifetime are discussed in detail in the next chapters (Chapter 5, 6).

### 4.3.2 4 mm sheet

Sheets are included in this study for their relevance in the industrial applications, especially aerospace structures. Hence, flat specimens were machined from a rolled Al 2024- T351 sheet of 4 mm thickness (Figure 4.2(a)) for each of the two directions with respect to the sheet's rolling direction (L 'Longitudinal' and T 'Transversal', perpendicular to the rolling direction).



(a) maximum tension and compression stresses in a particular test ( $\Delta\varepsilon^P = 0.0063$ ;  $N_R = 156$ ) (b) amplitude of plastic strains  $\Delta\varepsilon^P$  versus number of cycles to rupture  $N_R$

Figure 4.9: Mechanical response of DLC-specimens extracted from a plate having a thickness of 100 mm (S-direction)

The shape of the fatigue specimens has been chosen to minimise buckling during fatigue tests conducted under a negative strain ratio (Milan et al., 1988), see Section 4.3.1.3. The shape and the dimensions of the specimen are depicted in Figure 4.10.

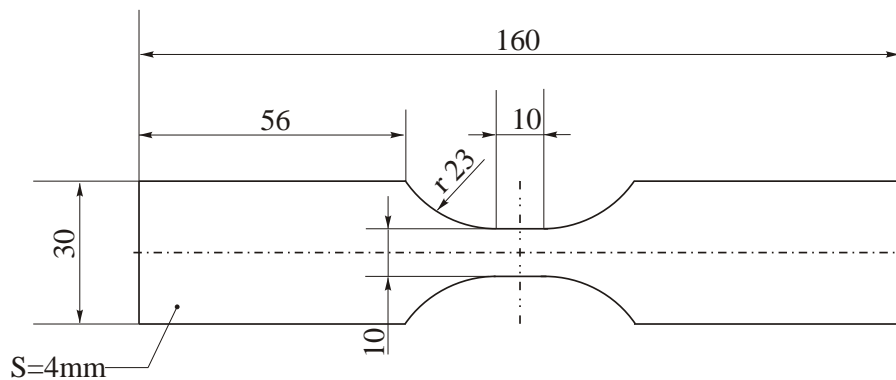


Figure 4.10: Flat specimen geometry extracted from 4 mm sheet used in the fatigue tests

#### 4.3.2.1 Tensile tests

The tensile tests were performed under displacement control using a mechanical Zwick Roell 1484 testing machine (maximum force 200 kN) with a constant

cross head speed of 0.5 mm/min. Grips were carefully aligned with the aid of an alignment fixture. An extensometer with gauge length of 8 mm (attached to the specimen on the sides) (see Figure 4.12(a)) was used to measure the displacement in loading direction, since the measurement of cross-head travel does not accurately measure the deformation of specimens. Another reason for attaching a clip gauge across the specimen is to measure the displacement close to the region of interest with high sensitivity. Load-displacement responses were recorded using DASYLab<sup>®</sup> software. The damage localisation was always inside the respective gauge length. The engineering stress was determined as the measured force at the clamp divided by the cross-sectional area (undeformed) at the centre of the specimen.

Table 4.5: Mechanical properties of 4 mm sheet of Al2024-T351 (uniaxial tensile loading), see Figure 4.2

Tensile direction	Yield stress $R_{p\ 0,2}$ (MPa)	Tensile Strength $R_m$ (MPa)	Fracture strain $\epsilon_f$ (-)
L	369	473	0.31
T	325	468	0.30
LT	330	468	0.29

Table (4.5) summarises the characteristic quantities obtained from the uniaxial tests on smooth flat specimens, namely the yield stress (see Figure 4.13), tensile strength and fracture strain in the 3 loading directions of the sheet: L (longitudinal), LT ( $45^\circ$ ) and T (Transversal). Longitudinal specimens presented a higher value of yield strength, ultimate strength and total elongation. All show a similar ductility. The fracture strain lies between 0.31 and 0.29 (see Figure 4.11), where the highest was measured in L-direction. In comparison to the DLC-specimen extracted from the 100 mm plate, flat specimens have a higher yield stress but a lower tensile strength. Although, the ductility and fracture strain have been higher in flat specimens as compared to round bars extracted from (100 mm), this is mostly related to geometrical effects.

#### 4.3.2.2 Fatigue tests

As discussed in Section 4.3.1.3, surface roughness affects fatigue life. For this reason, the edges of the specimen especially around the radii, were reworked by hand using a cylindrical abrasive pencil and then polished lengthwise by hand using a rubbing compound. This provided protection against edge cracks. The cyclic tests have been conducted on a Schenck 160 kN servohydraulic testing

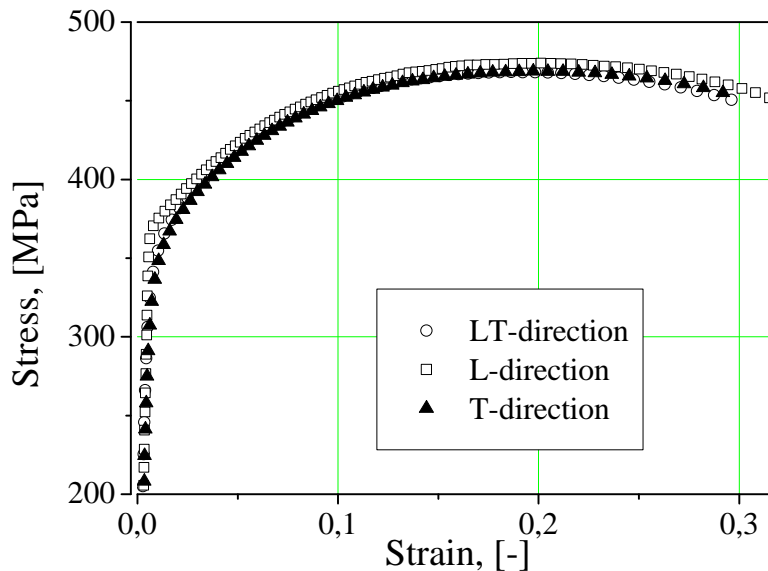


Figure 4.11: The response of the material at uni-axial tensile loading (4 mm sheet)

machine, at room temperature with triangular loading steps at the standard frequency (identical procedure as used for the DLC/RNB specimens).

The determination of the fatigue properties in thin sheets is extremely problematic due to the high risk of buckling of the sheet during compression, cf. (Fredriksson et al., 1988; Biswas, 1993). An anti-buckling guide was used to prevent this, allowing the specimen to “lean” against the guide without buckling. A floating guide technique is used for the buckling guide system, Figure 4.12. A Teflon (PTFE) film of 0.5 mm thickness is inserted between the buckling guides at both sides of the specimen. By these means it could be ensured that the axial freedom of movement of the specimen with the buckling guide is restricted as little as technically possible while at the same time ensuring that buckling is prevented.

With the use of the anti-buckling guide, there is a possibility that the specimen may be reinforced due to higher bolt torque or higher friction between the teflon layer and the specimen, see Figure 4.12. To check this, an experimental test series was done where only the first half-cycle at the highest amplitude (both in T and L-direction) was compared to a monotonic tensile test with the anti-buckling guide. As evident from Figure 4.13, the macroscopic behaviour is indeed not disturbed profoundly by the use of the anti-buckling guide.

The complete characterisation of the material response requires the continuous

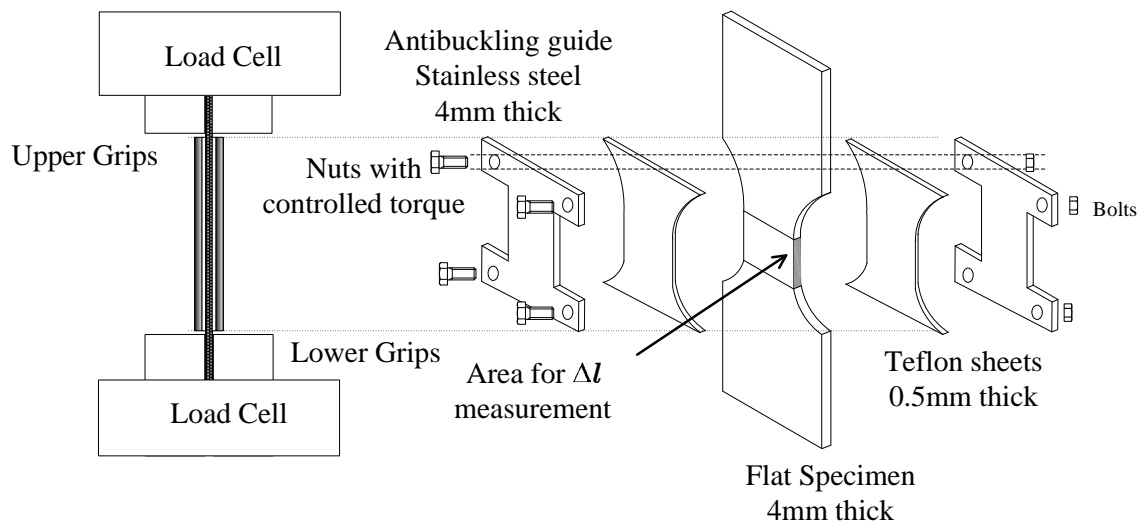


Figure 4.12: Anti-buckling support during LCF experiment, the extensometer (gauge length 8 mm) is attached to the edges of the specimen (4 mm sheet)

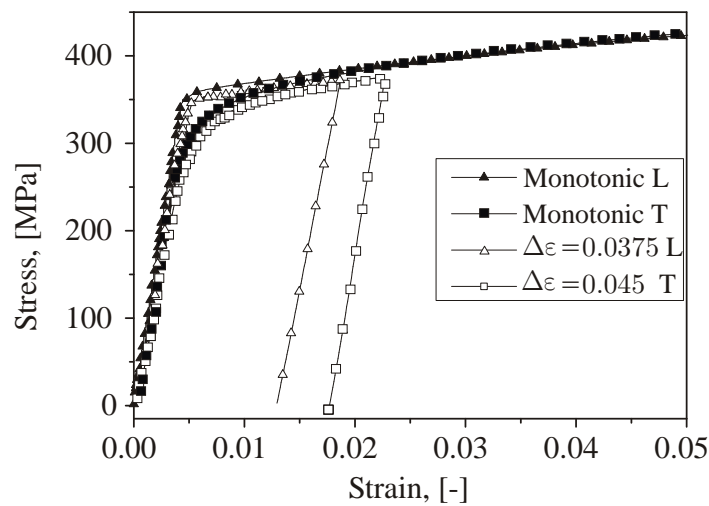


Figure 4.13: Independence of the experiments of the anti-buckling guide: macroscopic behaviour during the first half-cycle of a cyclic test (flat specimen extracted from 4 mm sheet) using the anti-buckling guide compared to that of the monotonic tensile test without the anti-buckling guide

monitoring of the stress amplitude. During the initial phase of cyclic deformation, (rapid) cyclic hardening occurs, giving rise to an increase in peak stresses  $\sigma_p$ , (Figure 4.14), followed by an extended regime of cyclic saturation during which stresses and strains attain steady state values  $\Delta\varepsilon_{p,s}$  and  $\Delta\sigma_s$  (Figure 4.15(b)). Finally, fatigue damage softening sets in. In this connection, two essential stages can usually be distinguished, mesocrack initiation and crack propagation (see 4.1).

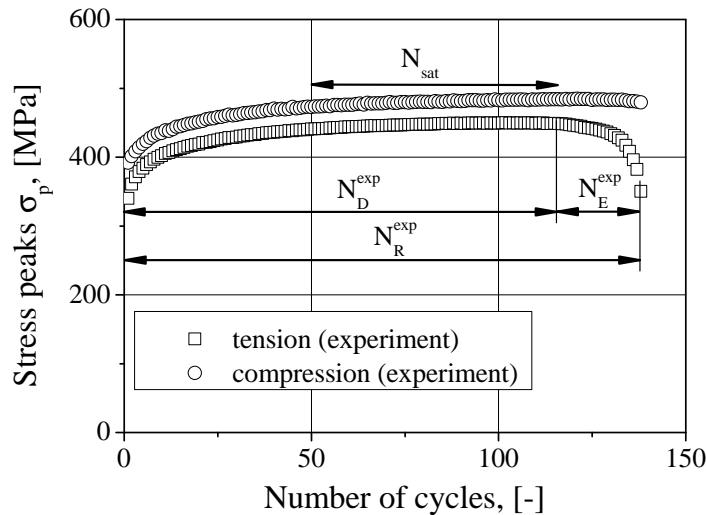
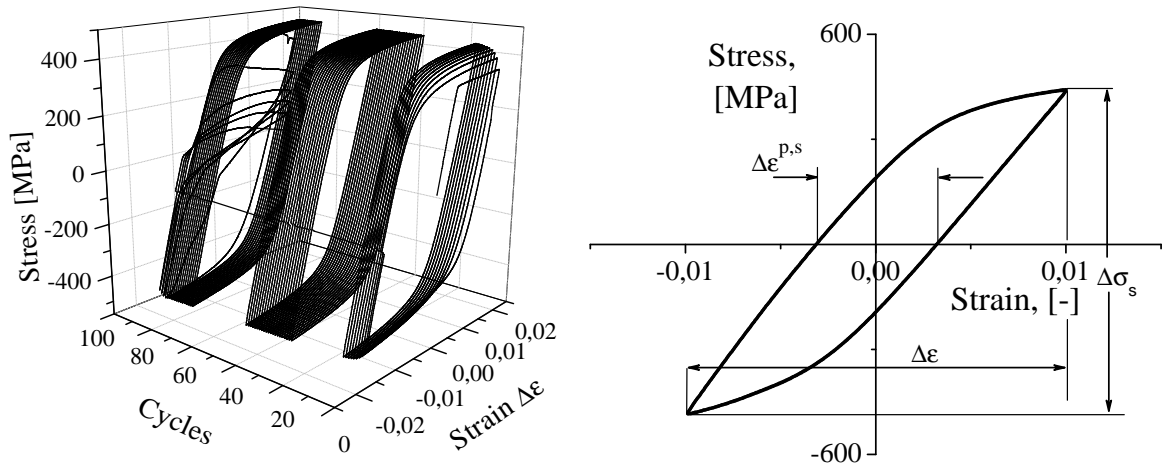


Figure 4.14: Peak stresses within the LCF experiments conducted on flat specimen (4 mm sheet)

The experimental results comply with the Coffin-Manson relation (Section 3.3.2 (pg. 12)) and the respective model parameters for the two directions are given in Table (4.6). Table (4.6) shows the interrelationships between the applied strain ranges and the corresponding fatigue lives. Analogously to the standard Coffin-Manson plot, the moment of damage initiation, measured by the number of cycles  $N_D$ , can be plotted in a similar manner. However, as will be explained, damage initiation is assumed to be governed by the accumulated plastic strain. Hence,  $N_D$  is plotted as a function of  $\Delta\varepsilon^P$ , see Figure 4.16.

Cyclic tension compression curves for a specimen with strain range 0.035 have been plotted in Figure 4.15(a). An important observation is that this alloy/structure exhibits a sudden loss of strength. In the monotonic tests upon reaching the ultimate stress (Figure 4.11), minute softening is observed before final rupture. Specimens under cyclic loading fail in a similar abrupt manner as well (Figure 4.14). Since in ductile materials, the softening phase is longer, the aforementioned observation is an indicator for the brittleness of the ma-



(a) cyclic tension-compression response (For sake of clarity, the cycles between 10-30 and 50-75 have been omitted.) (b) stabilised hysteresis (schematic)

Figure 4.15: Hysteresis produced by the flat specimen (4 mm sheet) subjected to loading with a strain range of 0.035 (with anti-buckling guides)

Table 4.6: Coffin-Manson parameters for Al2024-T351 flat specimen (4 mm sheet)

Orientation	$\dot{\epsilon}_f$	$c$	Strain range (%)	Cycles ( $N_R$ )
L	0.09838	-0.55	2.5-3.75	48-197
T	0.06421	-0.34127	2.375-4.5	21-145

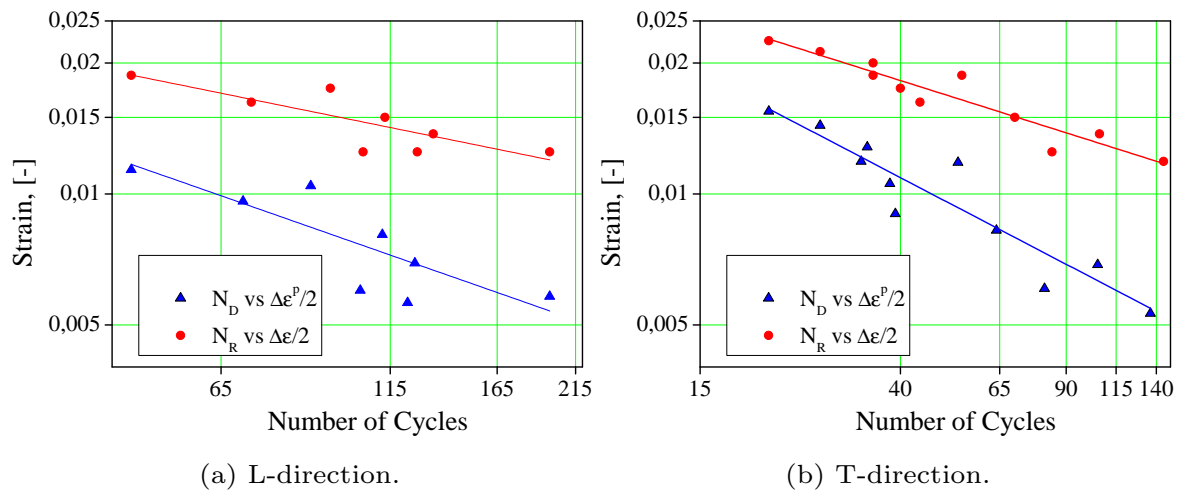


Figure 4.16: Coffin-Manson diagrams for the specimens (4 mm sheet) according to Figure 4.10 (model parameters according to Table (4.6))

Table 4.7: Experimental results for smooth flat specimens (4 mm sheet); for L and T-direction

Orientation	$\Delta\varepsilon$ [%]	$\Delta\varepsilon^P$ [%]	Number of cycles	
			$N_D^{\text{exp}}$	$N_R^{\text{exp}}$
L	3.75	2.275	48	52
	3.5	2.0875	68	74
	3.0	1.6125	108	116
	2.75	1.3875	125	135
T	3.25	1.8	39	44
	3.0	1.65	64	70
	2.5	1.2125	81	88
	2.375	1.0625	136	145

terial suggesting a rather quasi-brittle material response at the microscale. Selected results from the experimental testing are given in Table (4.7).

## 4.4 Microstructure

The mechanical anisotropy of metals is strongly related to the spatial distribution of grain orientations, grain shapes and sizes. After having analysed the macroscopical mechanical behaviour of the two different sources of material, it is now advisable to have a look at their respective microstructures, in order to understand the physical causes of the anisotropy seen in Section 4.3.1.1 and in Section 4.3.2.1. At the beginning of this section, the crystallographic grains are described and, afterwards, various types of inclusions in the matrix material (100 mm plate and 4 mm sheet) are examined.

Extensive research work has already been done on the microstructure of the 100 mm plate by Quan et al. (2004), where in particular the short-transversal (thickness) direction was the main focus of interest. During the course of this study the role of the microstructure is studied in more details and it is extended to the 4 mm sheet.

### 4.4.1 Grains

Whereas the orientations of grains can in principle be determined by texture measurements, their sizes and shapes become visible by polishing and etching plane cross sections of the material. For the aluminium alloy (both plate and



sheet) in the current investigation, a Barker's etch has been used to obtain an optimal contrast and visibility of grain boundaries.

#### 4.4.1.1 100 mm plate

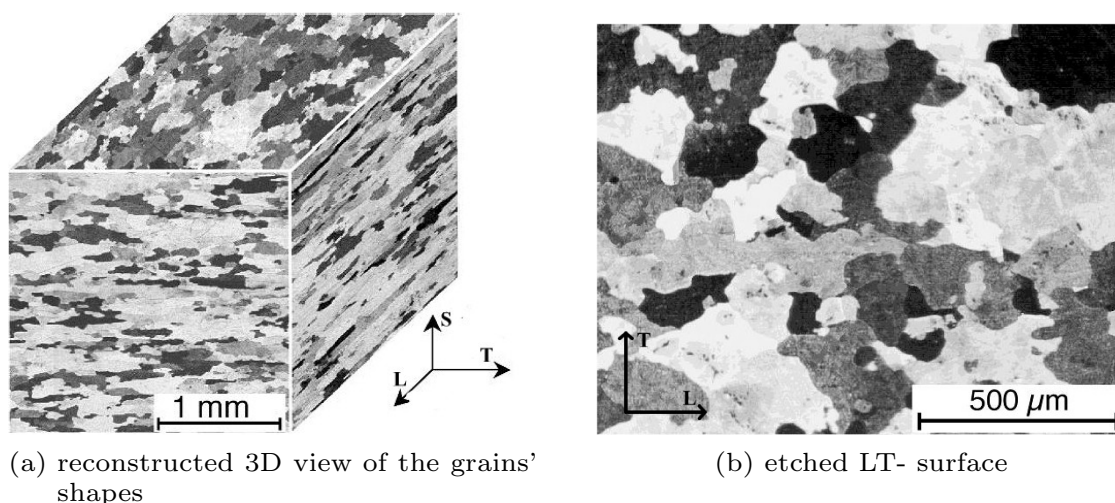


Figure 4.17: Etched microstructure of the 100 mm plate

In Figure 4.17(a), a reconstructed 3D crystallographic image for the 100 mm plate is shown. It is evident that the grains of the material have a flat shape, where the thickness in S-direction is much less than the width in L and T-direction.

Pictures have been acquired from three different surfaces using polarised light, having its normal vectors in L, T, and S-direction, respectively. Moreover the LT-plane section (Figure 4.17(b)) reveals two distinct grain sizes: small grains surrounded by much bigger ones. This structure is probably due to partial recrystallisation, that occurs mainly during and after hot-rolling, at a temperature of about 400 °C.

Table 4.8: Main diameter ratios of the grains in the 100 mm plate,  $D_X$  is the diameter along L, T, S-direction

$D_L/D_S$	$D_T/D_S$	$D_L/D_T$
$\sim 2.25$	2.09	1.08

Considering the ratios between the grain diameters measured in various directions (see Table (4.8)), it is seen that they can be approximated as slightly elliptical disks, with a thickness that is about half the width. These disks are averagely about  $120\ \mu\text{m}$  wide and  $52\ \mu\text{m}$  thick.

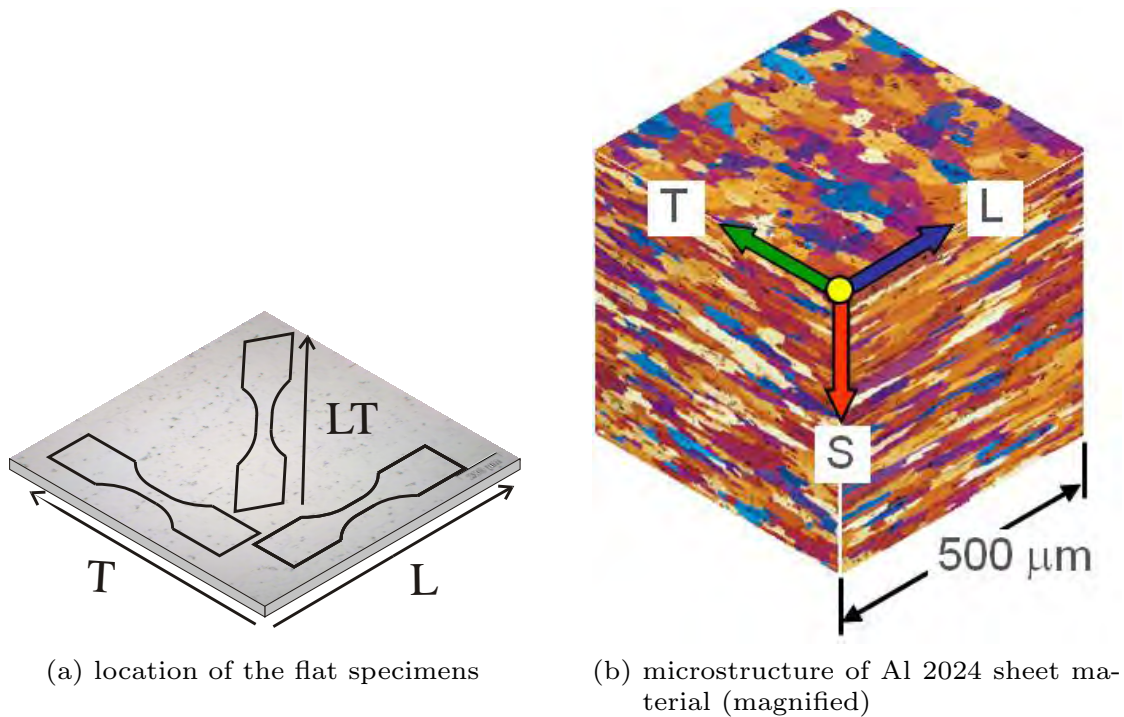


Figure 4.18: 4 mm sheet of Al2024-T351

#### 4.4.1.2 4 mm sheet

In case of 4 mm sheet, Figure 4.18(a) shows the location of the two main directions where the specimens have been taken and Figure 4.18(b) displays a representative volume element with grain structure, clearly showing the flat shape of the grains with the greatest principal axis in the LT-plane. The average grain sizes for the sheet in L- and T-directions are  $20\ \mu\text{m}$  and  $10\ \mu\text{m}$ , respectively. The grain dimensions in sheet thickness are reduced due to the rolling process and have an average length of  $5\ \mu\text{m}$ .

As loading is applied in the sheet plane, the mechanical properties are primarily influenced by the orientation of the grains, having roughly a size ratio of 2 between T and L-direction.

### 4.4.2 Particles

The presence of intermetallic particles, which act as nucleation sites for voids causing damage, significantly affects the damage tolerance of a material. These heterogeneous particles are distributed spatially in clusters through the length and thickness of the material.

Here, it should be noted that the considered volume (100 mm plate) allows to distinguish between particles of various sizes. For this reason, the 4 mm sheet will not be considered in what follows. However, it bears emphasis that conceptually, a similar classification of particles can also be applied to the sheet. Particles having consistent average size of 10 – 20  $\mu\text{m}$  were found randomly dispersed through the thickness of the sheet. These particles play a major role in damage initiation which will be discussed in Section 4.5.1.2, 4.5.2.2.

By analysing the material with the optical and electronic microscope, mainly three kinds of different particles are detected. These particles are classified with respect to their dimensions, different position and forming mechanisms. They are referred to as Particle Levels (PL), and are sorted from I to III, from the biggest to the smallest. The size and area fraction<sup>4</sup> data for these particles are exposed in Table (4.9).

Table 4.9: Main dimensions of the three levels of particles (100 mm plate) and their area density detected at the scanning electronic microscope (Quan et al., 2004)

	Arithmetic Mean Diameter	Area Fraction
Particle level I	$23.5 \pm 16.7 \mu\text{m}$	$3.2 \pm 0.7\%$
Particle level II	$1.03 \pm 0.76 \mu\text{m}$	$4.8 \pm 2.1\%$
Particle level III	Needle $\frac{\text{Length } 0.94 \pm 0.84 \mu\text{m}}{\text{Thickness } 0.13 \pm 0.09 \mu\text{m}}$	$2.3 \pm 1.2\%$
	Dot $0.24 \pm 0.19 \mu\text{m}$	

Now, the three levels of particles will be described and classified, starting from the smallest ones.

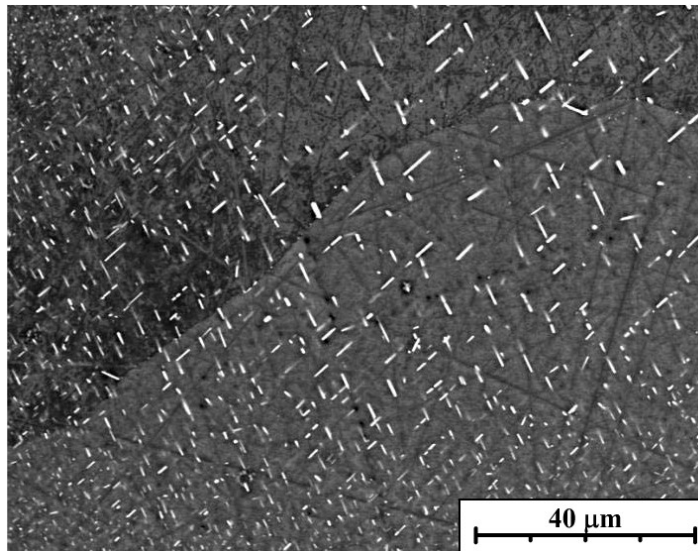


Figure 4.19: Particles of PL III (100 mm plate), see Table (4.9)

#### 4.4.2.1 Particle level III

Particle level III is identified as the common intermetallic precipitate, formed during ageing. Its chemical composition is mainly that of the two phases present in Al-Cu and Al-Cu-Mg alloys, i.e. the  $\theta'$  phase  $\text{Al}_2\text{Cu}$  and the  $S'$  phase  $\text{Al}_2\text{CuMg}$  (the latter being predominant). Both of them are coherent with the matrix, and therefore contribute to the hardening and the improvement of the mechanical properties of the material. They work as an obstacle to dislocation movements.

From Figure 4.19, it is seen that the precipitates appear mainly dot- and needle-shaped. Needle-like precipitates show a more elongated shape and seem to have preferential directions inside crystal domains. Since the crystallographic domains are statistically distributed with different orientations from grain to grain, the effect of these particles is orientation-independent with respect to the overall macroscopic mechanical behaviour. Dot-like precipitates have probably a needle shape as well but were cut with a plane normal to the direction of their length. In the upper right hand side of Figure 4.19, a great increase in the precipitates size can be seen. This happens mainly because of the presence of a small angle grain boundary (dark line), as explained in the following section.

---

<sup>4</sup>While the area fraction for PL I is based on the whole specimen only local area fractions can be given for PL II, since the respective fraction varies significantly.

#### 4.4.2.2 Particle Level II

The precipitation process is not uniform during ageing and it is favoured at preferred sites due to discontinuities or imperfections in the material. One of these sites is classically the grain boundary, where the interface formed by the different crystal orientations helps reducing the surface energy necessary to begin the nucleation of the precipitates. In this region, the precipitates had more time to grow resulting in the formation of bigger particles. These bigger precipitates belong to Particle level II (see Table (4.9)) and they are about twice as big as those corresponding to Particle level III.

Since most of the alloying elements are attracted into the bigger precipitates, the region surrounding them is free of small precipitates: such regions will be called PFZs (Precipitate Free Zones). Evidently, the PFZs are weaker than the rest of the matrix.

#### 4.4.2.3 Particle Level I

From the data in Table (4.9) it can be seen that this level of particles is in average more than twenty times larger than the particles of level II. While the chemical composition is very similar to that of the precipitates<sup>5</sup>, their shape now appears to be a round asymmetric ellipsoid, with the axis oriented along the L-direction. The ratio between the longest diameter of the particles and the shortest (aspect ratio of the particles) is  $1.6 \pm 0.6$ . Consequently, they are not so far from spheres. A mean value of these particles around 25  $\mu\text{m}$  is observed with a great scatter (Paganelli, 2005). Particles with a diameter of 40  $\mu\text{m}$  were found with half the frequency of the 25  $\mu\text{m}$  ones, while particles up to 80  $\mu\text{m}$  were also detected. Such a wide scatter could not be observed for particles related to the previous two levels. In addition to this, the alloying elements are concentrated in certain regions leaving impoverished small stripes behind in which the concentration of strengthening precipitates is strongly reduced. These stripes are named PFBs (Particle Free Bands). Analogously to the PFZs, they are weak bands inside the material. However, the weakness is even more pronounced. Qualitatively different to the PFZs, those zones are not always located at the grain boundaries, but they form a sort of network that seems to be independent of the position of the grains. In Figure 4.20, two different planes are observed in the optical microscope. As is evident from Figure 4.20(a) for the LT-plane, those networks lead to isolated

---

<sup>5</sup>The chemical composition, proved by EDX, showed that those particles are mainly composed by the intermetallic compound  $\text{Al}_2\text{CuMg}$ , with a small percentage of  $\text{Al}_2\text{Cu}$ . In addition, some other compounds were also found. Those are mainly due to Mn and other impurities, such as  $(\text{Fe},\text{Mn})\text{Al}_3$ ,  $\text{Cu}_2\text{Mn}_3\text{Al}_{20}$  and  $\text{SiO}_2$  in some darker spots. See Quan (2001) for more details.

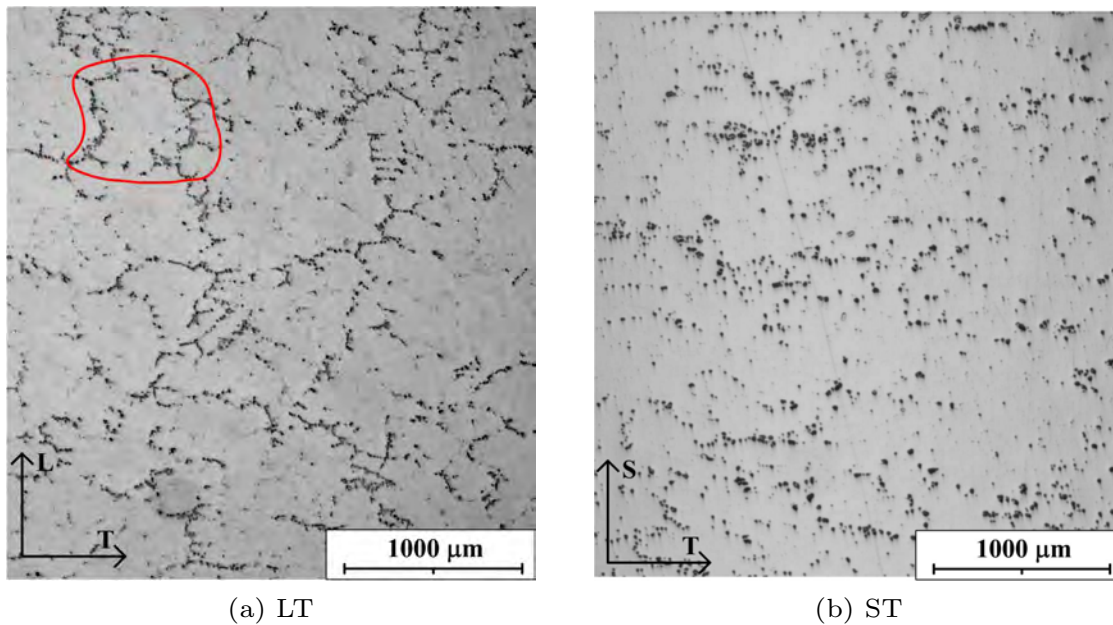


Figure 4.20: Network of Particle level I in two different planes of a 100 mm plate

but well-defined domains of particles, which will be called from now on PFB domains.

However, even though such impoverished bands can be seen also on the ST-plane (Figure 4.20(b)), which are aligned in T-direction, no clear network-like structure can be detected. The aforementioned network is much finer than in the LT-plane, and the electron microscope is necessary to visualise the PFBs and the distance between them. In Figure 4.21(a), a SEM micrograph of a ST-plane is shown where the PFB can be clearly identified. The average thickness of the PFBs, measured in many of such micrographs, was found to be of 5  $\mu\text{m}$ .

The traces of the PFBs are shown in Figure 4.21(b). Here, the network-like structure is clearly visible. It is also existent on the ST-plane albeit much thinner in S-direction. Now, combining the data obtained by the LT and ST-views, it can be stated that these domains are roughly disk-shaped, even though no clear connection with the grain structure can be observed. These disks have averagely a diameter of 360  $\mu\text{m}$  and a thickness of 25  $\mu\text{m}$  (Quan et al., 2004).

It was also observed that the particles (I, II, III) are bigger away from the surface of the plate. This variation which is due to the manufacturing process and can be observed in Figure 4.22. Furthermore, some particles of PL I were found already broken before any loading has been imposed on the material. This will be analysed in details by synchrotron tomography (see Section 4.6).

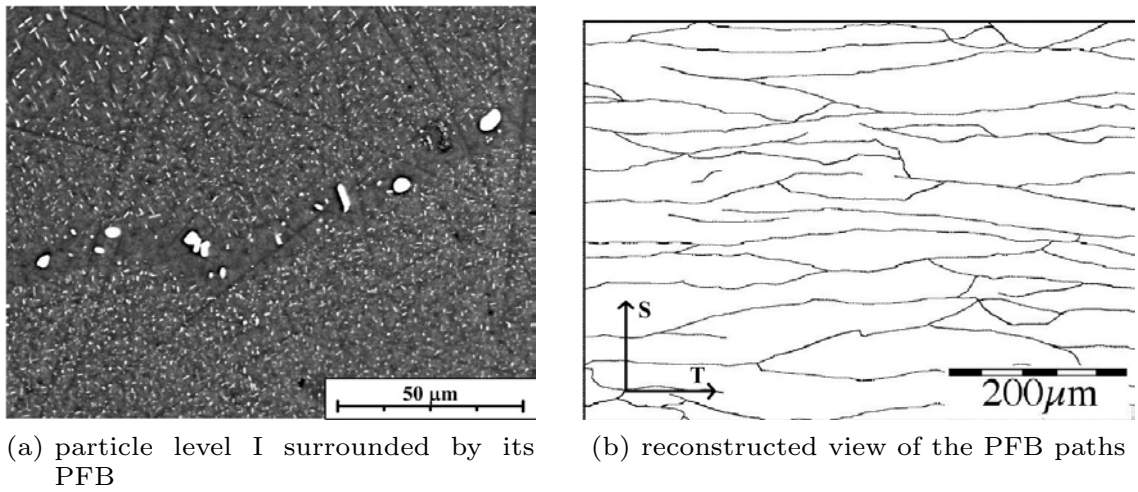


Figure 4.21: Particle Level I and PFB (Quan et al., 2004) detected at a 100 mm plate

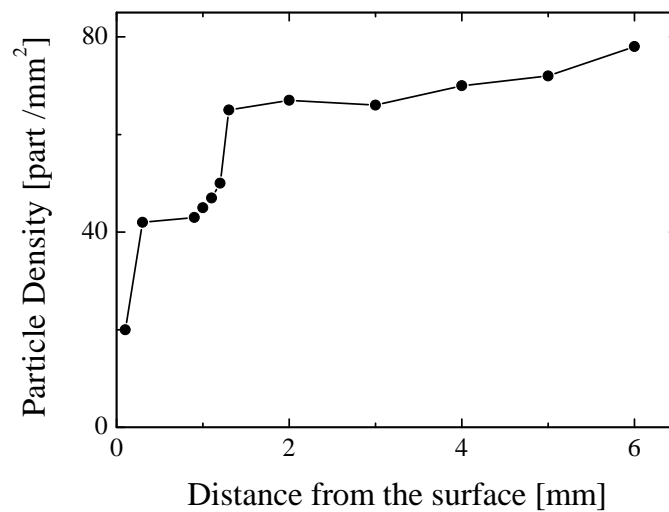


Figure 4.22: Density of Particle level I vs distance from the surface of the 100 mm plate

## 4.5 Fracture mechanisms

Having discussed about heterogeneous particles focus is next on the fracture behaviour of the considered alloy. The visualisation and analysis of the fracture surface is a classical way to understand the fracture process. In literature, different types of fracture are classified e.g. cyclically damaged surfaces show typically striation lines, whereas monotonic loading results in either a dimple or a staircase fracture profile. This depends on the material and the geometry considered. For further analyses, we divide the possible microscopical mechanisms into brittle and ductile, and each of them into various subcategories.

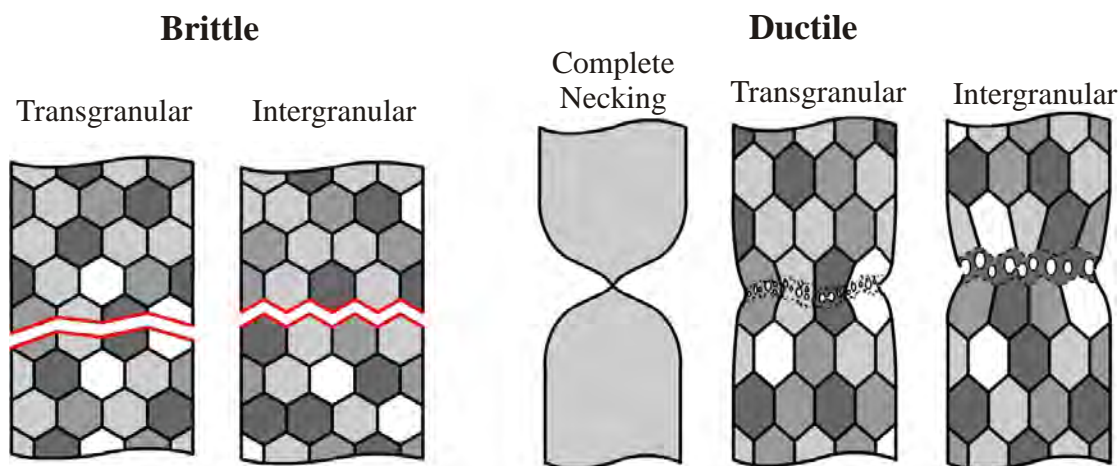


Figure 4.23: Possible fracture mechanisms at room temperature under static loading

Concerning brittle fracture the following mechanisms can be observed:

- **Transgranular:** This kind of fracture is caused by the detachment of well defined planes inside the crystal lattice. Typically, a sharp and polished fracture surface is produced (cleavage).
- **Intergranular:** It occurs by decohesion of grain boundaries, that are intrinsically weak interfaces.

On the other hand, ductile fracture is mainly caused by plastic deformation mechanisms, and it appears quite jagged and unglazed. The main mechanisms that produce this fracture are:

- **Complete necking:** It is caused by the complete collapse of the structure and it is purely due to plastic flow (Figure 4.23).



- **Transgranular:** The fracture is often caused by voids that are generated and grow inside the material, making it fail faster than in the previous case. If it happens inside the grains, the fracture is named transgranular.
- **Intergranular:** As seen in Section 4.4, grain boundaries are a place where bigger particles are more likely to be found. If these particles break or detach from the matrix, voids are generated inside the material. Therefore, the mechanism described before takes place more likely on the grain boundaries if particles such as PL II are found on the grain boundaries.

Vital to any fracture mechanism is the understanding of crack initiation during fatigue loading. Crack initiation usually occurs at the specimen's surface (see, e.g., (Lukas, 1996)), and is generally caused by stress concentrations, giving rise to local plastic deformation or cracking and detachment of brittle precipitates. Local stress-strain concentrations can be attributed to a variety of microstructural inhomogeneities (see, e.g., Lindley (1986)).

For understanding initiation of a macroscopic crack, it is important to understand the evolution of microcracks (damage evolution). Damage in Al-alloys usually nucleates at large and brittle intermetallic particles or coarse precipitates, and sometimes also at smaller particles such as dispersoids or precipitates, cf. Lassance et al. (2007); Garrett & Knott (1978); Pardoën & Pineau (2007).

### 4.5.1 100 mm plate

Optical microscopy (OM), scanning electron microscopy (SEM) and X-ray micro-tomography (SR $\mu$ CT) have been used at HZG to obtain quantitative information about micro-structural characteristics (Quan et al., 2004). For fracture and damage, the analysis of big intermetallic particles (equivalent diameter  $23.5 \pm 16.7 \mu\text{m}$ ) aligned in a network-like structure (clusters or Precipitate Free Bands (PFB)) which separate the matrix into domains is of utmost importance (Section 4.4.2.3). The majority of them are  $\text{Al}_2\text{CuMg}$  particles appearing in SEM pictures (BSD mode) in Figure 4.24(a) and (b) in white colour. This micro-structure results in higher damage rates in the PFB, if the material is loaded in S-direction. During evolving damage, the most probable orientation of the microscopic crack is perpendicular to the loading direction with “shearing jumps” between parallel PFBs, cf. Steglich et al. (2008). To systematically characterise fatigue fracture, fracture surfaces corresponding to monotonic loading are compared to their cyclic counterparts. 2D and 3D snapshots of the micro-structure have been extracted.

#### 4.5.1.1 Uniaxial tension tests

For monotonous loading, the fracture surface shows a dense dimple structure, which is characteristic of ductile failure, cf. Figure 4.26(a). However, the picture provides only two-dimensional information (the depth is missing). Some more details concerning depth-related information will be given in the subsequent paragraphs. Some multiple cracks are found at the surface of the notch. Various multiple broken particles appear just under the fractured surface in the middle of the specimen (Figure 4.24(a)). This is not the case in the region close to the notch root (Figure 4.24(b)), where slight necking is observed. Hence, the crack starts in the middle of the specimen and propagates to the surface. The specimens in Figure 4.24(a),(b) have been cut and polished in the longitudinal direction.

Imaging software (Alicona) combined with SEM was used to study and evaluate the shape and profile of the fracture surfaces. A JEOL JSM-6460LV SEM, operated at an accelerating voltage 20 kV was used for the analysis. Stereogram analysis were carried out with 3D image construction obtained using the aforementioned software. Figure 4.25 shows stereogram 3D images re-constructed from 3 SEM (Scanning electron microscope) images, respectively. The stereogram was obtained by tilting the specimen  $\pm 5^\circ$  from the top. In Figure 4.25, it can be seen that the fracture (monotonous loading in S-direction) initiates at different height levels, creating an uneven structure. This kind of ductile damage occurs at various stages within the material's layers. The scattered micro-cracks coalesce and form eventually a macro-crack, with bright planes representing the shearing ductile fracture. Accordingly, so-called shear lips (smoothened dimples due to shear deformation) are observable (instead of dimple structures).

#### 4.5.1.2 Cyclic tests

In cyclic loading large single “craters” (due to particle embedding) appear close to or directly at the edge of the fracture surface, see Figure 4.26(b). This is a strong indicator for failure originating from the surface. Fatigue lines are highly visible around the single “craters”.

By way of contrast to the monotonic case, the mechanisms change to mix-mode failure in the LCF regime for the S-direction (Figure 4.25). Consequently, uneven ductile failure areas, fatigue lines and shear lips are visible. Failure starts within a cluster of particles. Subsequently, with increasing accumulation of plastic strain, dense simple structures appear. Finally, the distributed damaged zones connect to each other due to ductile crack propagation and coalescence (fatigue lines). However, shearing ductile fracture as observed for

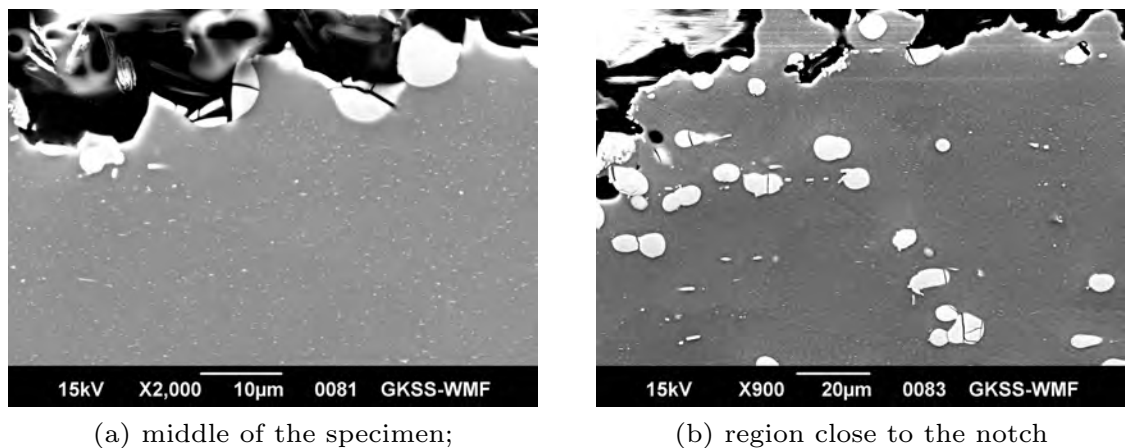


Figure 4.24: SEM image of longitudinal micro-sections close to the fracture surface of the monotonically loaded RNB (Figure 4.4(a)) specimen (100 mm plate, S-direction)

monotonic loading, can be seen as well.

## 4.5.2 4 mm sheet

After the LCF failure of the 4 mm thick specimens, the fracture surface morphology was examined with a scanning electron microscope with the specification as described in Section 4.5.1.1. The visualisations were made at different magnifications to identify the unique fractographic features, showing the immediate vicinity of crack initiation site and discriminating the regions of stable and unstable crack extension.

### 4.5.2.1 Uniaxial tension tests

For the considered flat specimens of Al2024 under monotonic loading, shear rupture occurs. A dominant macrocrack propagates with relatively low necking through the specimen's thickness. The profile of the fracture surface is of so-called slant-shear fracture-type (across the thickness). This kind of failure is typical for thin sheets and small-diameter rods, cf. Besson et al. (2003). The term slant-shear fracture is somewhat misleading, because the angle between the principle axis and the fracture surface was measured on average to be  $38^\circ$ .

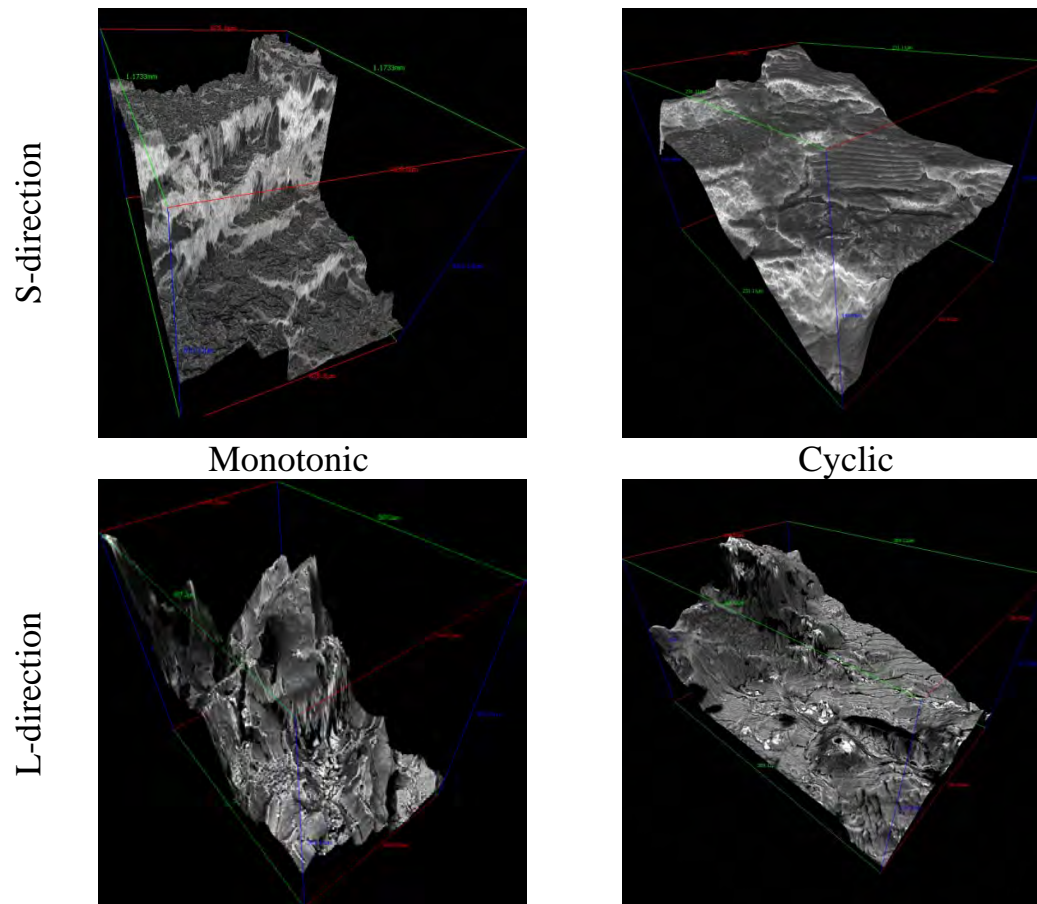


Figure 4.25: Fractured surface profiles of Al2024-T351 RNB specimen in L and -direction of the 100 mm plate (SEM data, visualised using 3D image re-construction software, Mex (Alicona, Inc.) (Mex-Alicona<sup>®</sup>, 2010))

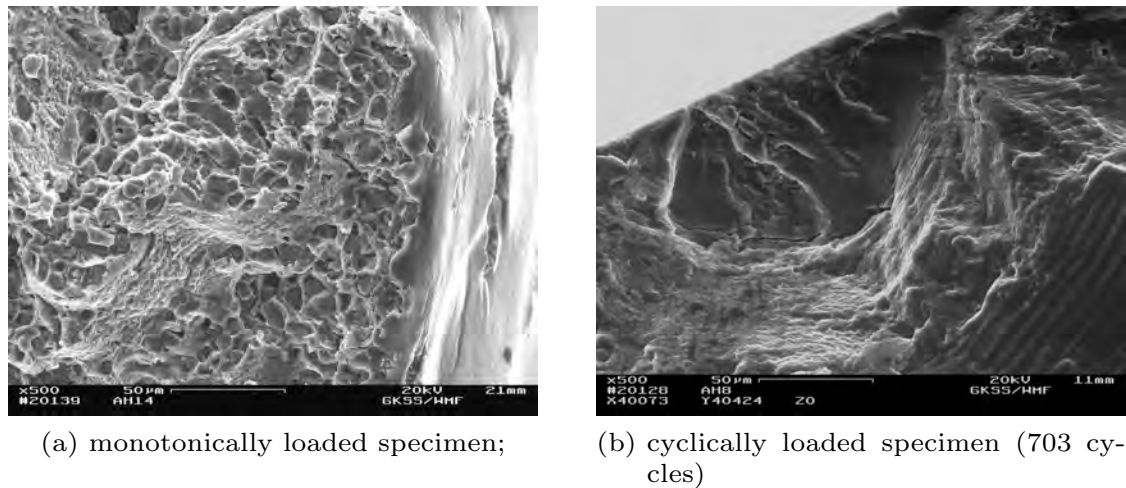


Figure 4.26: SEM obtained image of fracture surfaces in RNB specimens (100 mm plate, see Figure 4.4(a)) close to the notch root

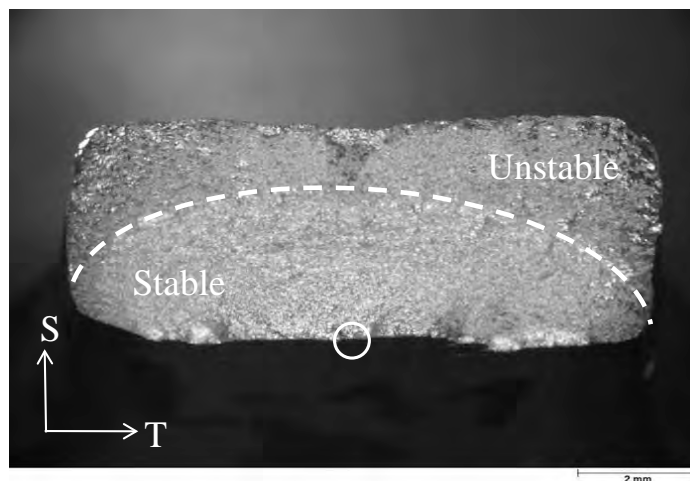


Figure 4.27: A 60° axial view of the fracture surface; failure after 135 cycles in L-direction (4 mm sheet),  $\Delta\epsilon=0.0275$ . The lower small circle indicates the crack initiation site

### 4.5.2.2 Cyclic tests

Typically, fatigue fracture surfaces of Aluminium alloy Al2024 have a chaotic wavy appearance (Khan et al., 2010). Furthermore, the fracture surface is composed of relatively shiny smooth areas with periodic markings called tire tracks, because they often resemble the tracks left by a tire. For the sake of clarity, the fracture surface is divided into two disparate regions: Those produced by stable and unstable crack growth (Figure 4.27). The elliptical front separating such regions grows from the surface across the specimen's thickness. The damage initiation point (discussed in detail in a later section) is close to the centre of the ellipse.

A 3D rendering of the images obtained from the SEM shows the damage (or crack) initiation point (Figure 4.28). The stable crack growth region has a dimple structure with large cavities, characteristic of ductile damage in aluminium alloys. The stable crack grows nearly perpendicular to the loading direction and produces a flat profile. The unstable region has a dimple structure with smaller cavities (Figure 4.29(a)) which are formed during unloading/compression. Fatigue lines can be observed only in the stable crack growth region (Figure 4.29(b)) with small flat patches, also produced in the compression phase. The related unstable crack growth region is slanted like that one observed in monotonic loading. The sizes of the unstable and stable crack growth regions vary with loading conditions. For a very high amplitude, restricting the lifetime to a few cycles, the stable crack growth region is smaller as compared to a lower amplitude with more number of cycles. There is no observed connection between stable/unstable crack growth regions and trans/intergranular crack propagation. Failure occurs always in a mixed-mode without any generalised trend.

Material inhomogeneities are common fatigue crack nucleation sites in aluminium alloys, cf. (Tanaka, 1982; Bowles & Schijve, 1973). Inhomogeneities include constituent particles and micropores as intrinsic properties as well as surface features like scratches. In thin sheet aluminium 2024-T351, the rolling of the material has eliminated any microporosity and in the absence of surface scratches, fatigue cracks initiate at constituent particles. Constituent particles generally range in size from 1-40  $\mu\text{m}$  (pg. 35) and contribute to the strength of the alloy. During high strain processing of thick plates into sheet material, many of these particles break and the larger ones are broken into clusters of smaller particles. If the material is subjected to cyclic fatigue loading, cracks emanating from the constituent particles grow into the surrounding aluminium matrix and continue to propagate.

The nucleation of fatigue cracks represents an important stage in the damage evolution process in cyclically loaded materials. In homogeneous materials

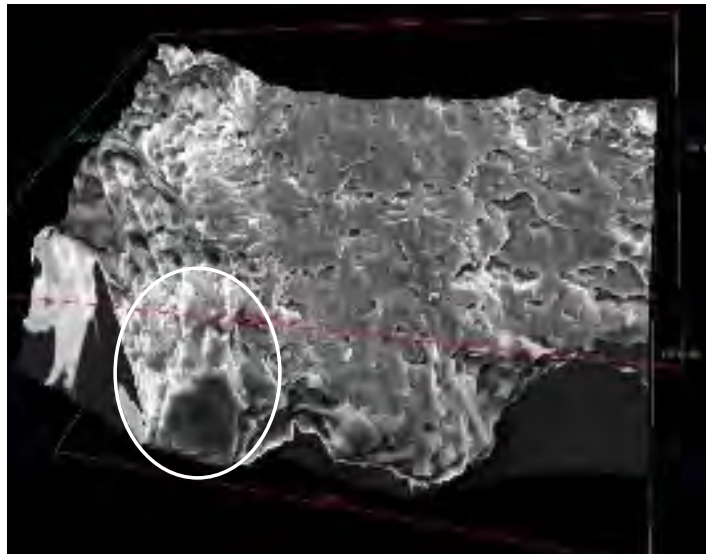
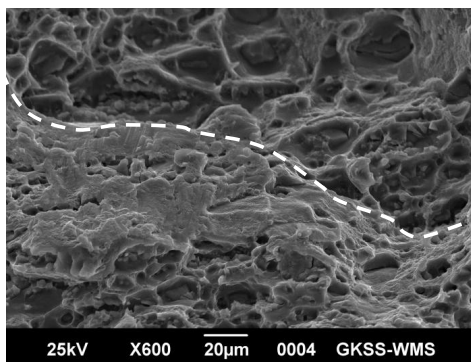
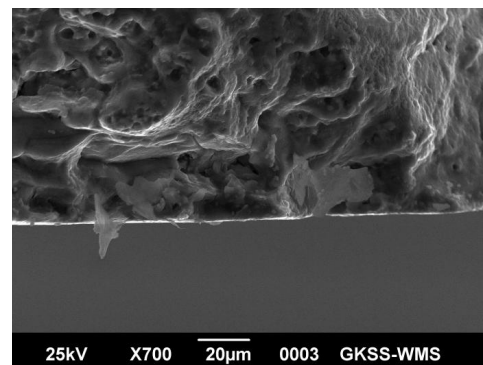


Figure 4.28: 3D rendered micro-structure of the fracture surface; the left lower circle indicates the crack initiation site; failure after 135 cycles in L-direction (4 mm sheet),  $\Delta\varepsilon=0.0275$



(a) transition path dividing stable (below) and unstable (above) crack growth regions, shown in white



(b) appearance of fatigue lines near crack initiation site

Figure 4.29: Damage mechanisms in a 4 mm sheet (failure after 135 cycles in L-direction,  $\Delta\varepsilon=0.0275$ )

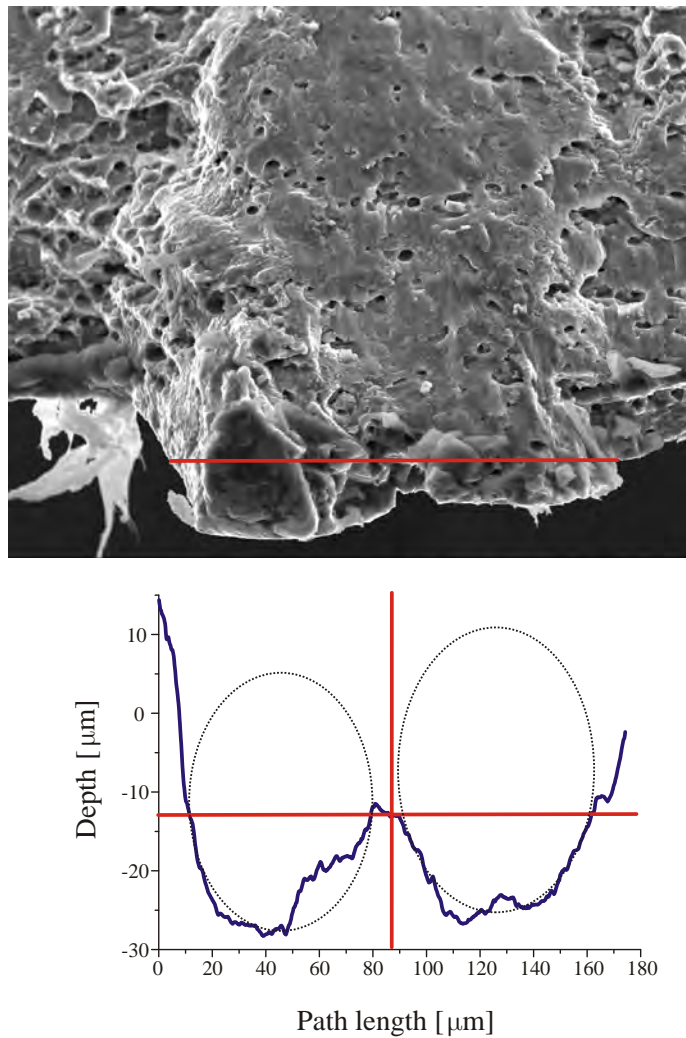


Figure 4.30: (above) SEM fractograph of the failure surface after 135 cycles in L-direction (4 mm sheet),  $\Delta\varepsilon=0.0275$ . The line defines the analysed path; (below) profile analysis associated with the above path showing two big cavities at the surface



without appreciable macroscopic defects, the surface of the material plays a prominent role in fatigue crack nucleation. As a matter of fact, the majority of fatigue cracks initiate at the surface, cf. Man et al. (2003). If macroscopic and microscopic defects (e.g. inclusions, holes and non-coherent precipitates) are present, the interface between the defects and the matrix is a potential site of crack nucleation.

Figure 4.30a shows the profile analysis of a fracture surface. Large cavities were found at the surface of the broken specimen and a cavity produced by a particle-up-rooting was found close to the initiation site of the fatigue crack. Area analysis (see Figure 4.30b) revealed that the particle sizing is on average 10-20  $\mu\text{m}$  near the surface. As expected, the lifetime is roughly inversely proportional to particle sizing. This implies, the bigger the particle, the sooner damage initiates and the less resistant the material.

## 4.6 Damage visualisation using synchrotron micro-tomography

Evidently, a complete understanding of the fracture mechanisms described in the earlier sections require particularly a careful analysis of damage evolution at the micro-scale. Consequently, non-destructive microstructural techniques such as Synchrotron radiation based X-ray micro-tomography (SR $\mu$ CT) have been applied. It has emerged during the last decade as a new powerful direct technique to visualise the interior of an opaque sample at the microscale, cf. (Morgeneyer et al., 2008; Proudhon et al., 2007). The subsequent argumentation explains the choice of SR $\mu$ CT:

- The physical phenomenon ranges between different scales, e.g. microscale (particles) and nano-scale (damage). Thus, techniques like transmission electron microscopy (TEM) or focused ion beam (FIB) destructive tomography are too fine and metallographic destructive methods or even more sophisticated methods like neutron tomography are too coarse.
- The heterogeneous microstructure and the limited number of experiments require special non-destructive techniques like tomography to visualise the damage.
- SR $\mu$ CT data allow analysing damage effects (defects, interfaces such as cracks, etc.) combined with the microstructural properties (matrix and inclusions) and their interaction.
- SR $\mu$ CT possesses higher resolution compared to alternative X-Ray tomography (e.g.  $\mu$ -focus tube) (Bernhardt et al., 2004) and high density resolution, too. Furthermore, it provides the necessary monochromatic beam intensity to apply  $\mu$ CT on high absorbing samples without beam-

hardening artifacts.

- 3D method: can locate and quantify characteristics (damage, microstructure) inside structural components.

Although synchrotron micro-tomography shows a lot of advantages, the method is not without problems. More explicitly, tomographic images often contain different kinds of artifacts. The so-called *ring artifacts* are very common (formation of concentric rings in the images around the center of rotation of the tomographic set-up, see Figure 4.42). They are caused by differences in the individual pixel response of the detector or by impurities on the scintillator crystals. A way to reduce such artifacts is the shape and size filtering during the post-processing of the images. In summary, most problems associated with synchrotron micro-tomography can be taken into account by experienced researchers and thus, such problems are not serious.

SR $\mu$ CT has been applied to 3D measurements and in-situ observations of fatigue crack propagation (Müller et al., 2006). The used beamline HARWI II operated by Helmholtz-Zentrum Geesthacht at the storage ring DORIS III of Deutsches Elektronen-Synchrotron (DESY), Hamburg, Germany, enables SR $\mu$ CT with a high spatial resolution down to less than 1  $\mu$ m (Beckmann et al., 2006).

Within this investigation, small round notched bars with different radii taken from 100 mm thick sheet are being examined. The specimens have been extracted from the short-transverse direction (Figure 4.1). Initially, the material specification is described. Subsequently, a microstructural characterisation is given. Finally, the experimental and tomography set-up is briefly discussed. The section is concluded by a discussion and some concluding remarks.

#### 4.6.1 Micro-structural characterisation using SR $\mu$ CT

In earlier sections (see Section 4.4), the microstructure of Al2024 has been studied extensively using destructive methods. SR $\mu$ CT have already been used to visualise the micro-structure of Al2024. Figure 4.31(a) shows a reconstructed view of the investigated volume, cf. (Steglich et al., 2008). The particle clusters appear white, while the surrounding matrix is grey. The particles are aligned in a network-like structure (clusters) which separates the matrix into domains. These domains have “pancake” shape, with the S-direction (thickness direction) as the shortest axis and almost identical dimensions in L and T-directions, see Figure 4.31(b).

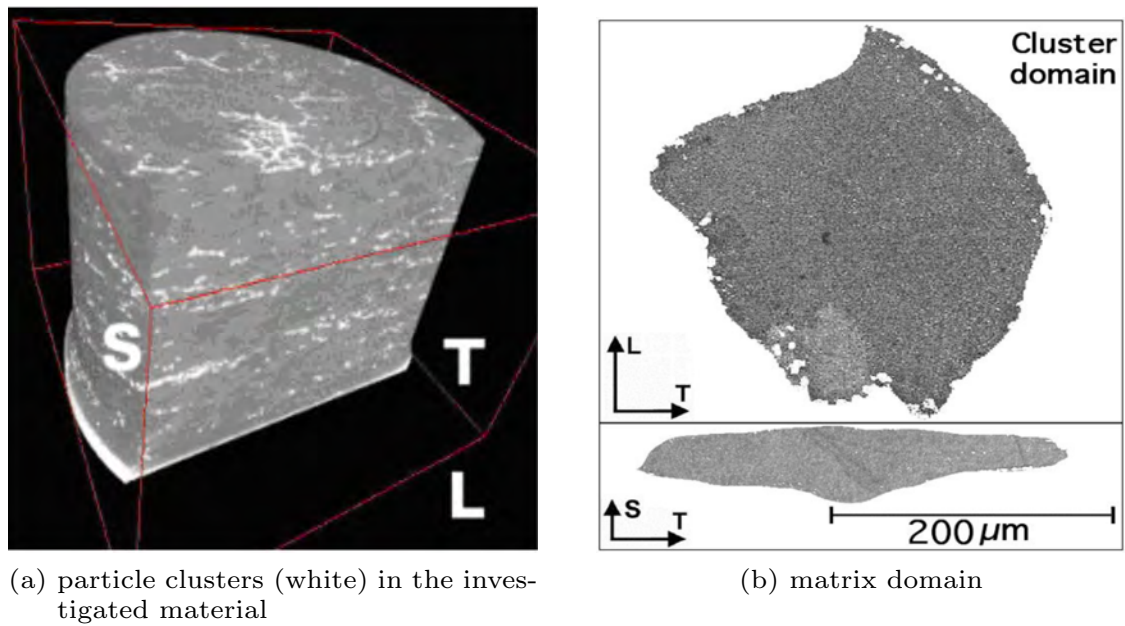


Figure 4.31: SR $\mu$ CT analysis on a 100 mm thick Al2024 plate (virgin state; see, Steglich et al. (2008))

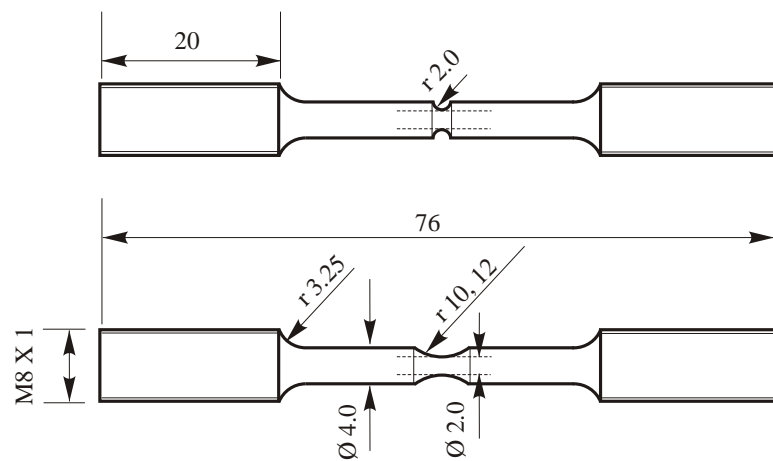


Figure 4.32: The geometry of the modified specimens (100 mm plate) used for SR $\mu$ CT investigations

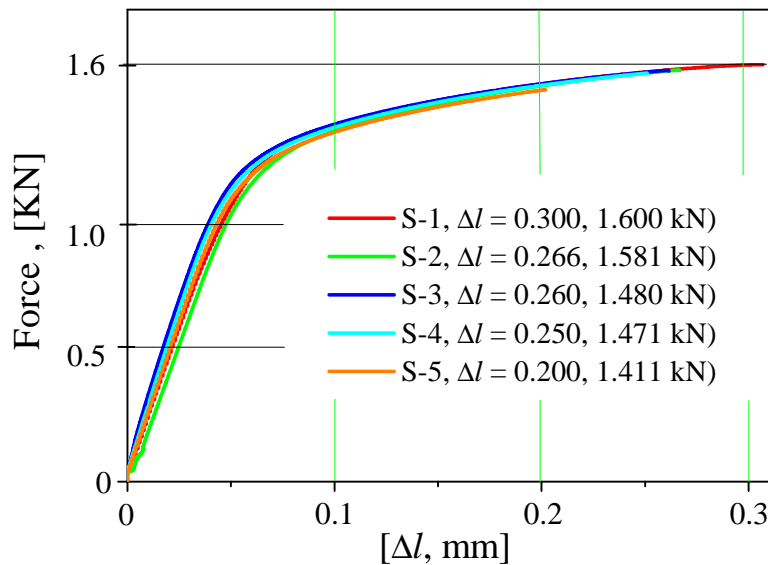


Figure 4.33: Uniaxial tests done on specimens having a 10 mm notch (gauge length  $l_0=10$  mm) extracted from a 100 mm plate

## 4.6.2 Experimental procedures

Round notched bar (relatively smaller than the ones used before Section 4.3.1.2) specimens having 2, 10 and 12 mm (hourglass) radius were manufactured (S-direction) from the 100 mm thick plate (Figure 4.32). To avoid the influence of surface roughness on the nucleation of cracks, the specimens have been polished mechanically before testing. Both tests (monotonic and cyclic) were performed displacement controlled. Figure 4.33 shows the incremental test procedure done to guarantee a damaged state during monotonic loading. The testing parameters for cyclic loadings remain confined to loading amplitudes identical to the ones discussed in Section 4.3.1.3. A typical measured load-elongation graph is given in Figure 4.34(a). These particular tests were stopped with the progression of the maximum load (Figure 4.34(b)). The minimal cross-section of the specimens was reduced up to 2 mm (Figure 4.32) to achieve better absorption resolution and the geometry was modified to localise damage in the middle part of the specimens.

Determining the onset of damage initiation and the further evolution of damage is the main purpose of this work. Specimens of both geometries have been tested till the marker stages (Figure 4.34(b)) classified as:

- A. This stage serves as a reference. It was reported in earlier works that rup-

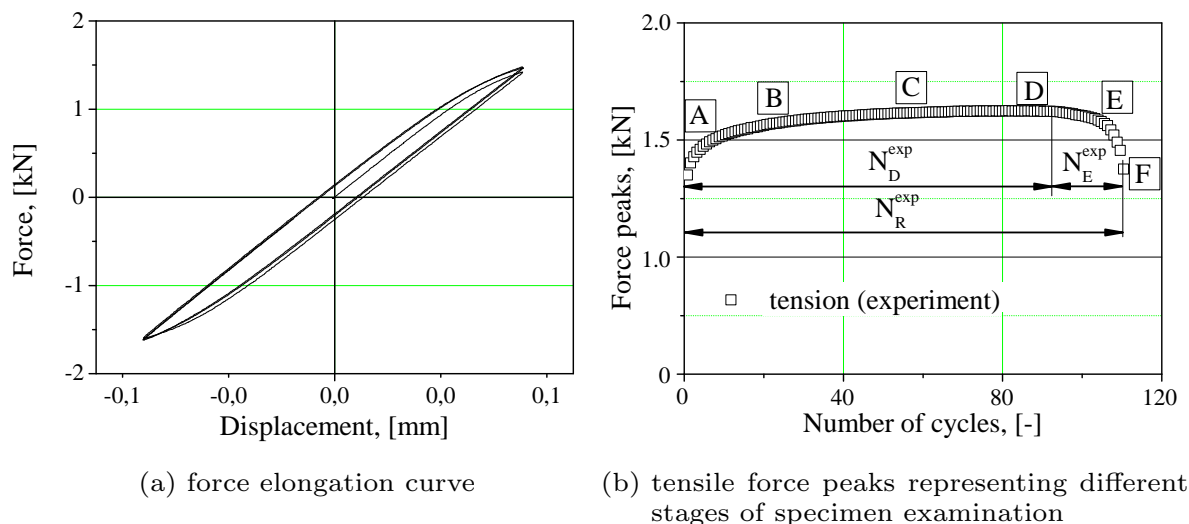


Figure 4.34: Cyclic mechanical response of small specimen (see before) of Al2024-T351 extracted from the S-direction of the 100 mm plate (see Figure 4.32)

ture of the brittle particles takes already place during this stage (Khan et al., 2010).

- B. During this stage, the specimen hardens and significant plasticity can be observed.
- C. A state of saturation is achieved, the stress remains almost constant. This stage represents the major portion of the specimen's fatigue life. Damage on the microscale already initiates during this stage.
- D. This point indicates the onset of the decrease in force. It corresponds to micro-cracks propagating into meso-cracks. The meso-crack initiation loci are vital in lifetime assessment.
- E. Various meso-cracks merge and constitute a large fatal propagating macro-crack.
- F. Final failure.

In the present thesis, the classifications of the different aforementioned stages are verified by synchrotron micro tomography. Clearly, in-situ measurements are possible in principle. However, overweight of the machine and vibrations involved could possibly distort the results (discussed in Section 4.6.5). For this reason, a staggered approach has been used.

### 4.6.3 Tomography set-up

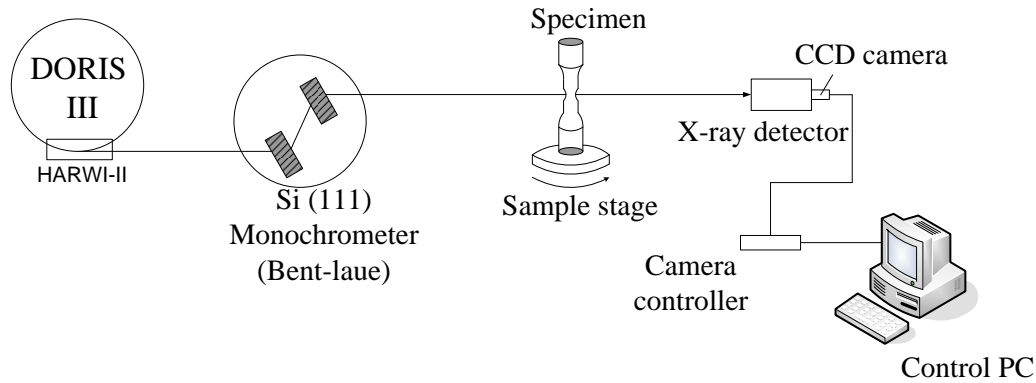


Figure 4.35: Schematic illustration of the synchrotron micro-tomography measurement system

X-ray imaging was carried out at HARWI-II beamline operated by HZG at the storage ring DORIS III of DESY, the largest synchrotron radiation facility in Germany. The schematic illustration of the measurement is shown in Figure 4.35. The samples were set approximately 40 m from the x-ray source. The zooming tube with the fluorescent screen and a cooled CCD camera were employed as a detector. As discussed formerly (pg. 52), the thickness of the specimen was adjusted according to the permeability of the radiation (Beckmann et al., 2006). The following beamline parameters were chosen for all scans:

Table 4.10: Parameters of SR $\mu$ CT at beamline HARWI-II

	HARWI II
Photon energy	25-30 keV
Pixelsize in projection	2.21 $\mu\text{m}$
Measured spatial resolution in projection	3.42 $\mu\text{m}$
Voxelsize in reconstruction	4.42 $\mu\text{m}$
Reconstructed volume	6.76 mm x 6.76 mm x 4.87 mm

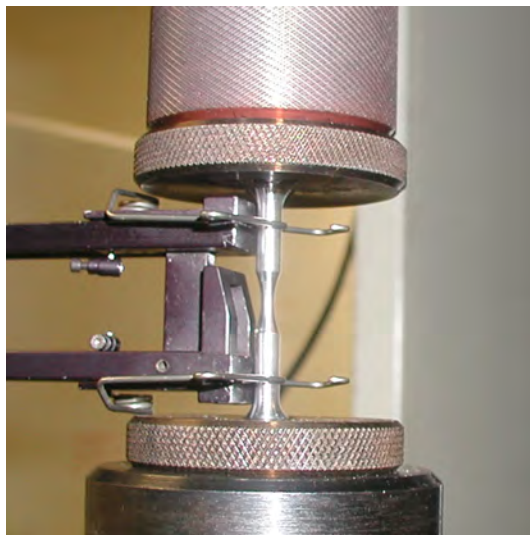
Based on the penetration depth, the energy of the incident beam was chosen to be 25 keV, and the micro-tomography images of the sample were observed. A CCD detector was located 40 m behind the specimen. For 3D reconstruction, a set of 900 radiographs of the sample was recorded over  $180^\circ$  rotations, where each rotation was  $0.2^\circ$ . The size of the voxels in the reconstructed images

Table 4.11: Components used for SR $\mu$ CT

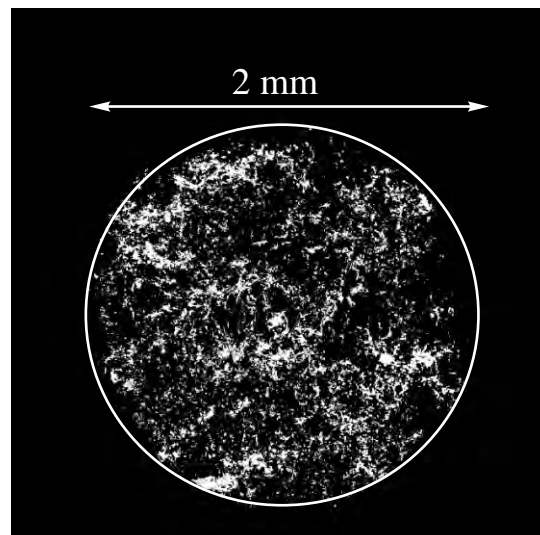
CCD camera	Finger Lake Instruments PLO9000, 3056 x 3056 pixels, pixel size: 12 $\mu\text{m}$ 16bit digitalisation at 10 MHz
Optical lens	Camera lens; Nikon Inc., 35 mm focal length
Fluorescent screen	CdWO <sub>4</sub> single crystal, thickness 590 $\mu\text{m}$

was 4.42  $\mu\text{m}$ . Image slices were reconstructed from the series of projections based on a filtered back projection algorithm (Kak & Slaney, 1988). For the visualisation of the re-constructed voxel data and volumetric analysis, VGStudio MAX 2.1<sup>®</sup> was later used.

#### 4.6.4 Results and Discussion



(a) test set-up for the hourglass specimens



(b) slice of the reconstructed SR $\mu$ CT measurements close to the middle section of the uniaxially loaded specimen (100 mm plate)

Figure 4.36: Loading device and visualisation of the SR $\mu$ CT experiments (beamline HARWI-II)

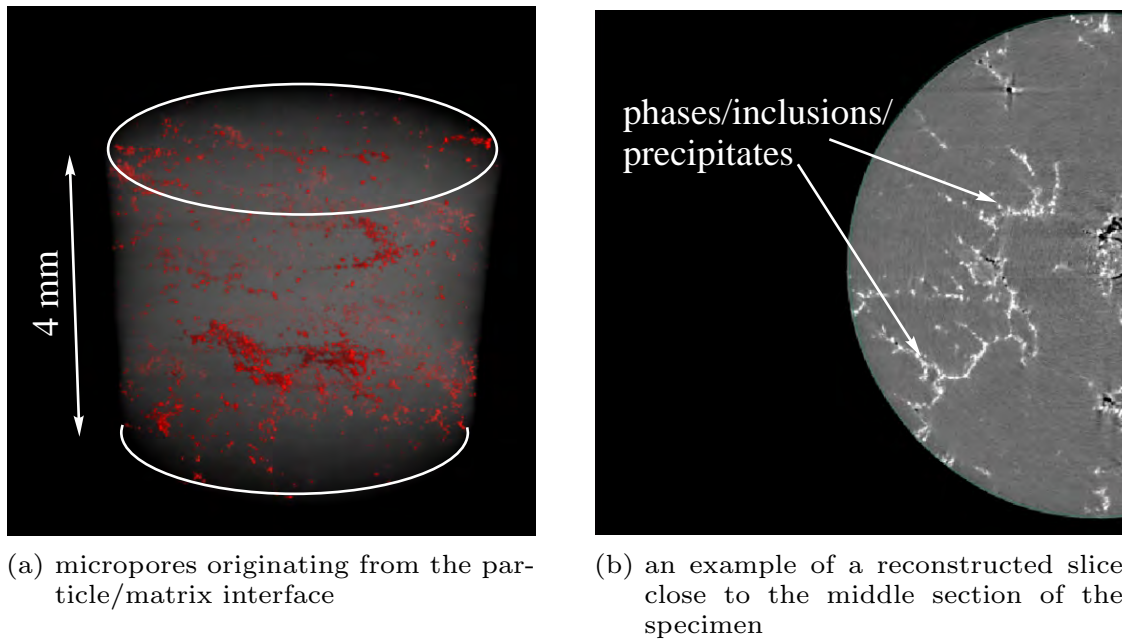


Figure 4.37: Re-construction of the hourglass specimen, see Figure 4.36(a) (100 mm plate, S-direction) with SR $\mu$ CT

#### 4.6.4.1 Uniaxial tests

Figure 4.36(b) shows a typical 2D cross-sectional image from the re-constructed tomography data set (uniaxial tensile loading<sup>6</sup>). A complex crack morphology can be seen at the centre of the image, with relatively spherical micropores (black) and complex intermetallic particle groups (white) in the surrounding matrix, cf. Figure 4.37(b). Particles in white are heterogeneous inclusions or precipitates of  $\text{Al}_2\text{Cu}$  and  $\text{Al}_2\text{CuMg}$  secondary phases. They appear in white due to different absorption related to copper. In Figure 4.37(b) the cluster network of these inclusions is evident (white layer). During monotonic loading decohesion takes place between these particles and the matrix resulting in void formation (several black dots appear on the grey background). The debonding is only observed at these clusters.

Figure 4.37(a) shows a 3D re-construction of the specimen with 4 mm scanning height. Damage is scattered all over the volume and has the same pattern as the particle layers which indicates that decohesion has been the underlying mechanism (red spots are voxels with a high contrast, i.e. damage). SR $\mu$ CT investigations on monotonically loaded specimens were a trial attempt to judge the capability of the tomography setup with respect to the resolution.

<sup>6</sup>In the figure, only an hourglass specimen is shown, but the same set-up was also used for 2 mm and 10 mm notched specimen.



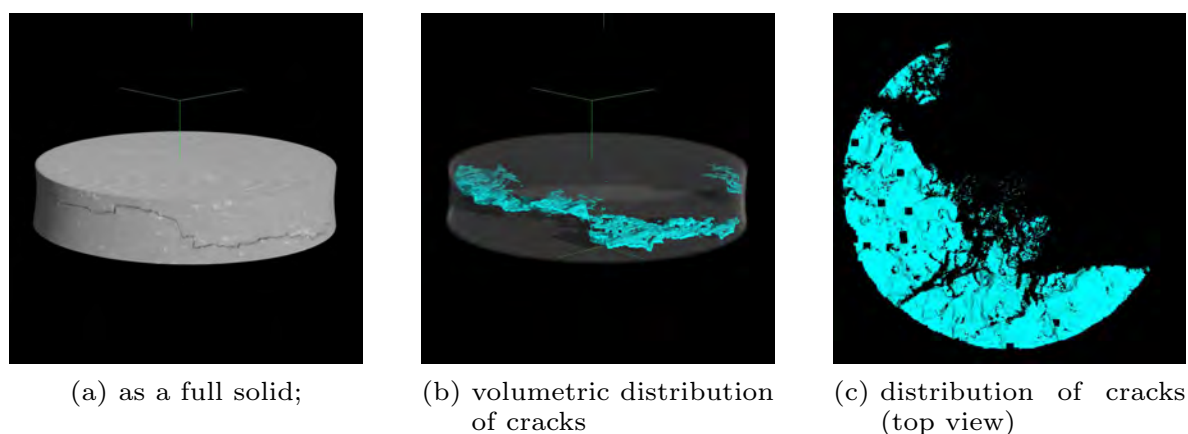


Figure 4.38: Re-constructed SR $\mu$ CT data; 3D images of the notched specimen (S-direction, 100 mm plate) (notch radius=4 mm), cf. (Khan et al., 2010)

#### 4.6.4.2 LCF tests

Earlier studies (Braun et al., 2006; Khan et al., 2010) on cyclically deformed notched specimens (4 mm notch radius) of the same alloy indicated that the crack front is neither a straight line nor does it lie in the symmetry plane of the specimen, cf. Figure 4.38(c). However, those specimens were deformed till the appearance of surface cracks and hence, the experiments gave no information on the initiation of damage its evolution.

Table 4.12: Volumetric analysis of Al2024-T351 (S-direction, 100 mm plate)

Specimen	Voxels, ROI (average)	Total volume (excl. noise)	Volume (high density objects)
2mm	4.1e8	16.6 mm <sup>3</sup>	0.1115 mm <sup>3</sup>
10mm	3.92e8	15.7 mm <sup>3</sup>	0.1563 mm <sup>3</sup>

In Figure 4.39, the number of voxels has been plotted against the considered attenuation coefficient for specimens failing under fatigue loading. Three areas can be distinguished based on the absorption level. Air which surrounds the specimen, as shown by a bounding box (see Figure 4.40) and noise in the system appear on the left of the histogram. Cracks, being a discontinuity physically belong to the same no absorption class. Aluminium being the matrix material comes next followed by high density heavy copper particles. The composition in terms of voxels is given in Table (4.12) above. In all cases, a

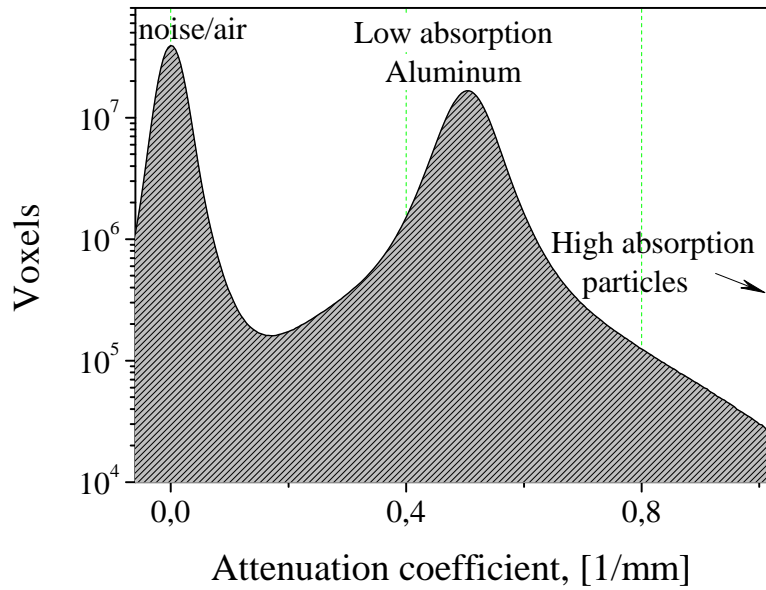


Figure 4.39: Attenuation coefficient measured by using SR $\mu$ CT. From left to right, the grey values of the different constituents are displayed, i.e. noise/air, matrix material, heterogeneous inclusions/particles

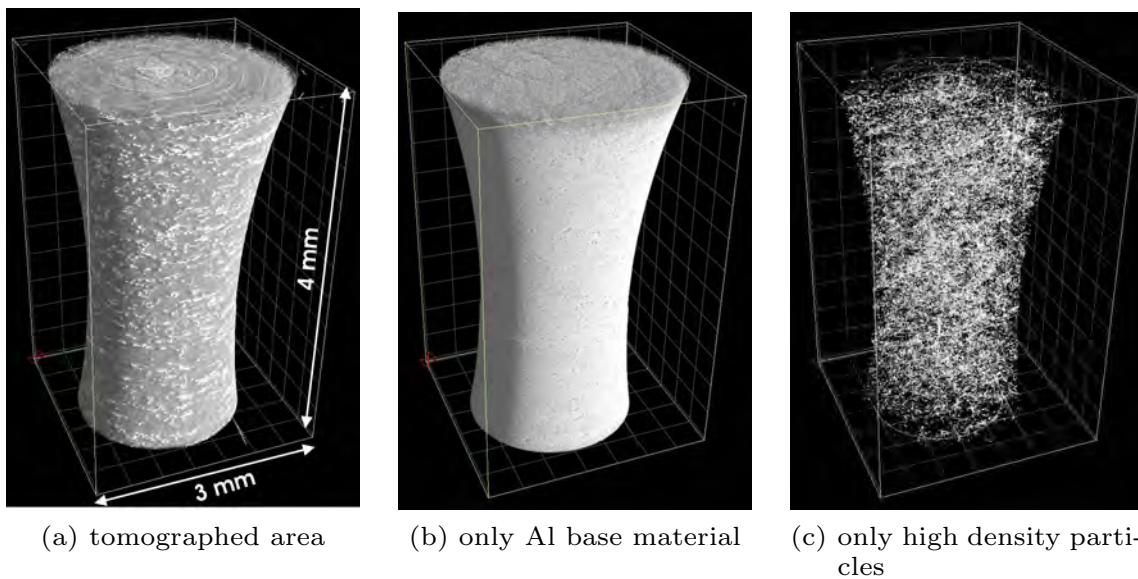


Figure 4.40: Results of the SR $\mu$ CT; Cyclically loaded RNB specimen with a notch radius of 10 mm (S-direction, 100 mm plate, see Figure 4.32)

specific region of interest ROI (region of interest, cf. Figure 4.40(a),(b),(c)) is extracted which excludes noise and other experimental tolerances.

The volumetric analysis shows an unusually high volume of particles at the middle of the plate, the site which forms the notches of the specimen. Among the particles, damage initiates from the bigger ones located near the notch root for cyclic loading and at the middle of the specimen for monotonic loading.

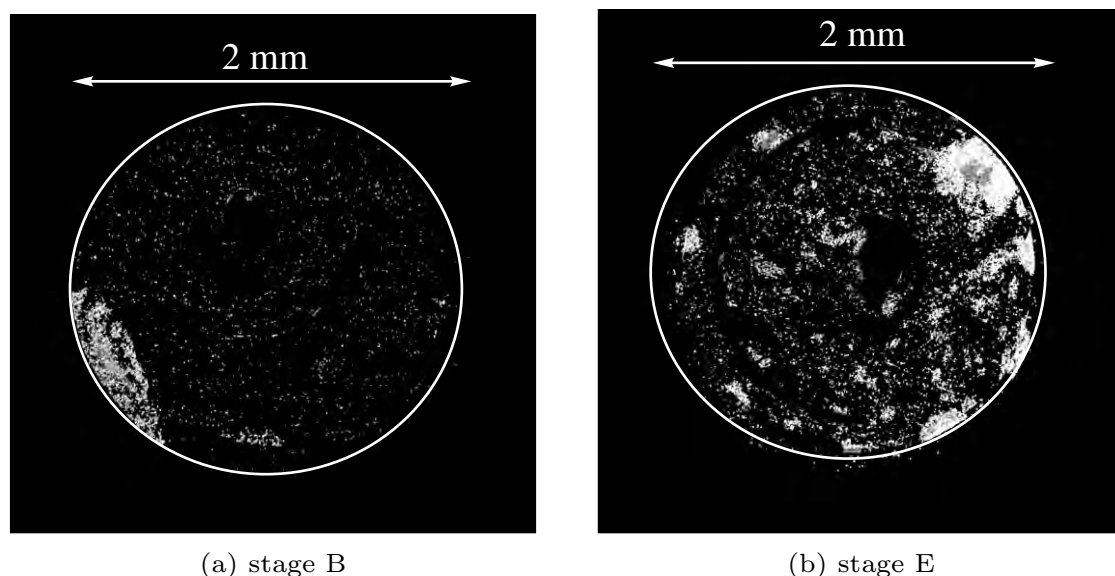


Figure 4.41: Results of the SR $\mu$ CT for cyclic loading conditions: Top views of damage in the specimen (S-direction, 100 mm plate) with a 10 mm notch at different loading stages, see Figure 4.34(b)

Cracks already nucleate during the hardening stage (stage B, Figure 4.34(b)). Figure 4.41(a) shows a small micro-crack initiating from the surface of the 10 mm notch specimen and the distribution of high density particles all over the volume. Subsequently, during the saturation and degradation stage (stage D and E, Figure 4.34(b)), multiple cracks near the surface evolve (large particles) and merge into a major surface crack resulting eventually in the total failure (Figure 4.41(b)). A similar observation has also been noted for 2 mm notches. However, a single crack dominates the failure process in this case. The vacant dark rings (Figure 4.41) near the edge appear black due to the removal of the artifacts during post processing.

Figure 4.42 shows cracks in the interior of the specimen. Accordingly, their propagation is very complex and shows a wavy path. After the tomography, some specimens have been longitudinally cut and the mid-plane has been examined using an optical microscope, cf. Figure 4.43. In the particular case of the 10 mm specimen at stage E, two cracks in addition to the primary crack

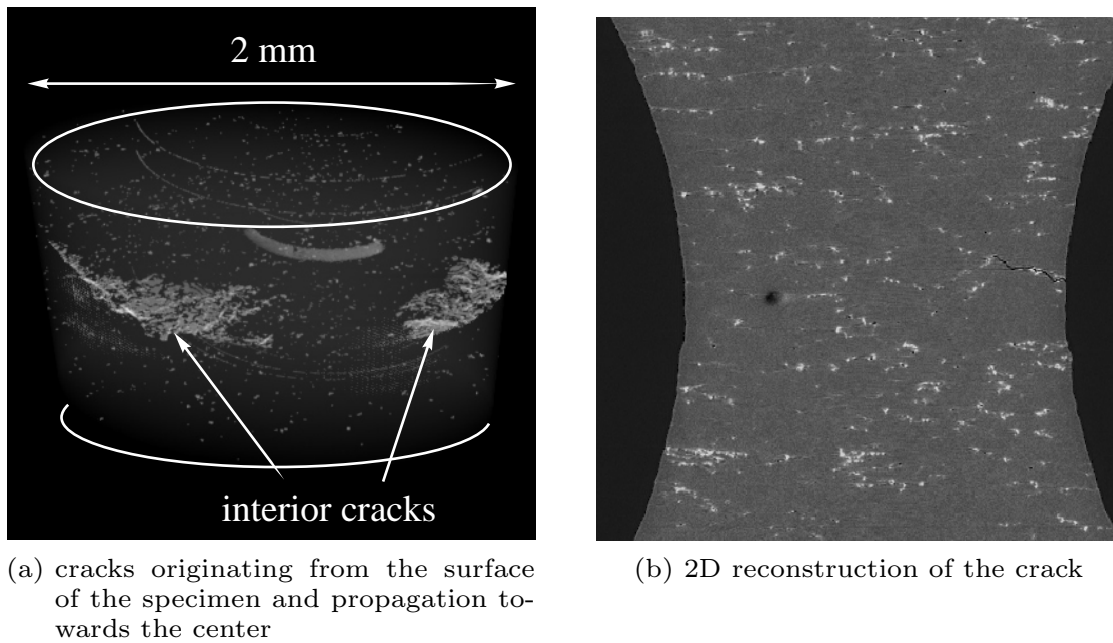


Figure 4.42: Results of the SR $\mu$ CT: Cyclically loaded hourglass specimens (S-direction, 100 mm plate)

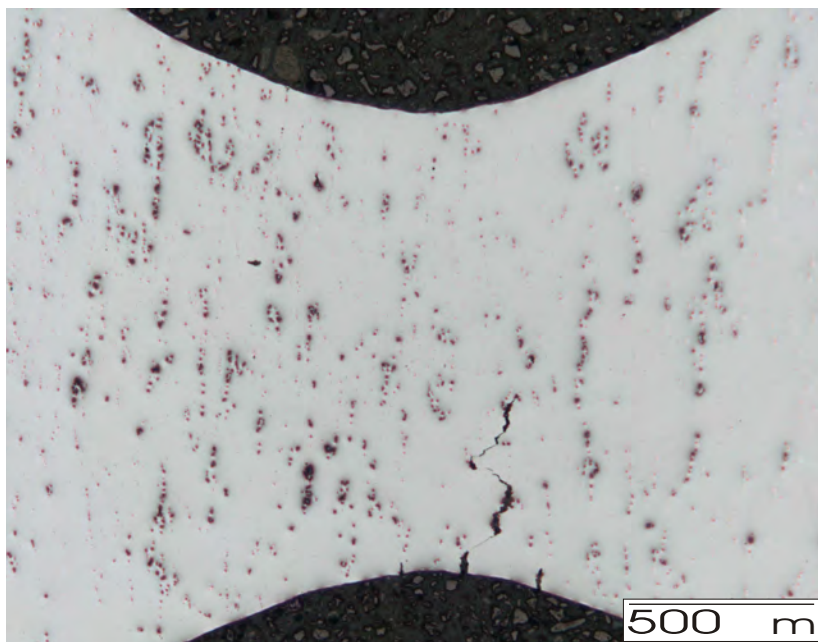


Figure 4.43: Results of an optical microscopy study: RNB with 10 mm notch (S-direction, 100 mm plate) at stage E, longitudinally cut and polished afterwards

have formed at the surface (81 and 63  $\mu\text{m}$  length, respectively). The primary crack connects various clusters of particles and has a length of 752  $\mu\text{m}$ . The resulting fracture surfaces of the 2 mm as well as of the 10 mm notch specimen, now generated by the SR $\mu$ CT data, are depicted in Figure 4.44. Numerous subsurface cracks can be seen under the fracture surface for the 10 mm notch specimen, whereas no such cracks were detected for the 2 mm notch specimen.

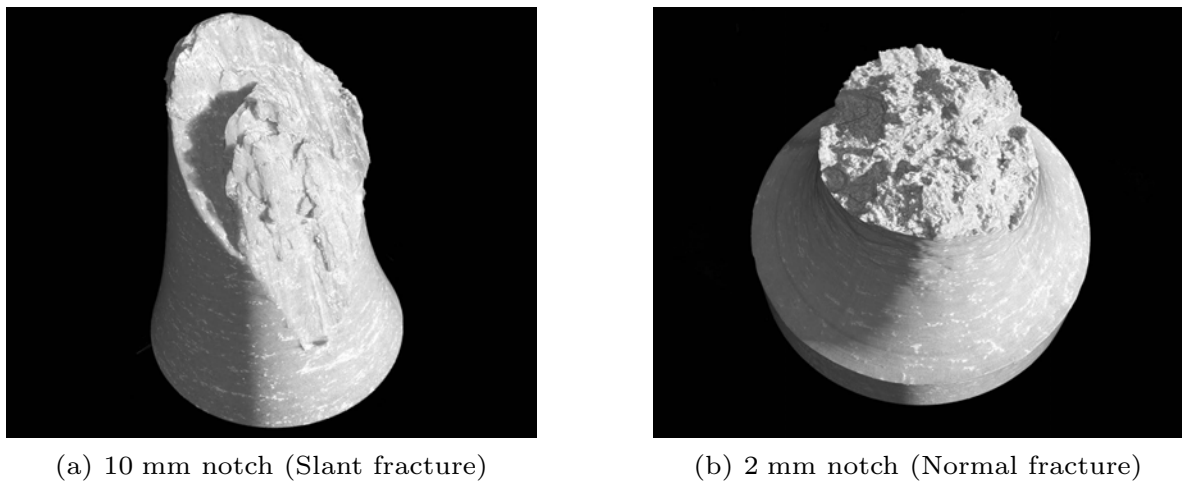


Figure 4.44: Results of the SR $\mu$ CT: Fractured surfaces (S-direction, 100 mm plate)

#### 4.6.5 Concluding remarks - X-ray tomography

By using the aforementioned measuring technique, the frequently postulated statement that a macroscopic crack forms at the surface in case of fatigue, while it starts propagating in the interior for monotonic loading could be verified for the high-strength aluminium alloy Al2024. However and besides this commonly accepted fact, several additional new findings associated with low cycle fatigue could be also reported. Although some of those have already been conjectured earlier based on post-mortem analysis, cf. Khan et al. (2010), their final correctness could only be verified by the presented synchrotron micro-tomography measurements.

In addition to the already conjectured statements, the reported tri-axiality dependence on the failure process is completely new. More explicitly, the 2 mm and 10 mm notched specimens have different fracture mechanisms. While the crack originates from different particles at the notch root for lower tri-axiality (10 mm notch), a single straight crack initiating from the surface and eventually, resulting in fatal failure has been observed for the 2 mm notched specimen.

Equally important, decohesion of particles is the major source driving damage accumulation during the first loading stages. Such insights allow developing physically sound constitutive models. This will be discussed in the following chapters.

# 5 Modelling material damage by continuum mechanics

Although advanced material characterisation is the workhorse for understanding materials, accompanying computer simulations are often useful for getting further insights. For that purpose, the first section (5.1) of this chapter introduces the fundamentals in continuum damage mechanics starting with the concept of internal damage variables, principal of equivalent strain and modelling the evolution of damage. After that, a brief introduction to a ductile damage model, presented by Lemaitre & Desmorat (2005) is described suitable for anisotropic materials and for predicting low cycle fatigue lifetime in ductile materials. This section is completed by describing a procedure for the identification of the material parameters. In the concluding section (5.3), the model is applied to Al 2024 and conclusions are drawn.

## 5.1 Fundamentals

The proper and accurate modelling of material damage represent one of the crucial problems of continuum damage mechanics. It is possible to homogenise the true distribution of damage in a quasicontinuum by using properly defined internal variables that characterise damage. This idea is briefly discussed in the following section.

### 5.1.1 The concept of internal damage variables

Damage variables can be scalars, vectors, second-, fourth- or eight-order tensors. A scalar damage variable is sufficient to model isotropic damage processes (see Section 5.2), but modelling of anisotropic damage processes requires tensor-valued damage variables. A more detailed review of damage variables used to describe damage processes is given in Skrzypek & Ganczarski (1999).

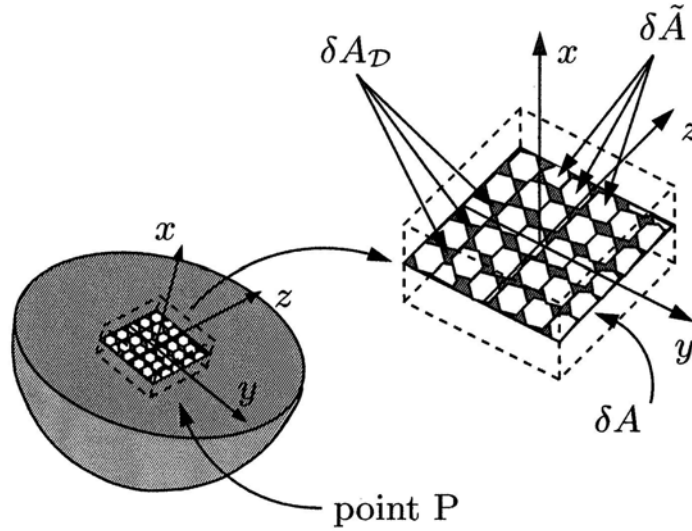


Figure 5.1: Scalar-valued damage variable - as defined by Kachanov (1958)

### 5.1.1.1 Scalar damage variables

In a pioneering paper, Kachanov (1958) proposed to characterise a gradual deterioration process of a microstructure by a scalar  $\psi$ , which he called *continuity*. For a completely undamaged material  $\psi=1$  and for a completely damaged material with no remaining load carrying capacity  $\psi=0$ . Consequently and according to Figure 5.1, damage within a certain plane is defined by

$$\psi = \frac{\delta\tilde{A}}{\delta A}, \quad \psi \in [0, 1], \quad (5.1)$$

where  $\delta\tilde{A}$  is the effective remaining area, which is deteriorated via microcrack and microvoid nucleation and evolution, and  $\delta A$  is the total area. Following Rabatnov (1969) scalar-valued damage accumulation can be equivalently described by the damage variable

$$\mathcal{D} = 1 - \psi = \frac{\delta A - \delta\tilde{A}}{\delta A}. \quad (5.2)$$

In the case of isotropic material

$$\mathcal{D} = \frac{\delta V_v}{\delta V}, \quad (5.3)$$

where  $\delta V$  and  $\delta V_v$  represent the void volume and the undamaged volume. If the distribution is identical in all spatial directions (spherical pores), damage can be conveniently measured by comparing the  $\delta V_v$  to the volume  $\delta V$  of the representative volume, i.e., element.



### 5.1.1.2 Second-order damage tensors

According to Figure 5.1, the damage variable  $\mathcal{D}$  depends on the position and orientation of the intersection area in the RVE. In the direction of the normal  $\mathbf{n}$ , the scalar equation is given as

$$\delta \tilde{A} = (1 - \mathcal{D}(\mathbf{n}))\delta A . \quad (5.4)$$

According to Murakami & Ohno (1981), (5.4) can be extended to a three dimensional case using normals  $\mathbf{n}_1$ ,  $\mathbf{n}_2$  and  $\mathbf{n}_3$  for three orthogonal directions

$$\delta \tilde{\mathbf{A}} = \tilde{\mathbf{n}}\delta \tilde{A} = (\mathbf{1} - \mathcal{D}) \cdot \mathbf{n}\delta A = (\mathbf{1} - \mathcal{D}) \cdot \delta \mathbf{A} , \quad (5.5)$$

where  $\mathcal{D}$  is a symmetric second-order damage tensor

$$\mathcal{D} = \sum_{i=1}^3 \mathcal{D}_i \mathbf{n}_i \otimes \mathbf{n}_i , \quad (5.6)$$

$\mathcal{D}_i$  and  $\mathbf{n}_i$  are the principal values and the unit vectors of principal directions of the damage tensor  $\mathcal{D}$ .

### 5.1.2 Principle of strain equivalence

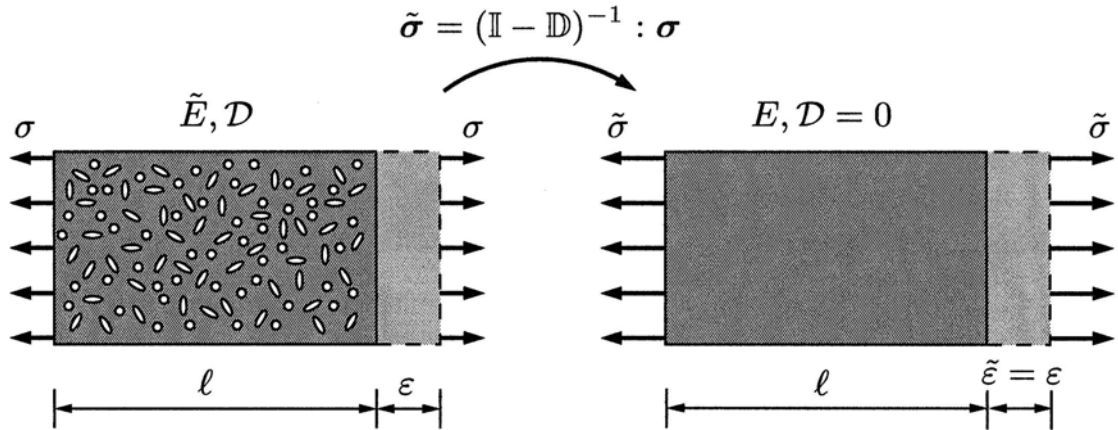


Figure 5.2: One-dimensional representation of strain equivalence concept (Chaboche, 1988)

In the previous section, different damage variables have been introduced based on purely geometrical considerations. Here, these variables are related to the stresses. For that purpose, equivalence principles are frequently used. The principle which will be used in the present thesis is the *principle of strain*

*equivalence* also known as *effective stress concept* (Chaboche, 1988; Lemaitre, 1992). It states that the strain associated with a damaged state under the applied stress  $\boldsymbol{\sigma}$  is equivalent to the strain associated with the undamaged state under the effective stress  $\tilde{\boldsymbol{\sigma}}$  (see Figure 5.2):

$$\tilde{\boldsymbol{\varepsilon}}(\tilde{\boldsymbol{\sigma}}, 0) = \boldsymbol{\varepsilon}(\boldsymbol{\sigma}, \mathbb{D}) . \quad (5.7)$$

Here,  $\mathbb{D}$  is an arbitrary tensor-valued damage variable. In the case of linear elasticity, the stress-strain relation in the undamaged material is represented by Hooke's law

$$\boldsymbol{\sigma} = \mathbb{C} : \boldsymbol{\varepsilon} , \quad (5.8)$$

where  $\mathbb{C}$  is the fourth-order *elastic stiffness* tensor. In the case of a damaged material, Hooke's law has a form

$$\boldsymbol{\sigma} = \tilde{\mathbb{C}} : \boldsymbol{\varepsilon} , \quad (5.9)$$

where  $\tilde{\mathbb{C}}$  is the fourth-order *damaged elastic stiffness* tensor. Based on the principle of strain equivalence (5.7), and on (5.9), the stress-strain relation in the undamaged configuration with undamaged elastic stiffness tensor reads

$$\tilde{\boldsymbol{\sigma}} = \mathbb{C} : \tilde{\boldsymbol{\varepsilon}} = \mathbb{C} : \boldsymbol{\varepsilon} = \mathbb{C} : \tilde{\mathbb{C}}^{-1} : \boldsymbol{\sigma} . \quad (5.10)$$

Thus, assuming for the sake of generality that the damage variable  $\mathcal{D}$  is represented by a fourth-order tensor,  $\mathbb{D}$  and the damaged elastic stiffness tensor  $\tilde{\mathbb{C}}$  are given as

$$\mathbb{D} = \mathbb{I} - \tilde{\mathbb{C}} : \mathbb{C}^{-1} \quad \text{and} \quad \tilde{\mathbb{C}} = (\mathbb{I} - \mathbb{D}) : \mathbb{C} , \quad (5.11)$$

where  $\mathbb{I}$  is the fourth-order *identity* tensor.

### 5.1.3 Modelling the evolution of damage

In ductile metallic materials like steels and aluminium, microvoid nucleation and growth have been recognised as key mechanisms of damage. Analysing the elongation of spherical or elliptical voids in a porous medium, Mc Clintock (McClintock, 1968) and Rice and Tracey (Rice & Tracey, 1969) initiated the research on void growth laws. Afterwards, many new developments in this field contributed to a number of ductile damage models or failure criteria. Today, the approaches are numerous and can be sorted broadly into three main classes : (i) abrupt failure criteria, (ii) porous metal plasticity, and (iii) continuum damage mechanics (CDM) approaches. For the first mentioned modelling approach, ductile failure is assumed when a micromechanical variable, for instance the cavity growth, cf. Rice et al. (Rice & Tracey, 1969), reaches a

critical characteristic material value. Regarding the second approach, damage effects are accounted for by a softening of the yield limit in dependence on the amount of porosity, cf. (Gurson, 1977; Needleman & Rice, 1978; Tvergaard & Needleman, 1984).

Finally, in the CDM approach, originated in the early works of Kachanov (Kachanov, 1958), softening effects associated with material damage are considered by means of thermodynamic internal state variables, see Section 5.1.1. In this framework, in contrast to porous plasticity theory, damage effects are accounted for by a degradation of material moduli like the elastic stiffness, see (5.9). Integrated within a thermodynamics framework, CDM models use as many internal state variables as there are mechanisms of deformation and material degradation to be accounted for, cf. (Steglich et al., 2008; Bonora et al., 2005).

## 5.2 Material law for ductile damage

In order to simulate the response of Al2024 (S-direction) under extreme cyclic loading (LCF), initially an anisotropic damage constitutive model proposed by Lemaitre (1992) in a CDM framework is used, since previous studies at Helmholtz-Zentrum Geesthacht (Graff, 2003) have indicated that micro-mechanically motivated models like GTN (Gurson, 1977) and Roussellier model (Roussellier, 1987) are inadequate for cyclic loading.

### 5.2.1 Elasto-plasticity

The constitutive behaviour of Al2024 is modelled first by means of the CDM approach proposed by Lemaitre & Desmorat (2005). This approach is based on rate-independent elasto-plasticity (isotropic and kinematic hardening) combined with an anisotropic damage evolution (with micro-defect closure effects). Further details can be found in (Lemaitre & Desmorat, 2005). For the sake of comprehensibility, an overview of the governing equations is presented in the following sections.

The model is based on the assumption of an additive decomposition of the strains into elastic  $\boldsymbol{\varepsilon}^e$  and plastic  $\boldsymbol{\varepsilon}^p$  parts. More precisely,

$$\dot{\boldsymbol{\sigma}} = \mathbb{C} : \dot{\boldsymbol{\varepsilon}}^e = \mathbb{C} : (\dot{\boldsymbol{\varepsilon}} - \dot{\boldsymbol{\varepsilon}}^p) , \quad (5.12)$$

where  $\dot{\boldsymbol{\sigma}}$  is the effective Cauchy stress tensor (rate) and  $\mathbb{C}$  is the 4th-order stiffness tensor. Yielding is governed by the von Mises-type function.

$$f = (\tilde{\boldsymbol{\sigma}} - \mathbf{Q}_k)_{\text{eq}} - R - \sigma_y , \quad (5.13)$$

with  $\mathbf{Q}_k$  being the back stress tensor,  $R$  representing a stress-like internal variable associated with isotropic hardening and  $\sigma_y$  denoting the (initial) yield stress. Here and henceforth,  $(\cdot)_{\text{eq}}$  is the equivalent stress measure of von Mises-type. The evolution of isotropic hardening and that of its kinematic counterpart are governed by an exponential law and an Armstrong-Frederick-type relation, respectively (Lemaitre & Chaboche, 1990; Lemaitre & Desmorat, 2005). More precisely,

$$R = R_\infty(1 - \exp(-br)) , \quad (5.14)$$

$$\dot{\mathbf{Q}}_k = \frac{2}{3}C\dot{\varepsilon}^p - \gamma\mathbf{Q}_k\dot{r} . \quad (5.15)$$

Here,  $R_\infty$  and  $b$  are parameters defining the isotropic hardening (saturation stress and saturation rate) and  $r$  is a strain-like internal variable (the equivalent plastic strain). Kinematic hardening is described by the material parameters  $C$  and  $\gamma$ .

### 5.2.2 Damage initiation - threshold of the stored energy

A review of the literature suggests that, in addition to empirical models like the Coffin-Manson life curve (Coffin, 1954) and Wöhler (Wöhler, 1858) curves (Section 3.3), several authors (Radhakri, 1980; Kliman & Bily, 1984) have proposed fatigue life curves based on plastic strain energy or related energy-based criteria, see also Section 3.3.2. Here, an identical concept has been followed, where the plastic stored energy  $w_s$  is an integral function of the hardening laws (5.16).

$$w_s = \int_0^t R_\infty (1 - \exp(-br)) \frac{A}{m} r^{\frac{1-m}{m}} \dot{r} dt + \frac{3}{4C} \mathbf{Q}_k^2 . \quad (5.16)$$

In (5.16),  $r$  is the accumulated plastic strain,  $\mathbf{Q}_k$  is the back stress tensor,  $A$ ,  $m$  are parameters defining the plastic stored energy function and  $R_\infty$ ,  $b$ ,  $C$  are additional parameters describing the cyclic plasticity model (see (5.14) and (5.15)). Damage initiation is assumed, if

$$w_s \geq w_D , \quad (5.17)$$

with  $w_D$  being a threshold value.

### 5.2.3 Damage evolution

Following the model presented in Lemaitre & Desmorat (2005), damage is described by a second-order damage tensor. More precisely, the stresses are defined by

$$\tilde{\boldsymbol{\sigma}} = \left( \mathbf{H}^{\mathbf{P}} \cdot \boldsymbol{\sigma}_+^{\mathbf{D}} \cdot \mathbf{H}^{\mathbf{P}} \right)^{\mathbf{D}} + \left( \mathbf{H}^{\mathbf{n}} \cdot \boldsymbol{\sigma}_-^{\mathbf{D}} \cdot \mathbf{H}^{\mathbf{n}} \right)^{\mathbf{D}} + \left[ \frac{\langle \boldsymbol{\sigma}_{\mathbf{H}} \rangle}{1 - \eta \mathcal{D}_{\mathbf{H}}} - \frac{\langle -\boldsymbol{\sigma}_{\mathbf{H}} \rangle}{1 - \eta h_{\mathbf{a}} \mathcal{D}_{\mathbf{H}}} \right] \mathbf{I}, \quad (5.18)$$

$$\mathbf{H}_{ij}^{\mathbf{P}} = (\mathbf{1} - \mathcal{D})_{ij}^{-1/2} \quad \text{and} \quad \mathbf{H}_{ij}^{\mathbf{n}} = (\mathbf{1} - \mathcal{D} h_{\mathbf{a}})_{ij}^{-1/2}, \quad (5.19)$$

where  $\boldsymbol{\sigma}_+^{\mathbf{D}}$ ,  $\boldsymbol{\sigma}_-^{\mathbf{D}}$  are the positive and the negative part of the deviatoric stresses (based on eigenvalues),  $\boldsymbol{\sigma}_{\mathbf{H}}$  is the hydrostatic stress,  $\langle \bullet \rangle$  are McCauly brackets and  $\eta$ ,  $h_{\mathbf{a}}$  are the hydrostatic damage sensitivity and the closure effect parameters, respectively.

According to Lemaitre & Desmorat (2005), the damage evolution law is assumed to be a function of the plastic strain rate  $\dot{\boldsymbol{\varepsilon}}^{\mathbf{P}}$  and the effective energy density  $\bar{Y}$ , i.e.,

$$\dot{\mathcal{D}}_{ij} = \left( \frac{\bar{Y}}{S} \right)^s |\dot{\boldsymbol{\varepsilon}}^{\mathbf{P}}|_{ij}. \quad (5.20)$$

Clearly,  $\bar{Y}$  depends implicitly on the stress state and hence, a tri-axiality dependence is naturally included.

### 5.2.4 Crack closure effect

Damage affects the elastic properties of a material, see (5.21). Accordingly, the same evolution equation is applied in case of tension or compression. Clearly, that is not physical. For this reason, a crack closure parameter  $h_{\mathbf{a}}$  is introduced. In case of  $h_{\mathbf{a}}=0$ , damage accumulation is considered in compression, while  $h_{\mathbf{a}}=1$  implies that tension and compression results in the same material degradation. For metals,  $h_{\mathbf{a}}$  remains close to 0.2, see Lemaitre (1992) and is considered a material parameter in what follows. Based on (Young's modulus in tension  $\tilde{E}_{\mathbf{t}}$ , compression  $\tilde{E}_{\mathbf{c}}$  and Poisson's ratio  $\nu$ ) it can be computed as (see (5.21)).

$$h_{\mathbf{a}} = \frac{1 - (\tilde{E}_{\mathbf{t}}/E)}{1 - (\tilde{E}_{\mathbf{c}}/E)}. \quad (5.21)$$

### 5.2.5 Meso-crack initiation

Concerning damage in fatigue of metals one can distinguish three stages of degradation:

- A first stage of micro-plasticity and the accumulation of dislocations without (or with small) damage, i.e.  $\mathcal{D} \approx 0$ .
- A second stage of micro-damage growth  $\dot{\mathcal{D}} \geq 0$ .
- Once damage reaches the critical value  $\mathcal{D} = \mathcal{D}_c$ , a meso-crack initiates which can be simulated with models for macrocrack propagation. Typically  $\mathcal{D}_c$  ranges between 0.2 and 0.5 for metallic sheets in literature, see Lemaitre & Desmorat (2005).  $\mathcal{D}_c$  calibrated by analysing the stable and unstable crack growth area  $\mathcal{D}_c = \frac{A_{\text{stable}}}{A_{\text{total}}}$ , (refer to Figure 4.27).

## 5.3 Simulation Results

To simulate the LCF response of the DLC-specimen (see Figure 4.4(b)) and the RNB specimen see Figure 4.4(a)), axi-symmetric FE models of the specimen geometries were used. Symmetry conditions are imposed in order to increase computational efficiency. The mesh size in the region of expected failure is of the same order as a representative volume element in metals (Lemaitre & Chaboche, 1990). The simulations are run by using ABAQUS v6.7 software with Z-mat as material library.

### 5.3.1 Material parameters for plasticity model

For the simulation of the cyclic mechanical response as described in earlier sections, the combined isotropic-kinematic hardening plasticity model discussed in Section 5.2.1 is used. Since no damage occurs within the first  $N_D^{\text{exp}}$  cycles (see Figure 5.3(a)), the material response is purely elasto-plastic (without damage). The material parameters were adjusted using experimental cyclic stress-strain curves of DLC-specimens (round bar specimen) with the experimental response for  $\Delta\varepsilon = 0.02$ . The resulting material parameters are summarised in Table (5.1). Since a von Mises flow rule is adopted, the tension-compression asymmetry is not captured (Figure 5.3(a)). However, this can easily be improved by using a more realistic yield function.

Table 5.1: Parameters defining the underlying elasto-plastic model according to Section 5.2.1 (DLC-specimen taken from S-direction of a 100 mm plate)

Elasticity		Plasticity				
$E$ , [MPa]	$\nu$	$\sigma_y$ , [MPa]	$R_\infty$	$b$	$\gamma$	$C$ , [MPa]
$7 \times 10^4$	0.3	284	150	4	80	$1.7 \times 10^4$

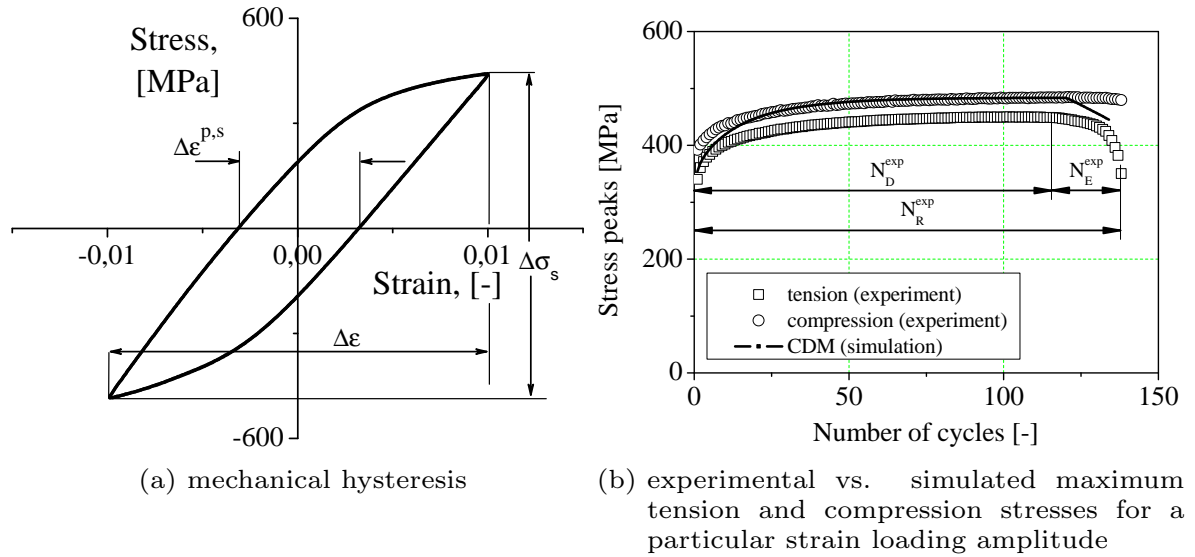


Figure 5.3: DLC-specimen (S-direction, 100 mm plate)  $\Delta\varepsilon = 0.02$ ;  $\Delta\varepsilon^P = 0.0063$ ;  $N_R^{\text{exp}} = 138$

### 5.3.2 Material parameters for the damage model

The material parameters are calibrated starting with those for the evolution and the threshold value of the stored plastic energy function (5.16). Frequently, an analytic method is applied, cf. (Otin, 2007). This method is based on the explicit calculation of function values for different number of cycles. It is assumed, that the isotropic hardening function reaches the saturation prior to damage initiation. This is a common observation in ductile steels. Al2024-T351 does not exhibit such a stabilisation and thus other parametrisation methods have to be used. In the present work the objective function

$$\{A, m, w_D\}^* = \arg \min_{\{A, m, w_D\}} \left( \sum_1^n \text{abs}(\log N_{D,i}^{\text{exp}} - \log N_{D,i}^{\text{sim}}(A, m, w_D)) \right). \quad (5.22)$$

is minimised, where  $N_{D,i}^{\text{exp}}$  and  $N_{D,i}^{\text{comp}}$  are the experimentally observed cycles before damage initiation and the numerically computed counterparts;  $n$  is the number of experiments (with different loading amplitudes). The problem is solved by implementing an algorithm in MATLAB. The final parameters are summarised in Table (5.2).

Table 5.2: Parameters of the model governing the evolution and the threshold values of the stored plastic energy (Section 5.2.2) and damage evolution (Section 5.2.3)

Stored plastic energy			Damage				
$m$	$A$	$w_D, (\text{MJ}/\text{m}^3)$	$S, (\text{MJ}/\text{m}^3)$	$s$	$\eta$	$h_a$	$\mathcal{D}_c$
3.9	0.0113	0.897	1.3	1.0	2.8	0	0.1

The choice of the damage parameters is motivated by the macroscopic material behaviour. In several experiments with DLC-specimens no degradation of the mechanical properties was observed. The decreasing of stresses showed an abrupt or *quasi-brittle* character. A fast evolution of damage and a small value of critical damage  $\mathcal{D}_c$  suit such a material behaviour well. The parameters for abrupt fracture and gradual degradation of the material behaviour (e.g. Figure 5.3) are given in Table (5.2). Smooth round bars (DLC) extracted from S-direction of the 100 mm plate have less ductility and fracture strain (uniaxial tensile tests) as compared to flat specimens (refer to Figure 4.3, p.g 18 and Figure 4.11, p.g 26). A consideration of the non-destructive testing (Figure 4.38(c)) roughly led to a value of  $\mathcal{D}_c = 0.1$ .

The hydrostatic damage sensitivity coefficient  $\eta$  is typically set to  $\eta \approx 3$ , see (5.18) (Lemaitre, 1992). The damage evolution parameters  $\mathcal{D}_c$ ,  $S$  and  $s$  were adjusted without any optimisation technique taking crack closure effect totally into account ( $h_a = 0$ , see (5.21)).

### 5.3.3 Simulation of fatigue life time of DLC-specimens

Figure 5.4 shows the results of FEM simulations with the set of CDM-parameters taken from, Table (5.1) and Table (5.2). A standard representation of LCF for uni-axial cyclic loading is based on the relation between plastic strain amplitude  $\Delta\varepsilon^P$  and number of cycles to rupture  $N_R$  (in logarithmic scale). This results in the so-called Coffin-Manson relation (see Section 3.3.2). For the sake of comparison, experimental results, together with the Coffin-Manson



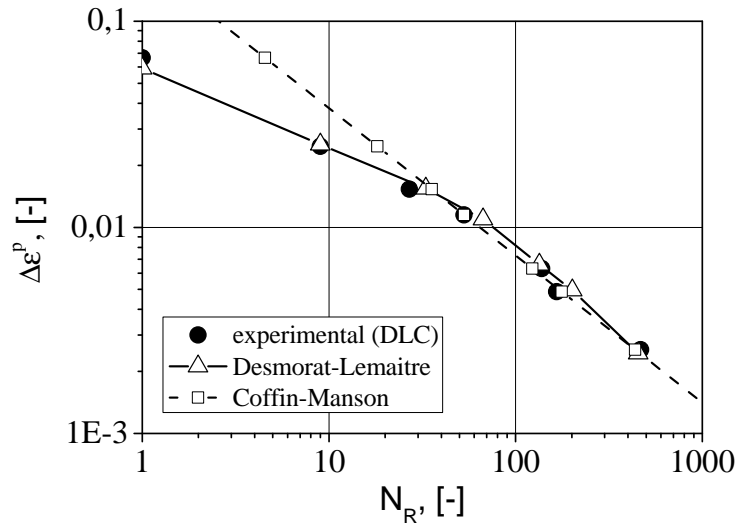


Figure 5.4: Experimental vs. simulated (For Desmorat-Lemaitre, see Section 5.2 and for Coffin-Manson curve, see (3.2)) fatigue response of DLC-specimens (S-direction, 100 mm plate)

model, are shown as well. The parameters of the Coffin-Manson model are  $C_{MC} = 0.196$  and  $\gamma_{MC} = 1.4$ , see (3.2).

According to Figure 5.4, the CDM fits almost perfectly the experimental data. For all loading amplitudes the agreement between the experimental observations and the numerically predicted response is remarkable. Furthermore, the predictions of the Coffin-Manson model are very good as well. Only if failure occurs in less than 30 cycles, this purely empirical model cannot be applied anymore. However, it bears emphasis that although both models lead to realistic results for more than 30 loading cycles, only the CDM approach is based on fundamental physical principles such as the second law of thermodynamics and equally importantly, only the CDM model can also be applied to more complex engineering problems, i.e., it is structure independent.

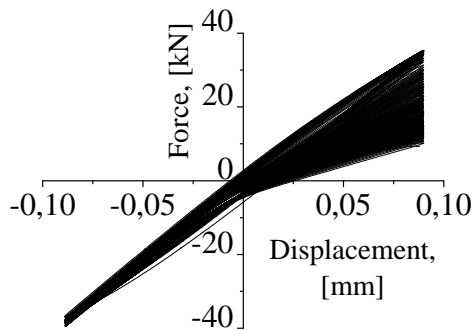
The experimental results (number of cycles) for different strain ranges are presented in Table (5.3) compared to simulated results obtained. Here  $\Delta \epsilon^P$  represents the strain amplitude for stabilised conditions Figure 5.3(a), i.e., when the peak stress remains constant from cycle to cycle.

#### 5.3.4 Lifetime prediction, RNB specimens

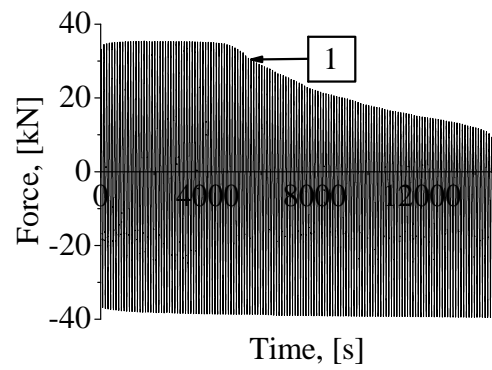
An example of a typical force-displacement and force-time response of the notched specimen is presented in Figure 5.5(a).

Table 5.3: Experimental results for smooth round bars (abbreviation DLC) taken from S-direction of the 100 mm plate

Specimen / $\Delta l$ [mm]	$\Delta \varepsilon$	$\Delta \varepsilon^P$	$N_D^{\text{exp}}$	$N_E^{\text{exp}}$	$N_R^{\text{exp}}$	$N_R^{\text{sim}}$
DLC / 0.8	0.08	0.0664	1	-	1	-
DLC-1 / 0.4	0.04	0.0247	9	1	10	13
DLC-2 / 0.3	0.03	0.0153	27	3	30	34.5
DLC-3 / 0.25	0.025	0.0115	48	5	53	67
DLC-4 / 0.2	0.02	0.0063	116	22	138	164
DLC-5 / 0.18	0.018	0.00487	145	21	166	201



(a) force-displacement



(b) force-time

Figure 5.5: Mechanical responses of the notched specimen (2mm notch,  $\Delta l = 0.02$  mm) extracted from S-direction of the 100 mm plate. Point 1 indicates the formation of a crack at the surface of the specimen.

The curves are similar to those of the DLC-specimen. The two stages of material hardening and degradation as mentioned formerly are evident (see Figure 5.5(b)). In contrast to the DLC-specimens, the second stage is significantly longer. This will be explained in the following.

The results of FE simulations reveal that with decrease of loading amplitude and increase of notch curvature the plastic deformation will be localised in the notch root. At the same time, the remaining volume of the specimen deforms purely elastically. If loading is further increased, this leads to crack propagation in an almost fully elastic specimen. Thus, from a structural point of view, this problem is mostly related to linear elastic fracture mechanics. Evidently, the aforementioned CDM approach is not well suited for the modelling of such a process. Therefore, crack initiation (Point 1 in Figure 5.5(b)) is chosen as the state defining  $N_R$ , see (4.1).

The results of the FEM simulation are compared to those of the experiments in Figure 5.6. The results, presented in Figure 5.6, show the mechanical response for extreme combinations of notch geometries and loading amplitudes. The best prediction was achieved for the 10 mm notch and the highest loading amplitude (Figure 5.6(a)). Although the numerical results are promising, some differences compared to the experimental data can be seen. One possible reason for this is the calibration method, i.e., for calibrating the material parameters, the onset of crack initiation is required (see point 1, Figure 5.5(b)). However, this point is not defined precisely by the conducted experiments (certain assumptions were necessary). Additionally, further investigations concerning the limits of the model (small strain amplitude, high stress tri-axiality) are required.

By analysing Figure 5.6(b), the limits of the CDM approach can be estimated. More precisely, the amplitude of the imposed displacement is so small, that after stabilisation of the hysteresis due to saturation of isotropic hardening, the hysteresis width is very small. Accordingly, the rate of further plastic strains will be very small as well. As a consequence, the stored plastic energy increases only very slowly and hence, damage initiation will not occur within a reasonable number of cycles ( $w_s < w_D$ ). The comparison of the predicted fatigue lifetime is summarised in Table (5.4). From Table (5.4) the relative error in the predicted lifetime can be computed.

Two damage distributions in loading direction at the rupture time point are shown in Figure 5.7. The region of crack initiation is predicted very accurately. It is in excellent agreement with similar investigations for ductile steels (Pirondi et al., 2006). The major difference as compared to the distribution of damage in steel is the pronounced localisation of damage in the notch root.

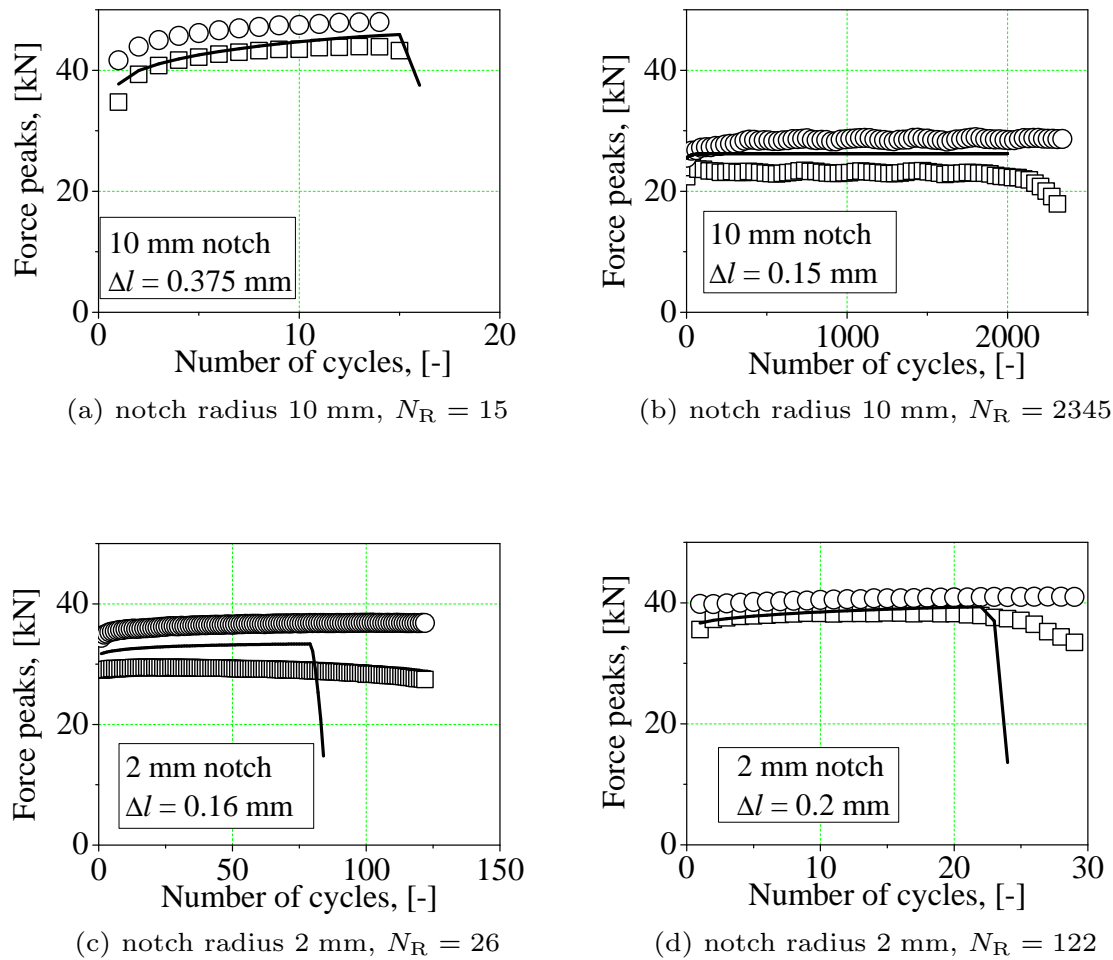


Figure 5.6: Experimental ( $\circ$ - tension,  $\square$ - compression) vs. simulated (- CDM) force peaks. The simulation in (b) was stopped due to saturation of the plastic energy function (2000 cycles)

Table 5.4: Comparison of the simulation results to the experimental data for the notched specimens (S-direction, 100 mm plate)

Notch radius (mm)	$\Delta l$ (mm)	$N_D^{\text{exp}}$	$N_D^{\text{sim}}$	$N_R^{\text{exp}}$	$N_R^{\text{sim}}$
10	0.375	14	15	15	16
10	0.200	204	378	431	383
10	0.150	2010	— <sup>a</sup>	2345	— <sup>a</sup>
2	0.20	19	22	26	24
2	0.18	36	43	55	45
2	0.16	63	79	122	84

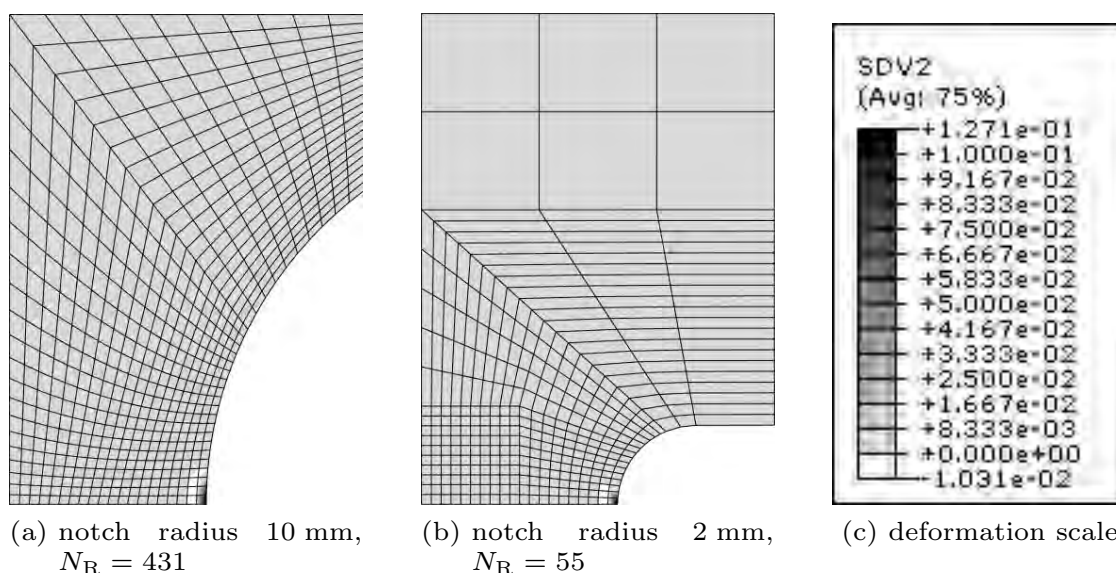


Figure 5.7: Distribution of damage in loading direction at the rupture time point ( $N = N_R$ )

## 5.4 Conclusions

While analysing the predictive capability of the Desmorat-Lemaitre CDM model (Lemaitre & Chaboche, 1990) for high load reversals under various stress states and lifetimes, it was found that for simple stress states, the predicted results have shown good agreement with experimental data. In contrast to the Coffin-Manson model, the CDM approach can even be applied to the analysis of material failure in less than 30 cycles. However and even more importantly, the CDM approach is, in contrast to the Coffin-Manson model, based on fundamental physical principles such as the second law of thermodynamics and hence, it can also be applied to more complex engineering problems, i.e., it is structure independent. This was demonstrated by analysing more complex geometries. Again, the lifetime prediction was in good agreement with experiments. It was shown, that with an increased tri-axiality (curvature of notch) and an increased number of cycles to rupture, the initiation of damage will be overestimated and the number of cycles to rupture will be underestimated.

The proposed CDM has already been validated for very ductile materials e.g. certain steels for which it is well suited. Although yields also reasonable results in case of Al2024 for some loading types, an overestimation of the lifetime could sometimes be seen - particularly for low strain amplitudes. This is in line with the experimental measurements discussed in Chapter 4 where in addition to ductile fracture, quasi-brittle-type damage accumulation was also observed. Thus, the model could be improved by adding a quasi-brittle-type damage approach.

## 6 A novel coupled damage model

According to the conclusions of Chapter 5, the model proposed by Lemaitre & Desmorat (2005) does not capture all damage modes relevant for the high-strength aluminium alloy Al2024. More precisely, the numerically predicted mechanical response as well as the material characterisation given in Chapter 5, point out the need for considering also a quasi-brittle-type damage mechanism. In the present chapter, such an extension is discussed. The present chapter is structured as follows: First, the extended constitutive model is introduced and explained in detail. Subsequently, a material parameter identification strategy is presented. In the last section, benchmarks (smooth round and flat specimens) demonstrate the performance of the coupled ductile-brittle law.

### 6.1 Fundamentals

In the current section, a novel coupled ductile-brittle damage model suitable for the numerical analysis of LCF in aluminium alloys is outlined. For the ductile damage model, an evolution law is used which depends on the plastic strain rate and the energy release rate as proposed by Lemaitre, cf. (Lemaitre, 1992) (Section 5.2). However, in contrast the framework in Lemaitre (1992), not only effective CAUCHY stresses but also effective hardening stresses are considered, cf. (Grammenoudis et al., 2009). For the brittle damage accumulation, a novel damage indicator function is introduced which depends also on the energy release rate and thus, on the elasto-plastic strain accumulation. Its related damage evolution is controlled by the damage mechanism associated with fatigue crack growth. The introduction of a shift tensor, which plays a similar role as the back stress in elasto-plasticity, allows the consideration of damage accumulation under cyclic loading. Throughout the chapter, a geometrically linearised setting is again considered where the global strains are coupled additively according to

$$\boldsymbol{\varepsilon} = \boldsymbol{\varepsilon}^e + \boldsymbol{\varepsilon}^p . \quad (6.1)$$

Here,  $\boldsymbol{\varepsilon}$  represents the total strains, and  $\boldsymbol{\varepsilon}^e$  and  $\boldsymbol{\varepsilon}^p$  are the elastic and the plastic parts of  $\boldsymbol{\varepsilon}$ .

In the following sections  $(\cdot)^p$  and  $(\cdot)^b$  denote internal constitutive variables associated to the ductile (plastic) and the brittle damage model, respectively.

### 6.1.1 The ductile damage model

For describing typical plastic effects such as the BAUSCHINGER effect, cyclic hardening up to saturation as well to allow a good approximation of the plastic hysteresis curve (see (Chaboche & Lemaitre, 1994) pg.234), three back stress tensors  $\mathbf{Q}_k^{(j)}$ , ( $j = 1, 2, 3$ ) and an isotropic hardening stress  $Q_i$  are introduced. With these assumptions, a Helmholtz energy potential of the type

$$\rho \Psi^p = \psi \left( \frac{\boldsymbol{\varepsilon}^e : \mathbb{C} : \boldsymbol{\varepsilon}^e}{2} + \sum_{j=1}^3 H_k^{(j)} \frac{\boldsymbol{\alpha}_k^j : \boldsymbol{\alpha}_k^j}{2} + H_i \frac{\alpha_i^2}{2} \right), \quad (6.2)$$

is adopted in the following. Here,  $\mathbb{C} = k\mathbf{1} \otimes \mathbf{1} + 2\mu\mathbb{P}_{\text{dev}}$  is the isotropic elastic stiffness tensor involving the bulk and shear moduli  $k$  and  $\mu$ , respectively,  $H_i$  and  $H_k$  are hardening moduli and  $\alpha_i$  and  $\boldsymbol{\alpha}_k^{(j)}$  represent the strain-like dual variables to  $Q_i$  and  $\mathbf{Q}_k^{(j)}$ , respectively.  $\psi = (1 - \mathcal{D})$  is the so-called *continuity* which depends on the damage variable  $\mathcal{D}$ , see Section 5.1.1.1. According to (6.2) and in contrast to (Lemaitre, 1992), the complete stored energy function is reduced by  $\psi$  (Section 5.1.1.1) which may lie in the range  $[0,1]$ . Based on (6.2), the state variables can be derived in standard manner, i.e., by means of the gradients to the energy potential (6.2). More precisely,

$$\boldsymbol{\sigma} = \rho \frac{\partial \Psi^p}{\partial \boldsymbol{\varepsilon}^e} = -\rho \frac{\partial \Psi^p}{\partial \boldsymbol{\varepsilon}^p} = \psi \mathbb{C} : \boldsymbol{\varepsilon}^e, \quad (6.3)$$

$$\mathbf{Q}_k^{(j)} = -\rho \frac{\partial \Psi^p}{\partial \boldsymbol{\alpha}_k^{(j)}} = -\psi H_k^{(j)} \boldsymbol{\alpha}_k^{(j)} \quad (j = 1, 2, 3), \quad (6.4)$$

$$Q_i = -\frac{\partial \Psi^p}{\partial \alpha_i} = -\psi H_i \alpha_i. \quad (6.5)$$

Clearly, in contrast to the stress-like internal variables  $\mathbf{Q}_k^{(j)}$  and  $Q_i$  being defined by equations (6.4) and (6.5), the CAUCHY stress tensor  $\boldsymbol{\sigma}$  as dual variable to  $\boldsymbol{\varepsilon}^e$  follows from the second law of thermodynamics for fully reversible processes.

For modelling damage accumulation, the effective stress concept is utilised which is based on the principle of strain equivalence (see Section 5.1.2). In this connection, the undamaged state is defined by considering the virgin moduli  $\mathbb{C}$ ,



$H_i$  and  $H_k^{(j)}$  for vanishing damage ( $\mathcal{D} = 0$ ). Thus, the effective state variable ( $\tilde{\bullet}$ ) are given by

$$\tilde{\sigma} = \mathbb{C} : \tilde{\varepsilon}^e, \quad \tilde{\mathbf{Q}}_k^{(j)} = -H_k^{(j)} \tilde{\alpha}_k^{(j)} \quad (j = 1, 2, 3), \quad \tilde{Q}_i = -H_i \tilde{\alpha}_i. \quad (6.6)$$

By enforcing the conditions of strain equivalence, i.e.,  $\tilde{\varepsilon}^e = \varepsilon^e$ ,  $\tilde{\varepsilon}^p = \varepsilon^e$ ,  $\tilde{\alpha}_k^{(j)} = \alpha_k^{(j)}$  and  $\tilde{\alpha}_i = \alpha_i$ , the relationships

$$\tilde{\sigma} = \frac{\sigma}{\psi}, \quad \tilde{\mathbf{Q}}_k^{(j)} = \frac{\mathbf{Q}_k^{(j)}}{\psi} \quad (j = 1, 2, 3), \quad \tilde{Q}_i = \frac{Q_i}{\psi} \quad (6.7)$$

between the effective stress-like variables ( $\tilde{\bullet}$ ) and their physical counterparts ( $\bullet$ ) can be derived.

For deciding whether a considered loading step is dissipative or fully reversible, a yield function  $\phi^p$  is introduced. It is assumed that this function depends solely on effective stresses. More precisely, a VON MISES yield function of the type

$$\phi^p = \sqrt{\frac{3}{2} \text{dev}(\tilde{\sigma} - \sum_{j=1}^3 \tilde{\mathbf{Q}}_k^{(j)}) : \text{dev}(\tilde{\sigma} - \sum_{j=1}^3 \tilde{\mathbf{Q}}_k^{(j)}) - (\tilde{Q}_i + Q_0^{\text{eq}})} \leq 0 \quad (6.8)$$

is adopted where  $Q_0^{\text{eq}}$  represents the initial radius of the elastic domain and  $\text{dev}(\bullet)$  is the deviatoric projector, i.e.,  $\text{dev}\sigma = \sigma - 1/3\text{tr}(\sigma)\mathbf{1}$ . Hence, according to the effective stress (see Section 5.1.1.1) concept, damage and elasto-plastic effects are uncoupled, i.e., the yield function is independent of  $\mathcal{D}$ . However, a kinetic coupling still exists, since the damage evolution is affected by the plastic strain rate. This will be shown explicitly later.

The model is completed by suitable evolution equations. For providing enough flexibility even for non-linear kinematic hardening, the framework of *generalised standard media* is utilised here, cf.(Chaboche & Lemaitre, 1994). Within this framework, the evolution laws are derived from a plastic potential  $\bar{\phi}^p$ . Similar to (Lemaitre, 1992; Chaboche & Lemaitre, 1994),  $\bar{\phi}^p$  is assumed to be of the type

$$\bar{\phi}^p = \phi^p + \frac{Y^M}{MS_1\psi(1-\mathcal{D})^K} + \sum_{j=1}^3 \frac{B_k^{(j)}}{H_k^{(j)}} \frac{\tilde{\mathbf{Q}}_k^{(j)} : \tilde{\mathbf{Q}}_k^{(j)}}{2} + \frac{B_i}{H_i} \frac{\tilde{Q}_i^2}{2}. \quad (6.9)$$

Here,  $M$ ,  $S_1$  and  $K$  are material parameters describing the damage evolution and  $B_k^{(j)}$ ,  $B_i$  are material parameters controlling the saturation values of the hardening stresses according to ARMSTRONG-FREDERICK. Furthermore,

$$Y^p = -\rho \frac{\partial \Psi^{\text{eq}}}{\partial \mathcal{D}} = \frac{\varepsilon^e : \mathbb{C} : \varepsilon^e}{2} + \sum_{j=1}^3 H_k^{(j)} \frac{\alpha_k^{(j)} : \alpha_k^{(j)}}{2} + H_i \frac{\alpha_i^2}{2}. \quad (6.10)$$

is the energy release rate. Complying with the framework of generalised standard media cf. (Chaboche & Lemaitre, 1994), the evolution laws are postulated as

$$\dot{\boldsymbol{\varepsilon}}^p = \lambda^p \frac{\partial \bar{\phi}^p}{\partial \boldsymbol{\sigma}} = \lambda^p \frac{\partial \bar{\phi}^d}{\partial \tilde{\boldsymbol{\sigma}}} : \frac{\partial \tilde{\boldsymbol{\sigma}}}{\partial \boldsymbol{\sigma}} = \frac{\lambda^p \mathbf{n}}{\psi} = p \mathbf{n} . \quad (6.11)$$

$$\begin{aligned} \dot{\boldsymbol{\alpha}}_k^{(j)} &= \lambda^p \frac{\partial \bar{\phi}^p}{\partial \mathbf{Q}_k^{(j)}} = \lambda^p \frac{\partial \bar{\phi}^p}{\partial \tilde{\mathbf{Q}}_k^{(j)}} : \frac{\partial \tilde{\mathbf{Q}}_k^{(j)}}{\partial \mathbf{Q}_k^{(j)}} \quad (j = 1, 2, 3), \\ &= \frac{\lambda^p}{\psi} \left( -\mathbf{n} + \frac{B_k^{(j)}}{H_k^{(j)}} \tilde{\mathbf{Q}}_k^{(j)} \right) = -p \left( \mathbf{n} + B_k^{(j)} \boldsymbol{\alpha}_k^{(j)} \right), \end{aligned} \quad (6.12)$$

$$\dot{\alpha}_i = \lambda^p \frac{\partial \bar{\phi}^p}{\partial Q_i} = \lambda^p \frac{\partial \bar{\phi}^p}{\partial \tilde{Q}_i} : \frac{\partial \tilde{Q}_i}{\partial Q_i} = \frac{\lambda^p}{\psi} \left( -1 + \frac{B_i}{H_i} \tilde{Q}_i \right) = -p(1 + B_i \alpha_i), \quad (6.13)$$

$$\dot{D}^p = \lambda^p \frac{\partial \bar{\phi}^p}{\partial Y} = p \frac{Y^{M-1}}{S_1(1-D)^K}. \quad (6.14)$$

Here, the definitions  $p := \frac{\lambda^p}{\psi}$  and  $\mathbf{n} := \frac{\partial \bar{\phi}^p}{\partial \boldsymbol{\sigma}}$  have been introduced. Hence,  $p$  equals the equivalent plastic strain rate, i.e.,

$$\sqrt{\frac{2}{3} \dot{\boldsymbol{\varepsilon}}^p : \dot{\boldsymbol{\varepsilon}}^p} = p. \quad (6.15)$$

The plastic multiplier  $\lambda^p \geq 0$  fulfils the KUHN-TUCKER complementarity conditions

$$\lambda^p \geq 0, \quad \phi^p(\boldsymbol{\sigma}, \mathbf{Q}_k^{(j)}, Q_i) \leq 0 \text{ and } \lambda^p \phi^p = 0 \quad (6.16)$$

as well as the consistency condition

$$\lambda^p \dot{\phi}^p = 0 \quad (6.17)$$

Considering  $\dot{\phi}^p = 0$ , together with (6.11, 6.13), the plastic multiplier  $p$  is derived as

$$p = \frac{\mathbf{n} : \mathbb{C} : \dot{\boldsymbol{\varepsilon}}}{\mathbf{n} : \mathbb{C} : \mathbf{n} + \sum_{j=1}^3 H_k^{(j)} \left( \frac{3}{2} + B_k^{(j)} \mathbf{n} : \boldsymbol{\alpha}_k^{(j)} \right) + H_i(1 + B_i \alpha_i)}. \quad (6.18)$$

It can be proved in a straightforward manner that the dissipation

$$\mathfrak{D} = \boldsymbol{\sigma} : \dot{\boldsymbol{\varepsilon}} - \rho \dot{\Psi} = \boldsymbol{\sigma} : \dot{\boldsymbol{\varepsilon}}^{\text{P}} + \sum_{j=1}^3 \mathbf{Q}_k^{(j)} : \dot{\boldsymbol{\alpha}}_k^{(j)} + Q_i \dot{\alpha}_i + Y \dot{\mathcal{D}}^{\text{P}} \geq 0, \quad (6.19)$$

as predicted by the discussed model, is non-negative and thus, the second law of thermodynamics is indeed fulfilled. This is a direct consequence of the convexity of the plastic potential  $\bar{\phi}^{\text{P}}$ , cf. (Chaboche & Lemaitre, 1994).

### 6.1.2 The brittle damage model

According to Chapter 4, a quasi-brittle-type damage mechanisms can also be observed in Al2024. Therefore, the ductile damage model, as discussed in the previous Section 6.1.1, is supplemented by an additional brittle-type damage model here. For deciding whether this additional model is active or not, a novel damage indicator function is proposed (analogous to a yield function). It reads

$$\phi^{\text{b}} = \frac{|Y^N - \Gamma|}{S_2} - (Q_{\text{b}} + Q_{\text{b}0}) \leq 0. \quad (6.20)$$

Here,  $(Q_{\text{b}} + Q_{\text{b}0})$  defines a threshold with a constant value  $Q_{\text{b}0}$  and variable value  $Q_{\text{b}}$ .  $\Gamma$  is the so-called *shift tensor* (here scalar-valued) which has been introduced for describing cyclic loading effects (similar to ARMSTRONG-FREDERICK type hardening),  $Y$  is the energy release rate (see (6.10)) and  $N$  is a material parameter. Assuming the internal variables governing ductile and brittle damage to be uncoupled, an additive form of the HELMHOLTZ energy is assumed. More precisely,

$$\rho \Psi^{\text{b}} = \psi Y^{\text{P}} + H_{\text{b}} \frac{\alpha_{\text{b}}^2}{2} + H_{\Gamma} \frac{\alpha_{\Gamma}^2}{2}. \quad (6.21)$$

$\alpha_{\Gamma}$  and  $\alpha_{\text{b}}$  are the strain-like variables dual to the energy-like variables  $\Gamma$  and  $Q_{\text{b}}$ , respectively. Both sets of variables are related by the state equations as

$$\Gamma = -\rho \frac{\partial \Psi^{\text{b}}}{\partial \alpha_{\Gamma}} = -H_{\Gamma} \alpha_{\Gamma} \quad \text{and} \quad Q_{\text{b}} = -\rho \frac{\partial \Psi^{\text{b}}}{\partial \alpha_{\text{b}}} = -H_{\text{b}} \alpha_{\text{b}}. \quad (6.22)$$

Accordingly,  $H_{\Gamma}$  and  $H_{\text{b}}$  can be interpreted as hardening parameters. Fully analogous to the elasto-plastic model presented before, the novel approach discussed here is further elaborated by postulating suitable evolution equations. For that purpose, the (convex) damage potential.

$$\bar{\phi}^{\text{b}} = \phi^{\text{b}} + \frac{B_{\text{b}}}{H_{\text{b}}} \frac{Q_{\text{b}}^2}{2} + \frac{B_{\Gamma}}{H_{\Gamma}} \frac{\Gamma^2}{2}, \quad (6.23)$$

is introduced. Here,  $B_\Gamma$  and  $B_b$  are material parameters which have a similar meaning as the saturation parameters  $B_i$  or  $B_k^{(j)}$  in the elasto-plastic rate problem. Based on (6.23), the evolution equations are derived by applying the framework of generalised standard media (see (Chaboche & Lemaitre, 1994)), i.e.,

$$\dot{\alpha}_\Gamma = \lambda^b \frac{\partial \bar{\phi}^b}{\partial \Gamma} = -\lambda^b \left( \frac{\text{sign}(Y^N - \Gamma)}{S_2} + B_\Gamma \alpha_\Gamma \right), \quad (6.24)$$

$$\dot{\alpha}_b = \lambda^b \frac{\partial \bar{\phi}^b}{\partial Q_b} = -\lambda^b (1 + B_b \alpha_b), \quad (6.25)$$

$$\dot{D}^b = \lambda^b \frac{\partial \bar{\phi}^b}{\partial Y} = \lambda^b \frac{\text{sign}(Y^N - \Gamma)}{S_2} N Y^{N-1}. \quad (6.26)$$

The multiplier  $\lambda^b \geq 0$  fulfils the KUHN-TUCKER complementarity conditions

$$\lambda^b \geq 0, \quad \phi^b(Y, \Gamma, Q_b) \leq 0 \quad \text{and} \quad \lambda^b \phi^b = 0, \quad (6.27)$$

together with the consistency requirement

$$\lambda^b \dot{\phi}^b = 0. \quad (6.28)$$

Considering  $\dot{\phi}^b = 0$ , the damage consistency parameter can be obtained as

$$\lambda^b = \frac{\frac{\text{sign}(Y^N - \Gamma)}{S_2} N Y^{N-1} \dot{Y}}{B_\Gamma \frac{\text{sign}(Y^N - \Gamma)}{S_2} (\Gamma_\infty - \Gamma) + B_b (Q_{b\infty} - Q_b)}, \quad (6.29)$$

where the limit stresses  $\Gamma_\infty = \frac{H_\Gamma \text{sign}(Y^N - \Gamma)}{S_2 B_\Gamma}$  and  $Q_{b\infty} = \frac{H_b}{B_b}$  have been introduced by assuming the limit values

$$\frac{\text{sign}(Y^N - \Gamma)}{S_2} + B_\Gamma \alpha_{\Gamma_\infty} = 0 \quad \text{and} \quad 1 + B_b \alpha_{b\infty} = 0, \quad (6.30)$$

in combination with (6.22). A careful analysis of the damage rate

$$\dot{D}^b = \left( \frac{N}{S_2} \right)^2 \frac{Y^{2(N-1)} \dot{Y}}{B_\Gamma \frac{\text{sign}(Y^N - \Gamma)}{S_2} (\Gamma_\infty - \Gamma) + B_b (Q_{b\infty} - Q_b)}, \quad (6.31)$$

reveals that  $\Gamma_\infty$  and  $Q_{b\infty}$  define an implicit threshold at which the damage rate accelerates to infinity. However, in contrast to the material model for ductile damage (see Section 5.2), it can be shown that the evolution of  $\Gamma$  or  $Q_b$  do not converge to  $\Gamma_\infty$  or  $Q_{b\infty}$ .

For the sake of completeness, the dissipation predicted by the model is given as well. It reads

$$\mathfrak{D} = \Gamma \dot{\alpha}_\Gamma + Q_b \dot{\alpha}_b + Y \dot{\mathcal{D}}^b \geq 0, \quad (6.32)$$

As mentioned before, since the evolution equations have been derived from a convex potential, i.e., within the framework of generalised standard solids, the second law of thermodynamics is automatically fulfilled.

### 6.1.3 The coupled ductile-brittle damage model

Finally, both models as outlined in the above section and the previous chapters (Section 5.2) are integrated into one ductile-brittle damage model. In line with the previous sections, the HELMHOLTZ energy of that model is assumed to be of the type

$$\rho \Psi = \psi \left( \frac{\boldsymbol{\varepsilon}^e : \mathbb{C} : \boldsymbol{\varepsilon}^e}{2} + \sum_{j=1}^3 H_k^{(j)} \frac{\boldsymbol{\alpha}_k^{(j)} : \boldsymbol{\alpha}_k^{(j)}}{2} + H_i \frac{\alpha_i^2}{2} \right) + H_b \frac{\alpha_b^2}{2} + H_\Gamma \frac{\alpha_\Gamma^2}{2}. \quad (6.33)$$

While the elasto-plastic part of the model is governed by the yield function (6.8), together with the evolution equations implied by the plastic potential (6.9), the brittle damage evolution is driven by (6.20) and (6.21). The total material degradation  $\mathcal{D}$  is assumed to be a superposition of the plastic part  $\mathcal{D}^p$  and the brittle part  $\mathcal{D}^b$ . More precisely, by introducing the composition factor  $\gamma^p = (1 - \gamma^b) \in [0, 1]$  fulfilling the compatibility equation  $\gamma^p + \gamma^b = 1$ , the coupling of both models is provided by

$$\psi = (1 - \gamma^d \mathcal{D}^d - \gamma^b \mathcal{D}^b). \quad (6.34)$$

This choice leads to an additive decomposition of the energy release into a ductile and a brittle part, i.e.,

$$Y^p = \gamma^p \left( \frac{\boldsymbol{\varepsilon}^e : \mathbb{C} : \boldsymbol{\varepsilon}^e}{2} + \sum_{j=1}^3 H_k^{(j)} \frac{\boldsymbol{\alpha}_k^{(j)} : \boldsymbol{\alpha}_k^{(j)}}{2} + H_i \frac{\alpha_i^2}{2} \right), \quad (6.35)$$

$$Y^b = \gamma^b \left( \frac{\boldsymbol{\varepsilon}^e : \mathbb{C} : \boldsymbol{\varepsilon}^e}{2} + \sum_{j=1}^3 H_k^{(j)} \frac{\boldsymbol{\alpha}_k^{(j)} : \boldsymbol{\alpha}_k^{(j)}}{2} + H_i \frac{\alpha_i^2}{2} \right), \quad (6.36)$$

which in turn, yields the additive structure of the damage evolution  $\mathcal{D} = \gamma^p \mathcal{D}^p + \gamma^b \mathcal{D}^b \in [0, \mathcal{D}_{\text{crit}}^p]$  with

$$\dot{\mathcal{D}}^p = p \frac{Y^{pM-1}}{S_1(1 - \mathcal{D}^p)^K}, \quad \mathcal{D}^p \in [0, \mathcal{D}_{\text{crit}}^p], \quad (6.37)$$

$$\dot{\mathcal{D}}^b = \lambda^b \frac{\text{sign}(Y^{bN} - \Gamma)}{S_2} N Y^{bN-1}, \quad \mathcal{D}^b \in [0, \mathcal{D}_{\text{crit}}^b]. \quad (6.38)$$

It can be shown in a relatively straightforward manner that this additive decomposition is also fulfilled for the dissipation, i.e.,

$$-\mathcal{D}\dot{Y} = -\lambda^p \frac{\partial \bar{\phi}^p}{\partial Y^p} - \lambda^b \frac{\partial \bar{\phi}^b}{\partial Y^b}. \quad (6.39)$$

Since each submodel (ductile damage and brittle damage) is thermodynamically consistent, i.e., obeys the second law of thermodynamics, the resulting model is indeed physically sound as well and the dissipation inequality is thus fulfilled. To guarantee a positive damage evolution for brittle damage, damage growth is considered for a half-cycle only, i.e., in case of a positive sign of  $(Y^{bN} - \Gamma)$ . Other approaches for the crack closure effect were discussed in Section 5.2.4.

## 6.2 Parameter identification

In the present section, the parameter identification strategy is outlined. First, the brittle damage law is calibrated to small fatigue crack growth considering Al2024 alloys. Then, the plastic moduli are defined by matching the experimentally observed elasto-plastic hysteresis curve for a medium strain range. For defining damage initiation, a reasonable activation criterion is presented which is finally calibrated to Al2024 by comparing the experimentally observed and numerically simulated number of cycles. For this purpose, the time to damage initiation, as observed in the experiments, is identified by the moment when the peak stress starts decreasing (Figure 5.3(b)). Finally, the softening process is described by the proposed ductile-brittle damage law. Its material parameters are found by comparing the experimentally observed and numerically simulated lifetimes. As optimisation strategy, an iterative approach has been used according to Needler & Mead (1965).

The fatigue tests on the so-called *Damage Low Cycle specimen* (DLC, smooth round bar) were performed and discussed in detail in Section 4.3.1.3. Additionally, circumferential Round Notch Bars (RNB) with various notch radii were designed to achieve a variation of the stress state in the middle cross section of the specimens. For detailed information, refer to Section 4.3.1.3. The experimental results (number of cycles) for different strain ranges are presented in Table (5.3), where  $\Delta\varepsilon^p$  represents the strain amplitude for stabilised conditions as shown in Figure 5.3.

Apart from the 100 mm thick plate, from whose thickness the aforementioned smooth round specimens have been taken, flat specimens (see Figure 4.10), extracted from L and T-direction of 4 mm sheets have also been experimentally tested and their response under LCF conditions recorded (see Section 4.3.2.2). For the accumulated plastic strain  $\Delta\varepsilon^P$  at the stabilised cycle the same definition has been used as for the smooth round bars (see Figure 5.3). Selected results from the experimental testing are in Table (4.7).

### 6.2.1 Calibration of the brittle damage model to Al2024

The novel brittle damage law discussed in Section 6.1.2 is used for describing the damage process of fatigue crack growth. A well known model which describes fatigue crack growth for rather long cracks was proposed by Paris et al. (1961). It reads

$$\frac{da}{dN} = C(\Delta K)^\eta, \quad (6.40)$$

where  $C$  and  $\eta$  are material parameters.  $a$  is the crack length,  $N$  is the number of cycles and  $\Delta K$  is the stress intensity factor range which can be computed by  $\Delta K = K_{\max} - K_{\min} = K_{\max} = K$ , if  $K_{\min} = 0$  is assumed. In general, the rate of small crack growth can be different to that of long crack growth. However, according to the ASM-Handbook (ASM, 1996), the small crack growth rate can be reasonably approximated by a model for long cracks. Consequently, PARIS' law is also considered here. For Al2024, the material parameters for the PARIS' law are documented in (Pieri & Sinclair, 1994). For two different geometrical scaling factors, two distinct values of  $\eta$ , 2.73 and 3.24, are reported. In what follows, an average value of  $\eta=3.0$  is considered. Regarding the stress intensity factor, it can be computed in terms of the energy release rate (Lemaitre, 1992). More precisely,

$$K = \sqrt{EY} \quad (6.41)$$

For relating PARIS law to the brittle damage model elaborated in the previous subsection, the time derivative of (6.40), evaluated over one cycle, is computed. It gives

$$\dot{a} = \eta C K^{\eta-1} \dot{K}. \quad (6.42)$$

Consequently, by inserting equation (6.41) into (6.42), a relation between the energy release rate and crack growth of the type

$$\dot{a} = \eta C (\sqrt{EY})^{\eta-1} \frac{\sqrt{E}}{2} Y^{-1/2} \dot{Y} = \bar{C} Y^{(\eta/2-1)} \dot{Y}, \quad (6.43)$$

can be derived. Here,  $\bar{C}$  is a material constant. By further assuming  $\dot{D} \sim \dot{a}$ , the proposed brittle damage evolution in (6.31) is defined as

$$\dot{D} \sim Y^{2(N-1)} \dot{Y} . \quad (6.44)$$

Accordingly, a comparison of both models yields the material parameter  $N = 1.25$ . Considering the damage evolution rate (6.31), here the admissible choice  $S_2 = N = 1.25$  is made, although for the given range of  $\eta$  its value can lie between 1.18 - 1.31. For the sake of further simplification and to reduce the unknown material parameters, the variable damage threshold value  $Q_b$  will be neglected in our numerical simulations, i.e., an evolving damage threshold will be modelled by means of the shift tensor  $\Gamma$  only. Summarising the aforementioned assumptions and simplifications yields finally

$$\dot{D}^b = \frac{N\sqrt{Y^b}\dot{Y}^b}{B_\Gamma(\Gamma_\infty) - \Gamma} = \frac{1.25\sqrt{Y^b}\dot{Y}^b}{B_\Gamma(\Gamma_\infty) - \Gamma} . \quad (6.45)$$

Here,  $(\Gamma)_\infty$  denotes the limit value of the brittle damage threshold variable  $(\Gamma)$ , see (6.20).

For computing the constant damage threshold value  $Q_{b0}$  (initial threshold), the endurance limit is considered in general. However, for aluminium a clear endurance limit does not exist. Given that the endurance limit can be set for a number of cycles at fracture  $N_f \sim 10^7 - 10^8$ , the CAUCHY stress lies in the range  $\sigma_f \sim 50 - 75$  MPa. Knowing  $\sigma_f$  and assuming instantaneous damage initiation in the first cycle, i.e.,

$$\phi^b = \frac{Y^{bN}}{N} - Q_{b0} = 0 \quad (6.46)$$

$Q_{b0}$  can be computed from

$$Q_{b0} = \frac{\left(\gamma^b \frac{\sigma_f^2}{2E}\right)^N}{N} . \quad (6.47)$$

Here, a purely elastic material state has been considered. For an average value  $\sigma_f = 62.5$  MPa,  $Q_{b0}$  is computed as 0.0096 (MJ/m<sup>3</sup>) for the DLC-specimen, where  $\gamma^b = 1.0$ ,  $E = 67000.0$  MPa,  $N = 1.25$ . For the flat specimen this value is a little lower  $Q_{b0}=0.0091$  ( $E=70000.0$  MPa, an average value taken for both T and L-direction).

## 6.2.2 The approximation of the elasto-plastic hysteresis curve

To permit a good approximation of the plastic hysteresis curve, three back stress tensors are superposed (see (Chaboche & Lemaitre, 1994), p.234). In



particular, the introduction of a linear kinematic hardening rule (third back stress tensor) improves the description of strain ratcheting, i.e., the growth of permanent strains from cycle to cycle. A single ARMSTRONG-FREDERICK rule usually overpredicts the ratcheting effect. The linear rule defines in particular the slope of the hysteresis curve at the point of strain reversal. The set of

Table 6.1: Optimised material parameters characterising the elasto-plastic response (DLC-specimen,  $\Delta\varepsilon = 0.025$ )

$H_k^{(1)}$ , [MPa]	$H_k^{(2)}$ , [MPa]	$H_k^{(3)}$ , [MPa]	$H_i$ [MPa]	$E$ [MPa]	
180000.0	5000.0	6010.0	1026.496	67000.0	
$B_k^{(1)}$	$B_k^{(2)}$	$B_k^{(3)}$	$B_i$	$Q_0^{\text{eq}}$ [MPa]	$\nu$
3050.0	20.0	0.0	6.8433	225.0	0.3

material parameters defining the plastic response has been found by matching the experimentally obtained and numerically simulated elasto-plastic hysteresis curves for a medium strain range of  $\Delta\varepsilon = 0.025$  with 53 number of cycles to fracture see Table (6.1). In Figure 6.1, the stress-strain diagrams obtained experimentally and those simulated numerically are presented. The approximation is not completely in line with the experimental data, but reproduces the cyclic behaviour quite satisfactory.

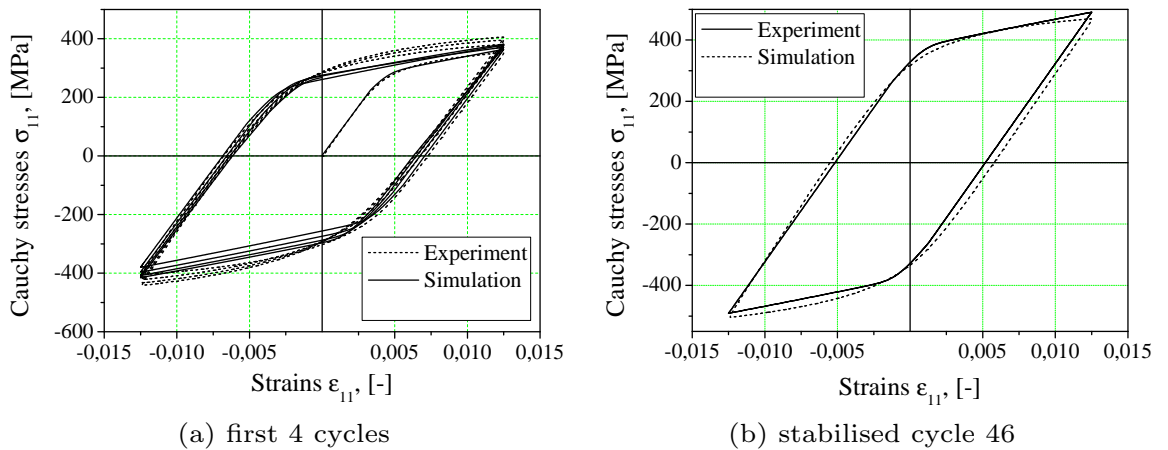


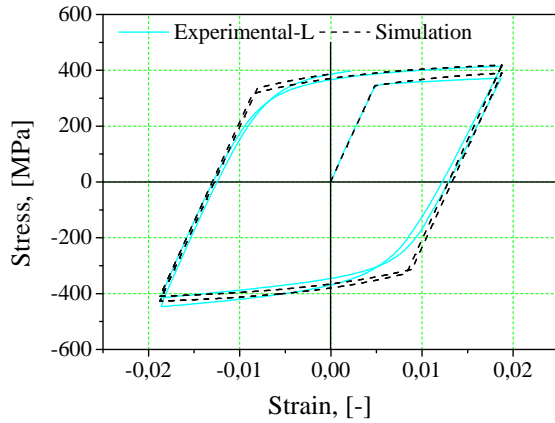
Figure 6.1: Elasto-plastic hysteresis (DLC-specimen, 100 mm plate); experimental data and simulation for a strain range of  $\Delta\varepsilon=0.025$

For the flat specimen the elasto-plastic parameters were adjusted using experimental cyclic stress-strain curves for  $\Delta\varepsilon=0.0375$  for both T and L-direction. Unlike the DLC-specimen, a good comparison with experimental hysteresis

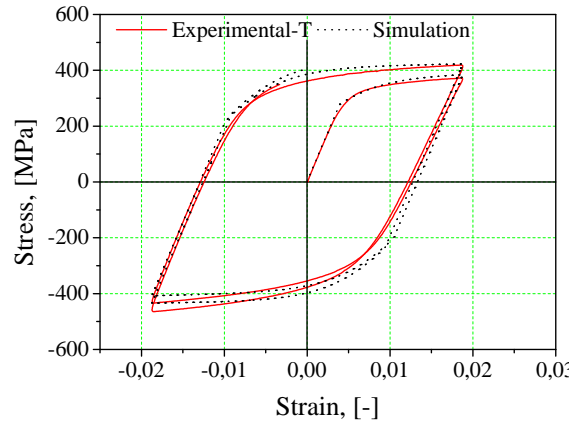
was obtained using a single back stress (Figure 6.2). The respective material parameters are given in Table (6.2).

Table 6.2: Optimised material parameters for elasto-plasticity for Al2024 4 mm sheet, for both L and T-directions

Elasticity			Plasticity				
E [MPa]	$\nu$		$Q_0^{\text{eq}}$	$H_i$ [MPa]	$B_i$	$H_k^{(2)}$	$B_k^{(2)}$
L	71000	0.3	345	501.252	5.01252	3333.33	90.0
T	70000	0.3	280	1050.766	11.0606	16666.66	265.0



(a) L-direction,  $\Delta\varepsilon = 0.0375$ ,  $N_R=48$



(b) T-direction,  $\Delta\varepsilon = 0.0375$ ,  $N_R=35$

Figure 6.2: Comparison of simulation and related experimental data for the initial 2 cycles (flat specimen, 4 mm sheet)

### 6.2.3 The damage initiation phase

Following Section 5.2.2, damage initiation is modelled by (5.16). According to (5.16), the stored energy corresponding to the back stress tensor affects damage initiation as well. However, since the first back stress saturates very fast, while the last back stress would lead to a too large energy (linear hardening), only the second back stress is considered in what follows.

In summary, defining damage initiation requires to determine the set of material parameters  $[A, m, w_D]$ , cf. Lemaitre (2001). In order to determine the set

Table 6.3: Parameters for isotropic hardening, Al2024-T351

Material	Specimen	$R_\infty$	$b$
100 mm plate	DLC	150.0	6.82
4 mm sheet	L flat	100.0	5.0
	T flat	95.0	11.0

of material parameters  $A$ ,  $m$ ,  $w_D$ , the minimisation problem

$$\{A, m, w_D\}^* = \arg \min_{\{A, m, w_D\}} \left( \sum_1^n \text{abs} \left( \log N_{D,i}^{\text{exp}} - \log N_{D,i}^{\text{sim}} \right) \right) \quad (6.48)$$

is again considered. Here,  $N_{D,i}^{\text{exp}}$  are the experimentally observed cycles up to damage initiation and  $N_{D,i}^{\text{sim}}$  are their numerically simulated counterparts.  $n$  is the number of experiments with different strain ranges (see Table (5.3),  $n=5$ , DLC-1 to DLC-5 for DLC-specimen and for flat specimen  $n=4$  corresponding to the selected experiments in T and L-direction respectively; see Table (4.7)). The final material parameters are summarised in Table (6.4).

Table 6.4: Optimised parameters for damage initiation parameters of Al2024-T351

Material	Specimen	$m$	$A$	$w_D(\text{MJ}/\text{m}^3)$
100 mm	DLC	4.8972	0.009824	0.66295
4 mm sheet	L flat	4.964	0.0097	0.7247
	T flat	2.479	0.00106	1.41

#### 6.2.4 The coupled ductile-brittle damage model

Although a ductile damage model similar to that proposed in the previous Section 5.2 has already been calibrated, all material parameters associated with the ductile damage model are re-calibrated here. Accordingly, the set of material parameters defining brittle and ductile damage evolution reads  $[M, S_1, B_\Gamma, H_\Gamma, \gamma^p]$ . A mesoscopic crack is assumed, if the critical values of the damage variables  $\mathcal{D}_{\text{crit}}^{\text{p,d}} = \mathcal{D}_{\text{crit}} = 0.23$  are reached. For the modelling of

crack closure,  $h_a$  is set to  $h_a=0.2$  (see Section 5.2.4, (5.21)). For the brittle damage contribution damage evolves only in the half-cycle sign  $\left(\frac{Y^{bN}-\Gamma}{S_2}\right) > 0$ .

The parameter identification was carried out in three steps. Within each of those the minimisation problem

$$\{\dots\}^* = \operatorname{argmin}_{\{\dots\}} \left( \sum_1^n \operatorname{abs} \left( \log N_{R,i}^{\operatorname{exp}} - \log N_{R,i}^{\operatorname{sim}} \right) \right) \quad (6.49)$$

was considered ( $n=5$  (DLC) and  $n=4$  (flat)), see (6.48). At first, the ductile damage model was calibrated (for finding  $M$  and  $S_1$ ). Subsequently, the same procedure was applied to the determination of the brittle damage parameters  $B_\Gamma$  and  $H_\Gamma$ . Finally, a fully coupled analysis yielded the composition factor  $\gamma^p$ . The final material parameters are presented in Table (6.5).

Table 6.5: Damage parameters of Al2024-T351 for the combined ductile-brittle damage model law

Material	Specimen	$M$	$S_1$	$B_\Gamma$	$H_\Gamma$	$\gamma^p$
100 mm	DLC	1.6	1.544	0.992	121.5	0.86
4 mm sheet	L flat	1.0511	2.12717	0.0515	200.51	0.55
	T flat	0.9475	2.0797	0.115	43.39	0.55

## 6.3 Numerical examples

### 6.3.1 Smooth round bar (DLC-specimen)

The prediction capability of the novel ductile-brittle damage model is demonstrated here by re-analysing a smooth round bar (DLC), see Table (5.3), with the parameters identified in Section 6.2. Its middle-section has been discretised by the finite element mesh shown in Figure 6.3. Due to symmetry, only one quarter of the structure has been discretised. The specimen's dimensions have been given previously in detail in Figure 4.4(a). The computation was done displacement-controlled. The right boundary at the free end is slightly conical to force localisation at the bottom right corner of the structure. The fully three-dimensional CDM model as presented in Section 6.2.4 has been implemented into a UMAT-routine in ABAQUS. To improve the convergence of

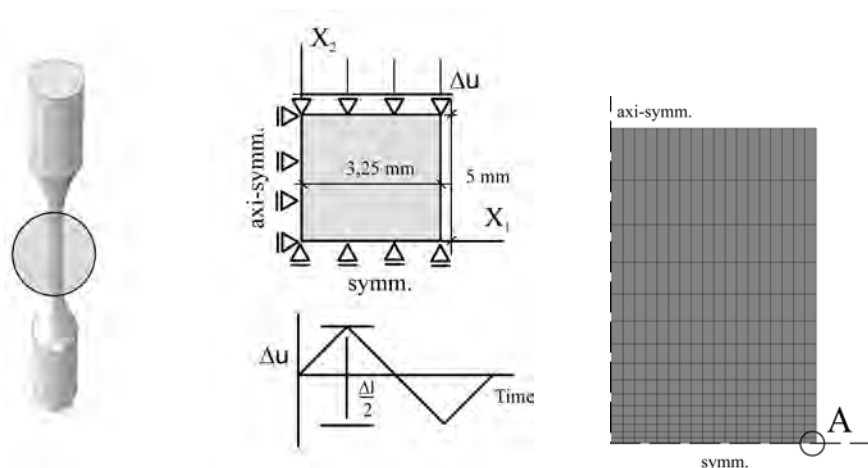


Figure 6.3: Sketch of the DLC-specimen extracted from S-direction of the 100 mm plate (see Figure 4.4(a)), loading conditions and finite element discretisation

the NEWTON iteration scheme at the material point level, a line search according to (Pèrez-Foguet & Armero, 2002) has been applied. The same technique was also employed at the global level (equilibrium iteration).

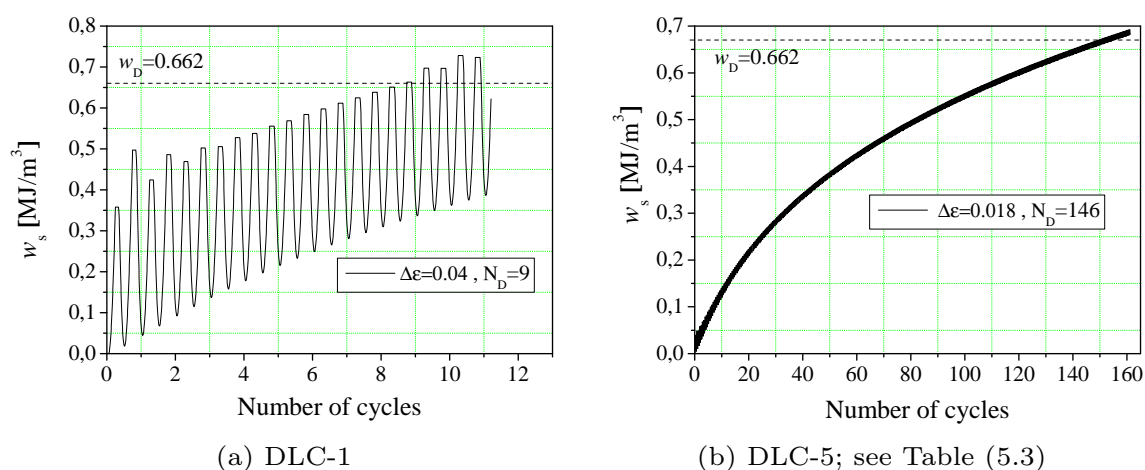


Figure 6.4: Damage activation criterion for two different strain amplitudes (DLC-specimen) at point A

The results are presented in Table (6.6) where also the estimated number of cycles for the one-dimensional case (as optimised during the parameter identification) are included. As can be seen, the numerical results for the one-dimensional and the three-dimensional case are nearly identical. Only for DLC-1, the fully three-dimensional computation gives a slightly better prediction for  $N_R^{\text{sim}}$ . Accordingly, the use of the fully coupled ductile-brittle

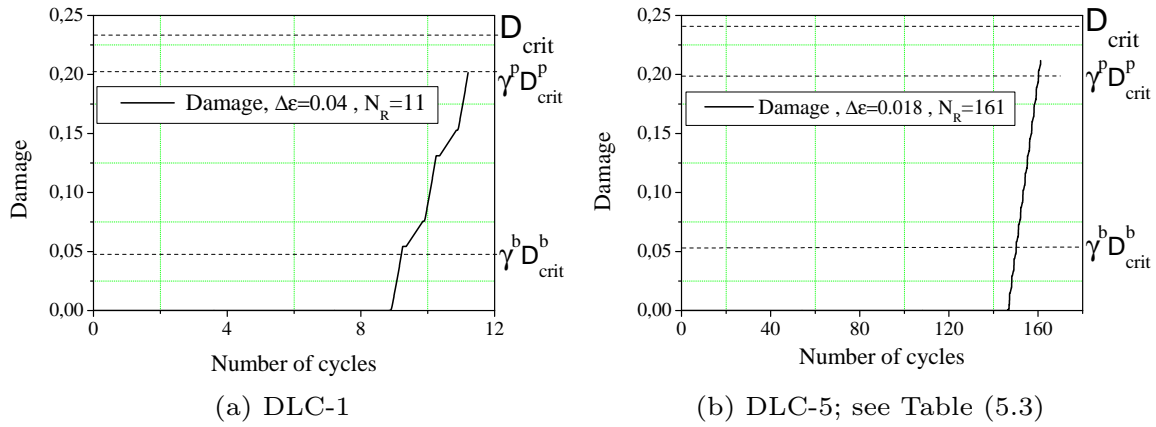


Figure 6.5: Evolution of the damage variable  $\mathcal{D} = \mathcal{D}^p + \mathcal{D}^b$  for two different strain amplitudes (DLC-specimen) at point A

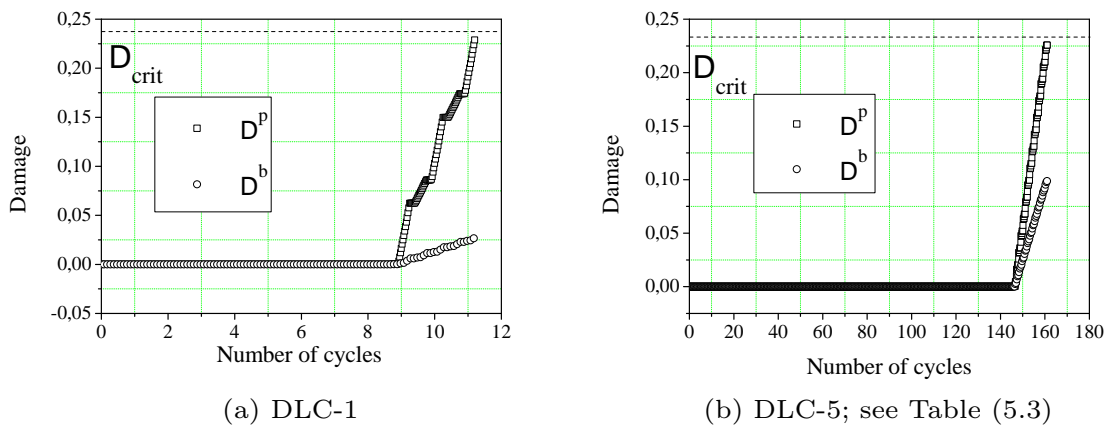


Figure 6.6: Ductile and brittle damage variables for two different strain amplitudes (DLC-specimen) at point A

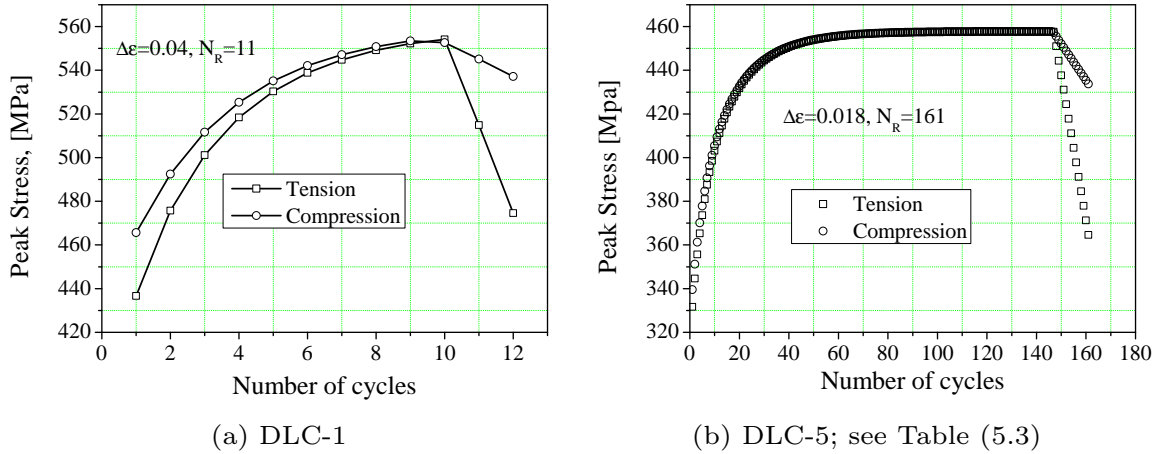


Figure 6.7: Maximum CAUCHY stresses for two different strain amplitudes (DLC-specimen) at point A

damage model leads to a prediction of lifetimes in good agreement with those experimentally observed. A more careful analysis reveals that the numerical simulation could be further improved by modifying the damage activation criterion (compare  $N_D^{\text{sim}}$  to Table (5.3)), since an error in  $N_D^{\text{sim}}$  affects also the prediction for  $N_R^{\text{sim}}$ . According to Figure 6.4, the portion of the plastic strain energy related to kinematic hardening plays a much greater role for DLC-1, in comparison to DLC-5 where the cyclic portion of the  $w_s$ -curve is negligible. In Figure 6.5 and 6.6, the total damage accumulation as well

Table 6.6: Numerically simulated number of cycle  $N_D^{\text{sim}}$ ,  $N_R^{\text{sim}}$  (4.1) and error with respect to  $N_R^{\text{exp}}$  ("DLC-X" abbreviation according to Table 5.3).

Type	1-D		3-D	
	$N_D^{\text{sim}}$	$N_R^{\text{sim}}$ [%]	$N_D^{\text{sim}}$	$N_R^{\text{sim}}$ [%]
DLC-1	9.25	12.11/+21.1	8.7	11.2/+12
DLC-2	29.75	34.06/+13.5	29.27	33.7/+12.3
DLC-3	52.25	58.25/+9.9	52.2	59.0/+11.3
DLC-4	101.25	112.04/+18.8	101.7	113.0/+18.1
DLC-5	144.25	159.13/+4.1	145.7	161.0/+3.0

as its defining single parts are plotted. As evident, the brittle damage part plays only a minor role for DLC-1, while its effect is more pronounced for DLC-5. This would imply that small fatigue crack growth is more relevant

for large numbers of cycles, especially for HCF. Furthermore, as can be seen in Figure 6.5 and 6.6, the fracture criterion for  $D^P$  is reached first, while the complete damage variable is still below its threshold. By comparing the numerical results to the experimental observations, it can be concluded that the brittle damage part is slightly underestimated for a smaller number of cycles. To increase its influence, different modifications are possible. The probably most promising one, which will be considered in future, is a variable composition factor.

The peak stress as a function of the number of loading cycles is shown in Figure 6.7. As can be observed, the maximum stresses in tension are smaller than in compression. This effect, which can also be observed in the experiment, is a direct consequence of the crack closure effect.

A summary of the results obtained using the ductile damage model and the novel coupled quasi-brittle ductile damage model is given in Figure 6.8. Accordingly, the novel model predicts a more realistic mechanical response.

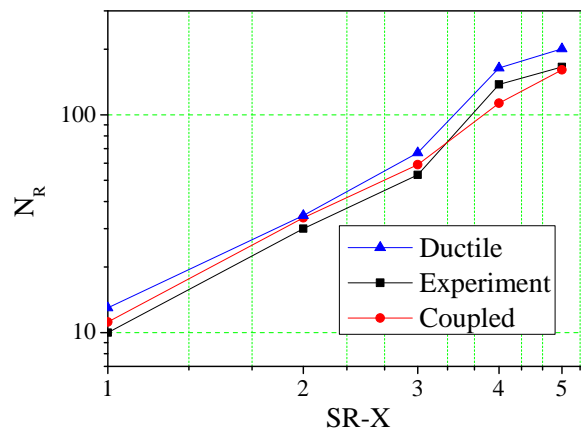


Figure 6.8: Predictions of the ductile and the coupled model for DLC-specimens (S-direction, 100 mm plate), see Table (5.3)

### 6.3.2 Flat specimen

For the finite element simulations of the flat specimens, a three-dimensional model representing a quarter of the specimen's gauge section is considered imposing a two-fold symmetry condition ( $X_1$  and  $X_2$ ). Despite the fact that the specimen's thickness is comparably small, the simulations are done using a three-dimensional discretisation. A coarse mesh is used with mesh refinement



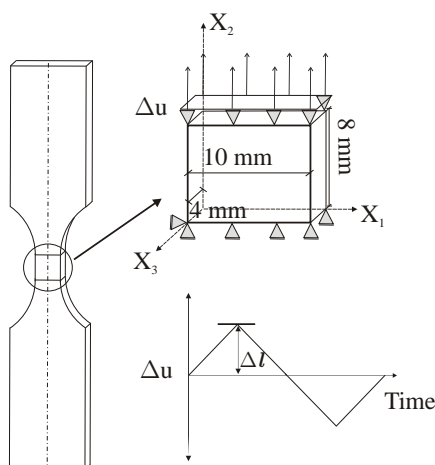


Figure 6.9: Sketch of the flat specimen (4 mm sheet) and the loading conditions used in the finite element simulations

at the expected regions of stress concentration which allows a good simulation of necking and the constraints caused by damage localisation. Tri-linear finite elements (3D bricks with 8 nodes) are used in the discretisation. The triangulation consists of eight elements across the thickness. A typical dimension of a finite element is 0.2 mm in longitudinal and transversal and 0.5 mm in thickness direction. The specimens are loaded under displacement control with a prescribed linear amplitude function for cyclic loading (Figure 6.9). The specimens are meshed with a geometrical imperfection; a slight hourglass shape is used to concentrate strain and therefore damage at the middle section.

Within the computations, the calibrated material parameters summarised in Table (6.4) are used. The numerically predicted lifetimes are given in Table (6.7). For sake of comparison, the purely ductile damage model in the spirit of Lemaitre & Desmorat (2005) is also considered, see Section 5.2.3. Since both models are equivalent before damage accumulation, only the numbers of cycles within the softening regime ( $N_E^{\text{sim}}$ ) are given. According to Table (6.7), a purely ductile damage model leads to a significant overestimation of the lifetime. By way of contrast, the fully coupled ductile-brittle approach captures the underlying physical processes in a more realistic manner and thus, leads to better agreements with the experiments.

## 6.4 Conclusions

In the present chapter, a coupled isotropic ductile brittle damage model suitable for the numerical analysis of LCF in high-strength aluminium alloys has been proposed. Comparisons between the predictions computed by the novel

Table 6.7: The lifetime prediction (quasi-brittle ductile model) compared to experiments in the LCF regime (for both L and T-directions, 4 mm sheet).  $N_E^{\text{exp}}$  is the number of loading cycles during the softening regime

Orientation	$\Delta\varepsilon$ [%]	Number of cycles		
		Experiment	Simulation - $N_E^{\text{sim}}$	
		$N_E^{\text{exp}}$	ductile	coupled
L	3.75	4	12.0	10.0
	3.5	8	11.26	9.62
	3.0	8	13.59	10.5
	2.75	10	17.755	11.0
T	3.25	5	7.0	6.0
	3.0	6	17.22	16.0
	2.5	7	23.40	20.45
	2.375	9	25.82	21.48

model and experiments for flat specimens showed a very good agreement. In particular, the estimated lifetimes are more realistic than those based on a purely ductile damage model. That confirmed the quasi-brittle nature of damage accumulation in Al2024.

## 7 Damage tolerance assessment of stiffened panels

The applicability of the novel constitutive model elaborated in Chapter 6 to complex engineering structures is demonstrated here. As a prototype structure, a certain bonded stringer-skin assembly is considered. The present chapter is completed by discussing current concepts of damage tolerance in aircraft design.

### 7.1 Adhesively bonded stiffened panels

The whole visible part of an aeroplane is constituted of stiffened panels (Figure 7.1), i.e. an outer thin sheet (skin) with generally orthogonally arranged integral or fastened stiffeners (stringers and frames in the fuselage shell sketched in the Figure 7.1). The fastened stiffeners can be riveted, adhesive bonded or welded to the skin (Niu, 1999).

These aeronautical stiffened panels are prone to the in-service formation of damage. An example for the final stage of damage represented by a through-the-skin crack is sketched in Figure 7.2. In the past, different designers have made different assumptions about the initial damage. Today, a crack extending into two frame bays with the central frame also cut is generally assumed. This through-the-skin crack can propagate along the fuselage shell and if it is not detected before becoming unstable (at the critical crack length) it can cause a catastrophic failure.

For this reason, the maximum undetectable crack length [ $a_{det}$ ] must be long enough to permit the establishment of a practicable inspection plan capable of detecting the crack before it reaches its critical crack length [ $a_{cr}$ ], during the operative life of the aircraft. Figure 7.3 shows the general crack growth behaviour of a skin crack propagating through a stiffened panel over a broken stringer.

Stiffened panels with adhesively bonded stiffeners can provide significant benefits in comparison with the more conventional riveted and monolithic structures, as it is evident in Figure 7.4. This is related to the long crack prop-

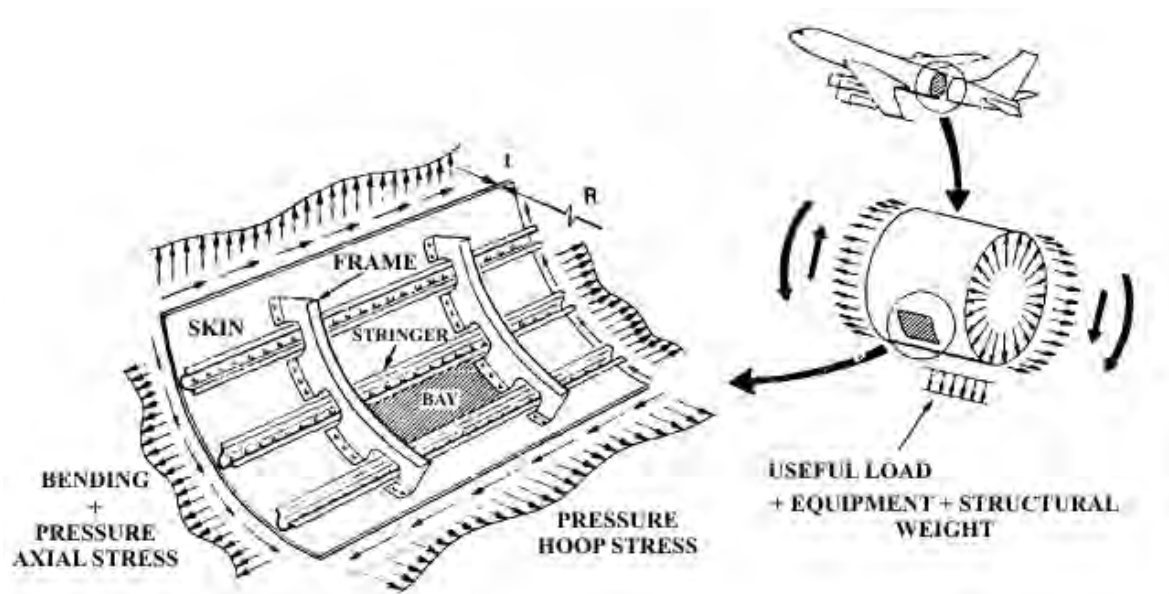


Figure 7.1: Fuselage stiffened panel: configuration and loading condition (FAA, 1993)

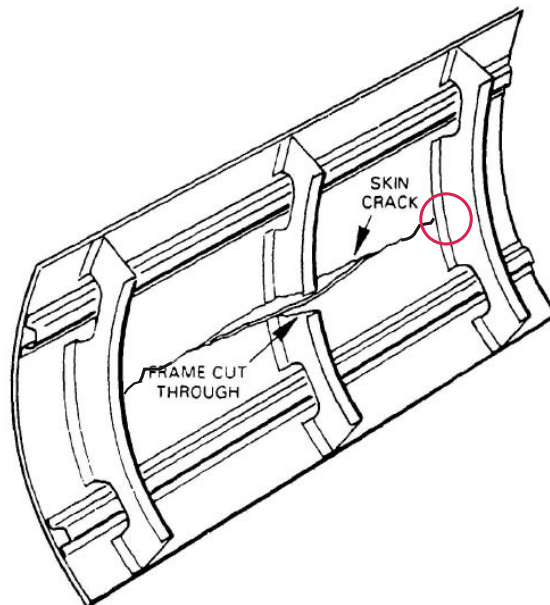


Figure 7.2: Fuselage stiffened panel with a longitudinal skin crack over a broken frame (FAA, 1993)

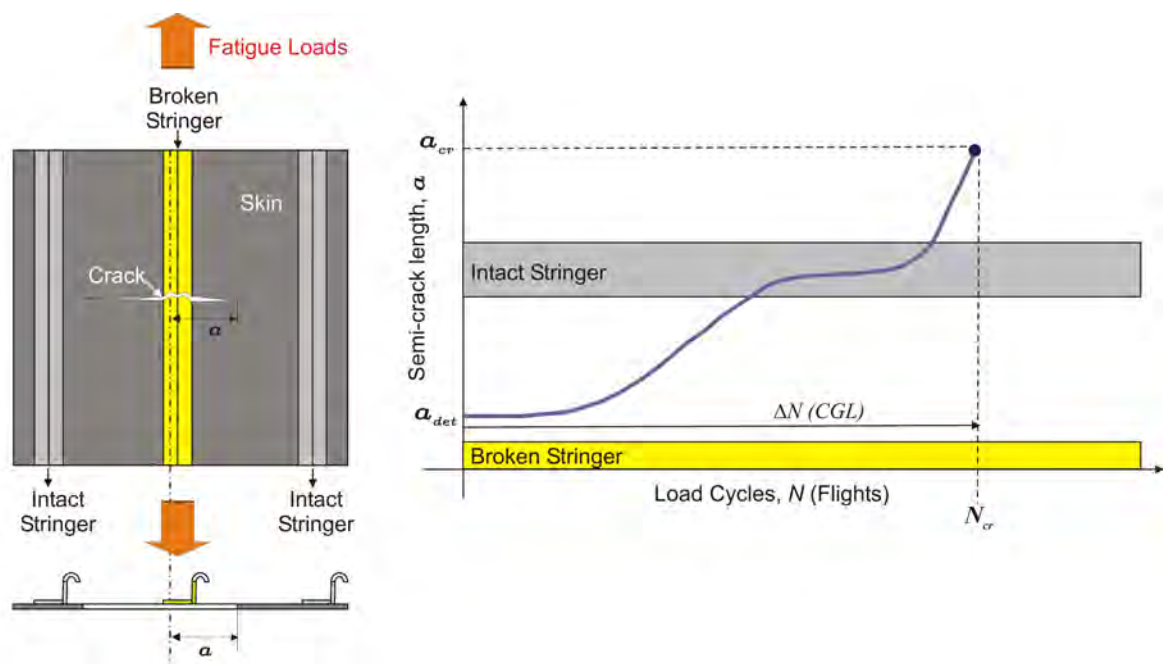


Figure 7.3: General crack growth behaviour of a skin crack propagating through a stiffened panel over a broken stringer

agation period through the skin underneath the bonded stringers (under the intact stringer in Figure 7.4). However, this has not been fully understood yet, cf. (Schmidt, 2005).

Although many details concerning the failure of bonded stringer-skin connections are still unknowns, it has been observed that the failure mechanism can also occur by means of a low-cycle-fatigue (LCF) mechanism (Meneghin, 2010). This is due to the intensive cyclic stress induced in the stringer which bridges the skin crack, mostly exerted in the narrow area of the stringer over the crack. The recorded maximum stresses induced in the stringers are often close to the Ultimate Tensile Strength (UTS) of the stringer material and they usually act for a few hundred load cycles before the stringer eventually fails.

## 7.2 Application of the coupled ductile-brittle damage to the numerical analysis of the stringer-skin connection

The design of such structural components such as a stringer-skin connection requires the estimation of their lifetimes. Figure 7.5(a) and Figure 7.6 show the dimensions of the considered structure. In the past, different, mostly ad-hoc, concepts have been considered for that purpose. Since it was experimentally

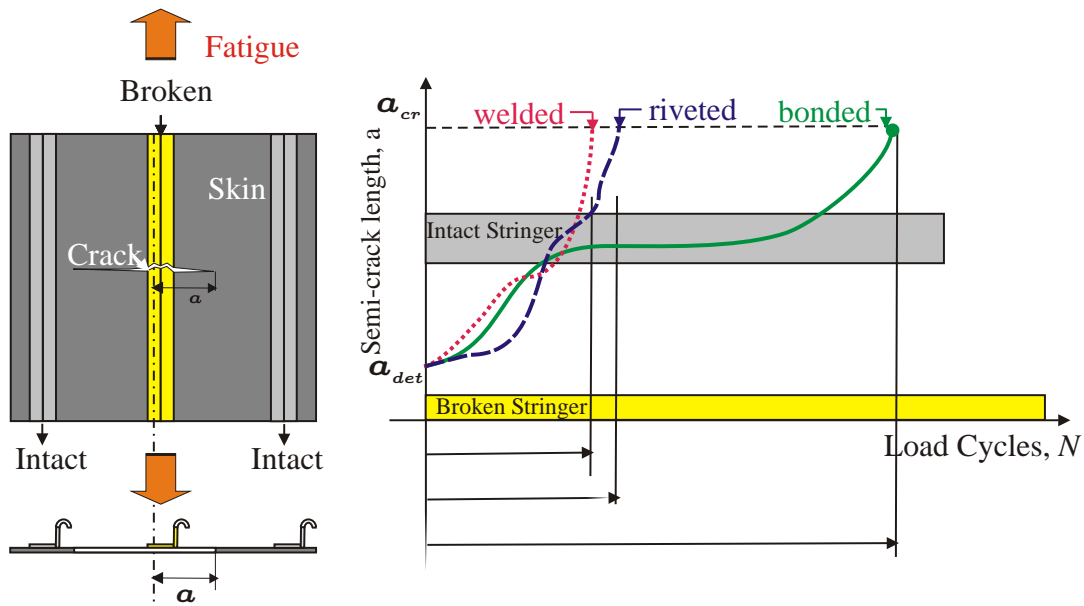


Figure 7.4: Beneficial effect of the bonded stiffened panels in comparison with riveted and monolithic solutions Meneghin (2010)

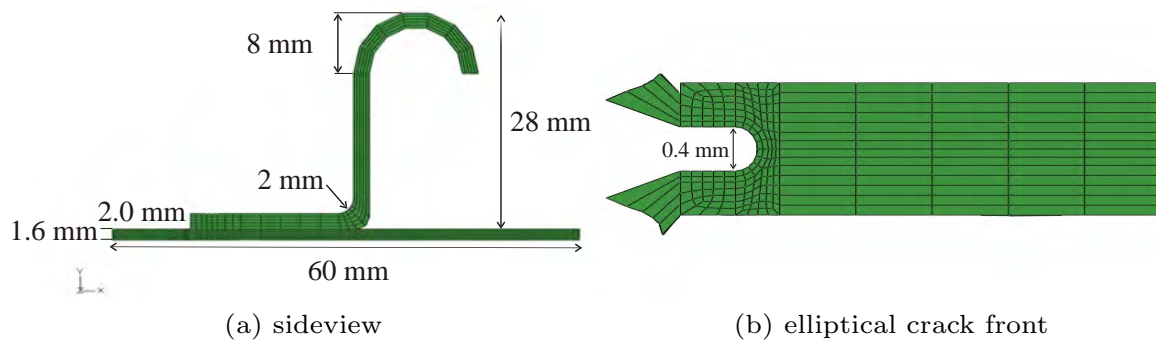


Figure 7.5: The dimensions of the skin-stringer assembly

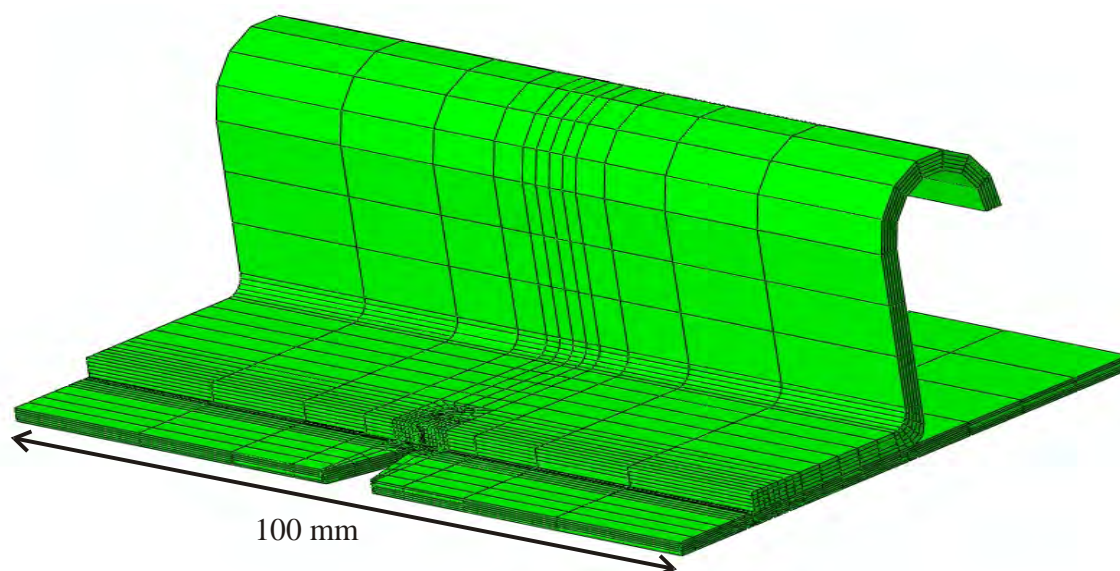


Figure 7.6: The complete skin-stringer assembly with elliptical pre-crack

observed that the stringer failure is driven by a low-cycle fatigue mechanism (Meneghin, 2010), the lifetime can be naturally estimated by using the constitutive model described in the previous chapter (Section 6.2.4).

Although the stringer is bonded to the skin, the whole assembly is considered as homogeneous and no special contact conditions have been defined within the respective finite element simulations. Despite the fact that a bonded stringer-skin assembly performs better with regard to damage tolerance, the purpose of this simulation was not to evaluate/judge the bonding strength. In industrial practise and at the laboratory testing stage only through-the-thickness cracks are used, i.e., the crack front is always considered straight. To model such a situation, an elliptical through-the-thickness notch is taken here as pre-crack ahead of the stringer, see Figure 7.5(b). The assumption of such a blunt notch reducing stress singularities is very practical from a modelling point of view. Otherwise damage would already evolve from the beginning. Furthermore, it is important to note that the numerical analyses were not intended to obtain the crack propagation profile. More explicitly, focus was on damage initiation (propagation of micro-cracks).

The structure shown in Figure 7.7 has been cyclically loaded displacement controlled under symmetric load condition ( $R = -1$ ). A very fine mesh especially around the elliptical notch has been generated. With one exception, the material parameters given in Table (6.5) (4 mm sheet, L-direction) have been used for the numerical analysis. This exception is the plastic energy threshold ( $w_D$ ) which has been altered to a value of 1.62. This value has been taken

from the uni-axial simulations (L-direction). The results of the finite element simulation are shown in Figure 7.7. The coupled damage model predicts microcrack initiation in the assembly after 60 load cycles. Subsequently, damage evolves fast to the critical value.

### **7.3 Conclusions**

As an outlook and for demonstrating the robustness and efficiency of the coupled ductile-brittle damage model proposed in Section 6.2.4, a complex engineering problem was analysed. More precisely, damage initiation in a stringer-skin connection of a fuselage was considered. While in the past, different, mostly ad-hoc, concepts have been considered for designing such structures to reach a desired lifetime, the combination of careful material characterisation (Chapter 4) and physically sound modelling as discussed in the present chapter allows to put this design process on more solid grounds.



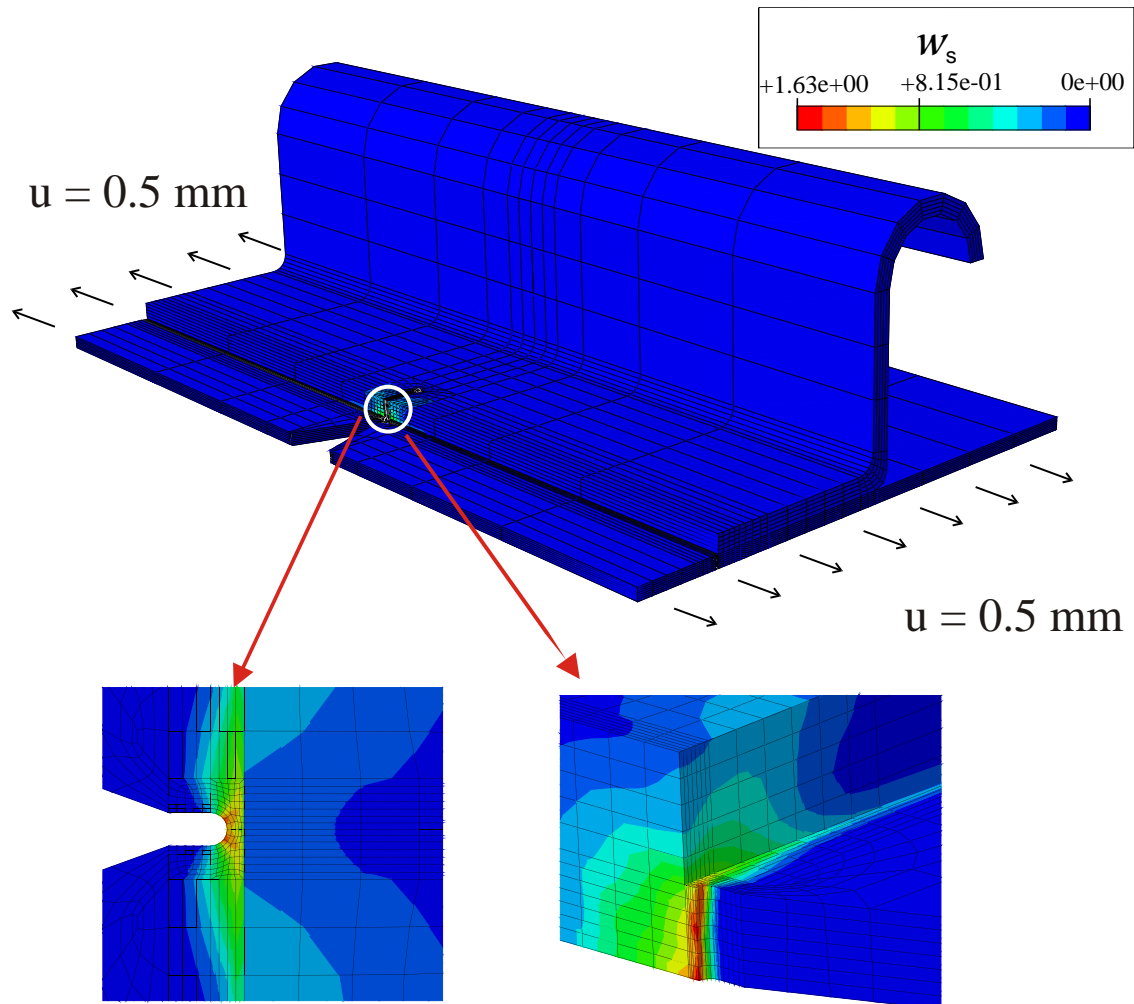


Figure 7.7: Distribution of the stored plastic energy  $w_s$  driving damage initiation, see (6.48). Lower left hand side: crack front at the elliptical notch (top view); lower right hand side: profile of plastic stored energy (side view). The relative position of the analysed stringer-skin connection within the fuselage section is marked by the circle in Figure 7.2



## 8 Summary and Conclusions

Many research groups around the globe take a direct route from failure under monotonic loading to high cycle fatigue. Surprisingly, low cycle fatigue being a border phenomenon between the aforementioned failure phenomena, is often not considered. In the present thesis, the gap between failure under monotonic loading and HCF was closed by thorough LCF analyses. As a practically relevant material, the high-strength aluminium alloy Al2024 has been chosen.

The SR $\mu$ CT investigations have made it evident that micro-mechanics based porous plasticity damage models are not suitable for this particular alloy due to a high number of dense particles. The particles are arranged in continuous layers throughout the micro-structure. Studying the microstructure and fracture mechanisms, it can be safely stated that bigger inclusions in Al2024 sheets and plates are responsible for damage initiation in the LCF regime. Al2024 thick plate, due to its underlying manufacturing process develops precipitates in the middle of the plate, creating layers within. A transition of fracture mode, from surface to internal fracture, was observed with increasing plastic range in cyclic experiments. In an ordinary low cycle regime (40-200 cycles), a fatal crack is generated by the propagation and frequent coalescence of small surface cracks. Eventually, a mesocrack initiates from the surface of the specimen due to the presence of bigger intermetallics.

For a 100 mm thick plate the S-direction has been found to be very brittle when compared to L and T-directions (rolling directions) respectively. Although there is a ductility observed, the resulting failure occurs without macroscopic softening. An identical response was also observed in 4 mm thin sheets. For allowing symmetric strain amplitudes ( $R = -1$ ) in such sheets, a floating anti-buckling guide has been proposed which successfully prevents buckling at high compressive loading without affecting adversely the mechanical behaviour of the specimen. In summary, the material behaviour in S-direction can be characterised as neither completely brittle nor completely ductile. More precisely, plastic strain accumulation as damage driving process as well as small fatigue crack growth as brittle damage mechanism can be seen for LCF. This led to a conclusion that for modelling low cycle fatigue for these materials, a material model which incorporates both these effects (coupled ductile and brittle) was required.

For that purpose, a phenomenological CDM approach was considered in the present thesis. In our earlier analyses in the past, only ductile damage was taken into account. However, since the microstructural arrangement of A12024, as observed in our experiments favour also brittle failure modes, a fully coupled ductile-brittle model has been proposed. While ductile damage has been modelled in a similar fashion as advocated formerly by other authors (see, e.g. Lemaitre & Desmorat (2005)), a novel approach was elaborated for brittle damage. In sharp contrast to the ductile damage model, material degradation can already evolve below the yield limit. Since early work on a large number of smooth and notched specimen demonstrated that wide variations in commercial aluminium alloys caused little or no detectable differences in fatigue strength, the novel coupled damage model is also applicable to a wider range of aluminium alloys. The material parameters necessary to use the proposed model can be easily obtained from a hysteresis loop test in order to determine the cyclic stress-strain curve. The predicted LCF lifetimes for A12024 alloy are in good agreement the respect experiments verifying the underlying assumptions.

## Bibliography

- ALCOA<sup>®</sup> (1995): *Material Specification*, URL [http://www.alcoa.com/mill\\_products/catalog/pdf/alloy2024techsheet.pdf](http://www.alcoa.com/mill_products/catalog/pdf/alloy2024techsheet.pdf).
- ASM (1996): *Fatigue and Fracture*, Technical report, ASM Handbook vol.19, ASM: Materials Park, 1996.
- ASTM (1998): "*Standard recommended practice for constant-amplitude low-cycle fatigue testing*", *ASTM E606-80*, ASTM 1998.
- BECKMANN, F., DONATH, T., FISCHER, T., DOSE, J., LIPPMANN, T., LOTTERMOSER, L. ., MARTINS, R. & SCHREYER, A. (2006): *New developments for synchrotron-radiation-based microtomography at DESY*, Technical report, DESY (Proc SPIE 6318:631810-631811), 2006.
- BERNHARDT, R., MÜLLER, B., THERUNER, P., SCHLIEPHAKE, H., WYSS, P., BECKMANN, F., GOEBBELS, J. & WORCH., H. (2004): *Comparison of microfocus- and synchrotron x-ray tomography for the analysis of osteointegration around Ti6Al4V- implants.*, in: *European Cells and Materials*, Volume 7, 42.
- BESSON, J., STEGLICH, D. & BROCKS, W. (2003): *Modeling of plane strain ductile rupture*, in: *Int. J. Plast.*, Volume 19, 1517–1541.
- BISWAS, K. (1993): *Problems and Feasibilities of Testing the Cyclic Behavior of Thin Sheet Steels.*, in: *Steel Research*, Volume 64(8-9), 407–413.
- BONORA, N., GENTILE, D., PIRONDI, A. & NEWAZ, G. (2005): *Ductile damage evolution under triaxial state of stress, theory and experiments*, in: *International Journal of Plasticity*, Volume 21, 981–1007.
- BOWLES, C. & SCHIJVE, J. (1973): *Role of inclusions in fatigue crack initiation in an Aluminum alloy*, in: *International Journal of Fracture*, Volume 9, 171–79.
- BRAITHWAITE, F. (1854): *On the fatigue and consequent fracture of metals*, in: *Institution of Civil Engineers, Minutes of Proceedings*, London 1854, Volume XIII, pp. 463–474.

- BRAUN, R., STEGLICH, D. & BECKMANN, F. (2006): *Damage mechanism and LCF crack extension in Al2024*, Technical report, DESY Annual Report, 2006.
- BROCKS, W. & HEERENS, J. (2002): *Mechanische Modellierung des Verformungs- und Bruchverhaltens hochfester Al-Legierungen*, in: Arbeitsberichts für 2000, 2001, 2002, Technische Universität Hamburg-Harburg, , 98–124.
- CAMBRÉSY, P. (2006): *Damage and fracture mechanisms investigations of an aluminium laser beam weld 2006*, Dissertation, Technischen Universität Hamburg-Harburg.
- CHABOCHE, J. (1988): *Continuum damage mechanics : Part I: General concepts, Part II: Damage growth, crack initiation, and crack growth*, in: J. Appli. Mech., Volume 55, 59–71.
- CHABOCHE, J.-L. & LEMAITRE, J. (1994): *Mechanics of solid materials*, Cambridge University Press 1994.
- COFFIN, L. (1954): *A study of the effect of cyclic thermal stresses on a ductile metal*, in: Trans. ASME, Volume 76, 931–950.
- DAVIS, J. R. (1993): *Aluminum and aluminum alloys*, ASM International. Handbook Committee 1993.
- DUFAILY, J. & LEMAITRE, J. (1995): *Modeling very low cycle fatigue*, in: International Journal of Damage Mechanics, Volume 4, 153–170.
- FAA, T. C. (1993): *Damage Tolerance Assessment Handbook Volume I: Introduction Fracture Mechanics Fatigue Crack Propagation*, Technical report, U.S. Department of Transportation - Federal Aviation Administration, 1993.
- FREDRIKSSON, K., MELANDER, A. & HEDMAN, M. (1988): *Influence of Pre-straining and Aging on Fatigue Properties of High-Strength Sheet Steels.*, in: International Journal of Fatigue, Volume 10(3), 139–151.
- GARRETT, G. & KNOTT, J. (1978): *The influence of compositional and microstructural variations on the mechanisms of static fracture in aluminium alloys*, in: Metall Trans., Volume 9A, 1187–201.
- GRAFF, S.: *FE-Simulation of damage evolution in cyclic plasticity*, Master's Thesis, Christian-Albrecht-Universität zu Kiel, 2003.
- GRAMMENOUDIS, P., RECKWERTH, D. & TSAKMARKIS, C. (2009): *Continuum damage models based on energy equivalence: part I- isotropic material responce*, in: Int J. Damage Mech., Volume 18(1), 31–64.

- GURSON, A. (1977): *Continuum theory of ductile rupture by void nucleation and growth: Part I - Yield criteria and flow rules for porous ductile media*, in: *Journal of Engineering Materials and Technology*, Volume 99, 2–15.
- HAIBACH, E. & LEHRKE, H. (1976): *Das Verfahren der Amplitudentransformation zur Lebensdauerberechnung bei Schwingbeanspruchung*, in: *Archiv für Eisenhüttenwesen*, Volume 74(10), 623–638.
- KACHANOV, L. (1958): *Time of the rupture process under creep conditions*, in: *Izv. AN SSSR, Otd. Tekh. Nauk.*, Volume 8, 26–31.
- KAK, A. & SLANEY, M. (1988): *Principles of Computerized Tomographic Imaging*, IEEE Press, New York 1988.
- KHAN, S., VYSHNEVSKYY, A. & MOSLER, J. (2010): *Low cycle lifetime assessment of Al2024 alloy*, in: *Int. J. Fatigue*, Volume 32, 1270–1277.
- KLIMAN, V. & BILY, M. (1984): *Hysteresis Energy of Cyclic Loading*, in: *Materials Science and Engineering*, Volume 68(1), 11–18.
- LASSANCE, D., FABRÈGUE, D., DELANNAY, F. & PARDOEN, T. (2007): *Micromechanics of room and high temperature fracture in 6xxx Al alloys*, in: *Prog Mater Sci*, Volume 52, 62–129.
- LEMAITRE, J. (1992): *A course on damage mechanics*, Springer, Berlin 1992.
- LEMAITRE, J. (2001): *Petite histoire de l'experimentation en mecanique des solides*, in: *Meccania*, Volume 36, 13–51.
- LEMAITRE, J. & CHABOCHE, J.-L. (1990): *Mechanics of solid materials*, Cambridge University Press, New York 1990.
- LEMAITRE, J. & DESMORAT, R. (2005): *Engineering Damage Mechanics*, Springer, Heidelberg 2005.
- LINDLEY, T. (1986): *Proc. Fatigue Crack Growth*, Pergamon 1986, Volume 53, Metallurgical Aspects of Fatigue Crack Growth, pp. 10–20.
- LUKAS, P. (1996): *Fatigue Crack Nucleation and Microstructure*, ASM International Handbook 1996, Volume 19, Fatigue and Fracture.
- LUKAS, P. & KLESNIL, M. (1973): *Cyclic stress-strain response and fatigue life of metals in low amplitude region*, in: *Mat. Sci. Eng.*, Volume 11, 345.
- MAN, J., OBRITILK, K. & POLAK, J. (2003): *Study of surface relief evolution in fatigued 316L austenitic stainless steel by AFM*, in: *Materials Science and Engineering a-Structural Materials Properties Microstructure and Processing*, Volume 351(1-2), 123–132.

- MANSON, S. (1953): *Behavior of materials under conditions of thermal stress*, in: Heat Transfer Symposium, University of Michigan Engineering Research Institute, , 9–71.
- MCCLINTOCK, F. (1968): *A criterion for ductile fracture by the growth of holes*, in: J. Appl. Mech.-Trans. ASME, , 363–371.
- MENEGHIN, I. (2010): *Damage Tolerance assessment of stiffened panels:*, Technical report, University of Bologna, 2010.
- MEX-ALICONA<sup>®</sup> (2010): *I. Alicona, Mex-Alicona<sup>®</sup> Imaging Solutions. Graz-Austria, 2000-2009.*
- MILAN, M. T., SPINELLI, D. & BOSE, W. (1988): *Fatigue and monotonic properties of an interstitial free steel sheet (FMPIF)*, in: International Journal of Fatigue, Volume 10(3), 139–151.
- MÜLLER, B., PFRUNDER, F., CHIOCCA, L., RUSE, N. & BECKMANN, F. (2006): *Visualising complex morphology of fatigue cracks in voxel based 3D datasets*, in: Materials Science and Technology, Volume 22, 1038–1044.
- MORGENEYER, T., STARINK, M. & SINCLAIR, I. (2008): *Evolution of voids during ductile crack propagation in an aluminium alloy sheet toughness test studied by synchrotron radiation computed tomography.*, in: Acta Materialia, Volume 56, 1671.
- MURAKAMI, S. & OHNO, N. (1981): *A continuum theory of creep and creep damage*, Springer, Berlin 1981, Creep in Structures, pp. 442–444.
- NEEDLEMAN, A. & RICE, J. (1978): *Mechanics of Sheet Metal Forming*, Plenum Press 1978.
- NEEDLER, J. & MEAD, R. (1965): *A simplex method for function minimization*, in: Computer Journal, Volume 7, 308–13.
- NIU, M. (1999): *Airframe structural design*, Hong Kong Conmilit Press Ltd., Hong Kong 1999.
- OTIN, S. (2007): *Lois d’endommagement incrementales isotrope/anisotropies pour applications thermomecaniques complexes 2007*, Dissertation, Cachan: Thèse d’état de l’école normale supérieure de Cachan.
- PAGANELLI, D.: *Comparison of different ductile failure models for Al2024-T351*, Master’s Thesis, Bologna University, 2005.
- PARDOEN, T. & PINEAU, A. (2007): *Comprehensive structural integrity encyclopedia, 2*, Elsevier, Amsterdam 2007, 6.



- PARIS, P., GOMEZ, M. & ANDERSON, W. (1961): *A rational analytic theory of fatigue*, in: *Trend Engineering*, Volume 13, 9–14.
- PIERI, R. & SINCLAIR, G. (1994): *On the effects of scaling on the PARIS law*, in: *Int. J. of Fract.*, Volume 68, 3–8.
- PINEAU, A. (2010): *Fatigue of materials and structures*, wiley 2010.
- PIRONDI, A., BONORA, N., STEGLICH, D. & BROCKS, W. (2006): *Simulation of failure under cyclic plastic loading by damage models*, in: *Int. J. Plast.*, Volume 22, 2146–2170.
- PISARENKO, G. & NAUMENKO, V. (1982): *Experimental methods of the fracture mechanics of materials*, in: *Fiz. -Khim. Mekh. Mater.*, Volume 2, 28–41.
- POLÁK, J. (1991): *Cyclic plasticity and low cycle fatigue life of metals.*, Elsevier Science Publishers 1991.
- PÈREZ-FOGUET, A. & ARMERO, F. (2002): *On the formulation of closest point projection algorithms in elasto-plasticity-part II : globally convergent schemes*, in: *Int J. Numerical Methods in Engineering*, Volume 17, 331–74.
- PROUDHON, H., BUFFIERE, J. & FOUVRY, S. (2007): *Three-dimensional study of a fretting crack using synchrotron X-ray micro-tomography*, in: *Engineering Fracture Mechanics*, Volume 74, 782.
- QUAN, G. (2001): *Microstructure analysis os thick rolled plate Al2024-T351*, Technical report, Institut für Werkstofforschung, GKSS-Internal report, 2001.
- QUAN, G., HEERENS, J. & BROCKS, W. (2004): *Distirbution characteristics of constituent particles in thick plates of 2024 Al -T351*, in: *Prakt. Metallogr.*, Volume 41, 304–313.
- RABATNOV, J. N. (1969): *Creep Problems in Structural Members*, North-Holland, Amsterdam 1969.
- RADHAKRI, V. (1980): *An analysis of Low Cycle Fatigue based on hysteresis energy*, in: *fatigue & Fracture of Engineering Materials & Structures*, Volume 3(1), 75–84.
- RICE, J. & TRACEY, D. (1969): *On the ductile enlargement of voids in triaxial stress fields*, in: *J. Mech. Phys. Solids*, Volume 17, 201–217.
- ROUSSELIER, G. (1987): *Ductile fracture models and their potential in local approach of fracture*, in: *Nucl. Eng. Des.*, Volume 105, 97–111.

- SCHMIDT, H. (June 6-10 (2005)): *Damage Tolerance technology for current and future aircraft structure*, in: *Proceedings ICAF 2005, 23rd Symposium of the International Committee on Aeronautical Fatigue, Hamburg, Germany, June 6-10 (2005)*.
- SCHÜTZ, W. (2003): *A history of fatigue*, in: *Int. J. Fatigue*, Volume 25, 679–702.
- STEGLICH, D., BROCKS, W. & PARDOEN, T. (2008): *Anisotropic ductile fracture of Al2024 alloys*, in: *Eng. Fract. Mech.*, Volume 75, 3692–3706.
- TANAKA, K. (1982): *A theory of fatigue crack initiation at inclusions*, in: *Metallurgical Transactions a-Physical Metallurgy and Materials Science*, Volume 13(1), 117–123.
- TVERGAARD, V. & NEEDLEMAN, A. (1984): *Analysis of the cup-cone fracture in a round tensile bar*, in: *Acta Metall.*, Volume 32, 1, 157–169.
- WÖHLER, A. (1858): *Über die Festigkeits-Versuche mit Eisen und Stahl*, in: *Zeitschrift für Bauwesen*, Volume 8,10,13,16,20.

## List of Figures

3.1	The severely damaged fuselage of the Aloha Airlines Boeing 737	6
3.2	Cyclic tension-compression response for high cycle fatigue of A 316 stainless steel (Dufailly & Lemaitre, 1995)	7
3.3	Cyclic tension-compression response for low cycle fatigue of A 316 stainless steel (Dufailly & Lemaitre, 1995)	8
3.4	Characterisation of cyclic loads	9
3.5	Different cyclic loading sequences, according to Haibach & Lehrke (1976)	10
3.6	Typical Wöhler curve with stages: L - Low Cycle, H - High Cycle and I - Unlimited fatigue life, cf. Haibach & Lehrke (1976)	11
4.1	The three main directions of the material as defined with respect to the rolling process	17
4.2	Locations of the specimens extracted from the 4 mm thin sheet and the 100 mm thick plate	18
4.3	Tensile tests of the standard round bar specimen extracted from the 100 mm plate	19
4.4	Specimen geometries for smooth and notched round specimen (100 mm plate)	21
4.5	Experimental results of the round notched bars (RNB) taken from the 100 mm plate	22
4.6	Force vs elongation experimental results of the notched round bars taken from the 100 mm plate, (S, L and T-direction) compared to that of round specimen, see Figure 4.4(a)	22
4.7	Attachment of the strain gauge to the specimen extracted from the 100 mm plate	23
4.8	Experimental lifetime of specimens with $r=2$ mm and $r=10$ mm round notched bars (RNB) taken from the 100 mm plate, see Figure 4.4(a)	25
4.9	Mechanical response of DLC-specimens extracted from a plate having a thickness of 100 mm (S-direction)	26
4.10	Flat specimen geometry extracted from 4 mm sheet used in the fatigue tests	26

4.11	The response of the material at uni-axial tensile loading (4 mm sheet) . . . . .	28
4.12	Anti-buckling support during LCF experiment . . . . .	29
4.13	The tensile mechanical behaviour at the first half cycle from cyclic experiments. . . . .	29
4.14	Peak stresses within the LCF experiments conducted on flat specimen (4 mm sheet) . . . . .	30
4.15	Hysteresis produced by the flat specimen (4 mm sheet) subjected to loading with a strain range of 0.035 (with anti-buckling guides) . . . . .	31
4.16	Coffin-Manson diagrams for the specimens (4 mm sheet) according to Figure 4.10 (model parameters according to Table (4.6)) . . . . .	31
4.17	Etched microstructure of the 100 mm plate . . . . .	33
4.18	4 mm sheet of Al2024-T351 . . . . .	34
4.19	Particles of PL III (100 mm plate), see Table (4.9) . . . . .	36
4.20	Network of Particle level I in two different planes of a 100 mm plate . . . . .	38
4.21	Particle Level I and PFB (Quan et al., 2004) detected at a 100 mm plate . . . . .	39
4.22	Density of Particle level I vs distance from the surface of the 100 mm plate . . . . .	39
4.23	Possible fracture mechanisms at room temperature under static loading . . . . .	40
4.24	SEM image of longitudinal micro-sections close to the fracture surface of the monotonically loaded RNB (Figure 4.4(a)) specimen (100 mm plate, S-direction) . . . . .	43
4.25	Fractured surface profiles of Al2024-T351 RNB specimen in L and -direction of the 100 mm plate (SEM data, visualised using 3D image re-construction software, Mex (Alicona, Inc.) (Mex-Alicona <sup>®</sup> , 2010)) . . . . .	44
4.26	SEM obtained image of fracture surfaces in RNB specimens (100 mm plate, see Figure 4.4(a)) close to the notch root . . . . .	45
4.27	A 60° axial view of the fracture surface; failure after 135 cycles in L-direction (4 mm sheet), $\Delta\varepsilon=0.0275$ . The lower small circle indicates the crack initiation site . . . . .	45
4.28	3D rendered micro-structure of the fracture surface; the left lower circle indicates the crack initiation site; failure after 135 cycles in L-direction (4 mm sheet), $\Delta\varepsilon=0.0275$ . . . . .	47
4.29	Damage mechanisms in a 4 mm sheet (failure after 135 cycles in L-direction, $\Delta\varepsilon=0.0275$ ) . . . . .	47

4.30	(above) SEM fractograph of the failure surface after 135 cycles in L-direction (4 mm sheet), $\Delta\varepsilon=0.0275$ . The line defines the analysed path; (below) profile analysis associated with the above path showing two big cavities at the surface . . . . .	48
4.31	SR $\mu$ CT analysis on a 100 mm thick Al2024 plate (virgin state; see, Steglich et al. (2008)) . . . . .	51
4.32	The geometry of the modified specimens (100 mm plate) used for SR $\mu$ CT investigations . . . . .	51
4.33	Uniaxial tests done on specimens having a 10 mm notch (gauge length $l_0=10$ mm) extracted from a 100 mm plate . . . . .	52
4.34	Cyclic mechanical response of small specimen (see before) of Al2024-T351 extracted from the S-direction of the 100 mm plate (see Figure 4.32) . . . . .	53
4.35	Schematic illustration of the synchrotron micro-tomography measurement system . . . . .	54
4.36	Loading device and visualisation of the SR $\mu$ CT experiments (beamline HARWI-II) . . . . .	55
4.37	Re-construction of the hourglass specimen, see Figure 4.36(a) (100 mm plate, S-direction) with SR $\mu$ CT . . . . .	56
4.38	Re-constructed SR $\mu$ CT data; 3D images of the notched specimen (S-direction, 100 mm plate) (notch radius=4 mm), cf. (Khan et al., 2010) . . . . .	57
4.39	Attenuation coefficient measured by using SR $\mu$ CT. . . . .	58
4.40	Results of the SR $\mu$ CT; Cyclically loaded RNB specimen with a notch radius of 10 mm (S-direction, 100 mm plate, see Figure 4.32) . . . . .	58
4.41	Results of the SR $\mu$ CT for cyclic loading conditions: Top views of damage in the specimen (S-direction, 100 mm plate) with a 10 mm notch at different loading stages, see Figure 4.34(b) . . . . .	59
4.42	Results of the SR $\mu$ CT: Cyclically loaded hourglass specimens (S-direction, 100 mm plate) . . . . .	60
4.43	Results of an optical microscopy study: RNB with 10 mm notch (S-direction, 100 mm plate) at stage E, longitudinally cut and polished afterwards . . . . .	60
4.44	Results of the SR $\mu$ CT: Fractured surfaces (S-direction, 100 mm plate) . . . . .	61
5.1	Scalar-valued damage variable - as defined by Kachanov (1958)	64
5.2	One-dimensional representation of strain equivalence concept (Chaboche, 1988) . . . . .	65
5.3	DLC-specimen (S-direction, 100 mm plate) $\Delta\varepsilon = 0.02$ ; $\Delta\varepsilon^p = 0.0063$ ; $N_R^{\text{exp}} = 138$ . . . . .	71

5.4	Experimental vs. simulated (For Desmorat-Lemaitre, see Section 5.2 and for Coffin-Manson curve . . . . .	73
5.5	Mechanical responses of the notched specimen (2mm notch, $\Delta l = 0.02$ mm) extracted from S-direction of the 100 mm plate. Point 1 indicates the formation of a crack at the surface of the specimen. . . . .	74
5.6	Experimental ( $\circ$ - tension, $\square$ - compression) vs. simulated (- CDM) force peaks. The simulation in (b) was stopped due to saturation of the plastic energy function (2000 cycles) . . . . .	76
5.7	Distribution of damage in loading direction at the rupture time point ( $N = N_R$ ) . . . . .	77
6.1	Elasto-plastic hysteresis (DLC-specimen, 100 mm plate); experimental data and simulation for a strain range of $\Delta \epsilon = 0.025$ . .	89
6.2	Comparison of simulation and related experimental data for the initial 2 cycles (flat specimen, 4 mm sheet) . . . . .	90
6.3	Sketch of the DLC-specimen extracted from S-direction of the 100 mm plate (see Figure 4.4(a)), loading conditions and finite element discretisation . . . . .	93
6.4	Damage activation criterion for two different strain amplitudes (DLC-specimen) at point A . . . . .	93
6.5	Evolution of the damage variable $\mathcal{D} = \mathcal{D}^p + \mathcal{D}^b$ for two different strain amplitudes (DLC-specimen) at point A . . . . .	94
6.6	Ductile and brittle damage variables for two different strain amplitudes (DLC-specimen) at point A . . . . .	94
6.7	Maximum CAUCHY stresses for two different strain amplitudes (DLC-specimen) at point A . . . . .	95
6.8	Predictions of the ductile and the coupled model for DLC-specimens (S-direction, 100 mm plate), see Table (5.3) . . . . .	96
6.9	Sketch of the flat specimen (4 mm sheet) and the loading conditions used in the finite element simulations . . . . .	97
7.1	Fuselage stiffened panel: configuration and loading condition (FAA, 1993) . . . . .	100
7.2	Fuselage stiffened panel with a longitudinal skin crack over a broken frame (FAA, 1993) . . . . .	100
7.3	General crack growth behaviour of a skin crack propagating through a stiffened panel over a broken stringer . . . . .	101
7.4	Beneficial effect of the bonded stiffened panels in comparison with riveted and monolithic solutions Meneghin (2010) . . . . .	102
7.5	The dimensions of the skin-stringer assembly . . . . .	102
7.6	The complete skin-stringer assembly with elliptical pre-crack .	103
7.7	Evolution of the stored plastic energy $w_s$ driving damage initiation	105

## List of Tables

3.1	Classification of fatigue (Dufailly & Lemaitre, 1995) . . . . .	6
3.2	Equations for the description of S-N curve according to Haibach & Lehrke (1976) . . . . .	11
4.1	Chemical composition limits of Al2024 alloy. Maximum value is given, if range is not shown . . . . .	16
4.2	Results of the static test for the L, T and S-directions taken from 100 mm plate, with $l_0=50$ mm . . . . .	19
4.3	Out-of-roundness of the section of the specimens (100 mm plate) at the end of the test. $d_{\max}$ is the longest diameter of the section, $d_{\min}$ the shortest and $d_0$ the initial diameter . . . . .	20
4.4	Matrix of LCF experiments conducted on specimens extracted from 100 mm plate . . . . .	24
4.5	Mechanical properties of 4 mm sheet of Al2024-T351 (uniaxial tensile loading), see Figure 4.2 . . . . .	27
4.6	Coffin-Manson parameters for Al2024-T351 flat specimen (4 mm sheet) . . . . .	31
4.7	Experimental results for smooth flat specimens (4 mm sheet); for L and T-direction . . . . .	32
4.8	Main diameter ratios of the grains in the 100 mm plate, $D_X$ is the diameter along L, T, S-direction . . . . .	33
4.9	Main dimensions of the three levels of particles (100 mm plate) and their area density detected at the scanning electronic microscope (Quan et al., 2004) . . . . .	35
4.10	Parameters of SR $\mu$ CT at beamline HARWI-II . . . . .	54
4.11	Components used for SR $\mu$ CT . . . . .	55
4.12	Volumetric analysis of Al2024-T351 (S-direction, 100 mm plate) . . . . .	57
5.1	Parameters defining the underlying elasto-plastic model according to Section 5.2.1 (DLC-specimen taken from S-direction of a 100 mm plate) . . . . .	71
5.2	Parameters of the model governing the evolution and the threshold values of the stored plastic energy (Section 5.2.2) and damage evolution (Section 5.2.3) . . . . .	72

5.3	Experimental results for smooth round bars (abbreviation DLC) taken from S-direction of the 100 mm plate . . . . .	74
5.4	Comparison of the simulation results to the experimental data for the notched specimens (S-direction, 100 mm plate) . . . . .	76
6.1	Optimised material parameters characterising the elasto-plastic response (DLC-specimen, $\Delta\varepsilon = 0.025$ ) . . . . .	89
6.2	Optimised material parameters for elasto-plasticity for Al2024 4 mm sheet, for both L and T-directions . . . . .	90
6.3	Parameters for isotropic hardening, Al2024-T351 . . . . .	91
6.4	Optimised parameters for damage initiation parameters of Al2024-T351 . . . . .	91
6.5	Damage parameters of Al2024-T351 for the combined ductile-brittle damage model law . . . . .	92
6.6	Numerically simulated number of cycle $N_D^{\text{sim}}$ , $N_R^{\text{sim}}$ (4.1) and error with respect to $N_R^{\text{exp}}$ ("DLC-X" abbreviation according to Table 5.3). . . . .	95
6.7	The lifetime prediction (quasi-brittle ductile model) compared to experiments in the LCF regime (for both L and T-directions, 4 mm sheet). $N_E^{\text{exp}}$ is the number of loading cycles during the softening regime . . . . .	98



## Curriculum Vitae

Name	Shehzad Saleem Khan
Date of birth	13.08.1982
Nationality	Pakistani
06/1995 – 06/1998	High school (10th grade) - Kohat Secondary school certificate (SSC)
07/1998 – 09/2000	Cadet College Kohat - Pakistan Faculty of science (FSc) Pre-Engineering
01/2001 – 08/2004	National University of Sciences and Technology Faculty of Engineering Sciences BE (Mechanical)
09/2005 – 06/2007	Universität Stuttgart - Germany Institut für Mechanik (Bauwesen) Certificate: MSc in Computational Mechanics
06/2007 – 01/2011	HZG Helmholtz Zentrum Geesthacht GmbH Geesthacht - Germany Institute of Materials research Doctoral Studies